The Dissertation Committee for Junghyun Kim certifies that this is the approved version of the following dissertation:

DEVELOPMENT OF ALTERNATIVE CATHODES FOR INTERMEDIATE TEMPERATURE SOLID OXIDE FUEL CELLS

Committee:

Arumugam Manthiram, Supervisor

John B. Goodenough

Desiderio Kovar

Paulo Ferreira

Keith Stevenson

DEVELOPMENT OF ALTERNATIVE CATHODES FOR INTERMEDIATE TEMPERATURE SOLID OXIDE FUEL CELLS

by

Junghyun Kim, B.S.; M.S.

Dissertation

Presented to the Faculty of the Graduate School of
the University of Texas at Austin
in Partial Fulfillment
of the Requirements
for the Degree of
Doctor of Philosophy

The University of Texas at Austin
August 2009

Acknowledgements

I would like to express my deepest appreciation to my advisor Professor Arumugam Manthiram for his guidance, trust, and heartwarming encouragement. Without his guidance and persistent help, this dissertation would not have been possible. I would also like to thank my committee members, Professors John Goodenough, Desiderio Kovar, Paulo Ferreira, and Keith Stevenson for their valuable suggestions on my dissertation.

I wish to thank several of my colleagues who helped me during the course of this dissertation work: Dr. Kee-Tae Lee for training me in many of the experimental techniques in SOFC, Dr. Fernando Prado for helping me with the oxygen permeation experiments, Dr. Claudia Torres-Garibay for showing me the single cell fabrication technique, and Mr. Young Nam Kim for his sincere assistance with experiments.

In addition to the technical assistance above, I have received equally important assistance from family and friends. I thank my wife, Jeeyoung Lee, for her love and steady support that cannot be described within a few words. I thank my parents, parent-in-laws, brother, and brother-in-law for believing and supporting me. I also thank Korean friends in Austin who share lots of good memories with me. I must thank Mr. Arindam Sakar, Mr. Alayavalli Kaushik, and Mr. Eungje Lee for our intensive discussion together on coursework, experiments, and qualifying exam. Last but foremost gratitude goes to Jesus Christ who will guide the rest of my life.

DEVELOPMENT OF ALTERNATIVE CATHODES FOR INTERMEDIATE TEMPERATURE SOLID OXIDE FUEL CELLS

Publication No. _______________

Junghyun Kim, Ph.D.

The University of Texas at Austin, 2009

Supervisor: Arumugam Manthiram

Solid oxide fuel cells (SOFCs) offer the advantage of using less expensive oxide catalysts and directly using hydrocarbon fuels without requiring external fuel reforming due to the higher operating temperatures of > 500°C compared to the proton exchange membrane fuel cells. However, the conventional operating temperature of ~ 1000 ^{o}C leads to undesired side reactions and thermal expansion mismatch among the cell components. These difficulties have generated considerable interest in intermediate temperature (500 - 800 ^{o}C) SOFC, but the lower operating temperature leads to poor oxygen reduction reaction kinetics with the conventional cathode material, $La_{1-x}Sr_xMnO_3$. In this regard, the cobalt-containing perovskite cathodes such as $La_{1-x}Sr_xCoO_{3-\delta}$ are appealing, but it suffers huge thermal expansion mismatch with the conventional electrolytes. To address this issue, this dissertation focuses on two series of new cathode materials.

First, the influence of the Ln^{3+} ions on the high temperature properties and performance in SOFC of the layered $LnBaCo_2O_{5+\delta}$ (Ln = La, Nd, Sm, Gd, and Y) oxides is investigated systematically. The oxygen content ($5+\delta$), thermal expansion coefficient (TEC), electrical conductivity, catalytic activity for the oxygen reduction reaction in SOFC, and oxygen permeability decrease with decreasing size of the Ln^{3+} ions from Ln = La to Y. These results suggest that lanthanide ions with an intermediate size may offer a tradeoff between catalytic activity and TEC. With an aim to tune the properties further, cationic substitutions are then pursued. For example, substitution of Sr for Ba is found to improve the chemical stability of $GdBaCo_2O_{5+\delta}$ with improved catalytic activity. Similarly, the substitution of Ni for Co is found to lower the TEC to 16.9×10^{-6} K^{-1} while still maintaining high catalytic activity at $x = 0.4$ in $NdBaCo_{2-x}Ni_xO_{5+\delta}$.

Second, non-perovskite $RBa(Co,M)_4O_7$ (R = Y, Ca, and In and M = Zn, Fe, and Al) oxides having a hexagonal structure and corner-shared $(Co,M)O_4$ tetrahedra are investigated. Among the various compositions investigated, $YBaCo_{4-x}Zn_xO_7$ ($1 \leq x \leq 2$) shows good long-term stability at high temperatures with an ideal matching of the TEC with those of standard electrolytes. The low TEC is attributed to the absence of spin state transitions with tetrahedral-site $Co^{2+/3+}$ ions and relatively small amount of oxygen loss at higher temperatures. The $YBaCo_3ZnO_7$ + GDC composite cathodes exhibit low polarization resistance and performance in SOFC comparable to that of well-studied cobalt-based perovskite cathodes.

TABLE OF CONTENTS

CHAPTER 1

CHAPTER 2

CHAPTER 6

Layered $NdBaCo_{2-x}Ni_xO_{5+\delta}$ Perovskite Oxides as Cathodes for Intermediate Temperature SOFC *98*

PART II

NON-PEROVSKITE OXIDE CATHODE MATERIALS FOR INTERMEDIATE TEMPERATURE SOFC 120

CHAPTER 7

Low Thermal Expansion $RBa(Co,M)_4O_7$ Cathodes Based on Tetrahedral-site Cobalt Ions for IT-SOFC *121*

LIST OF TABLES

LIST OF FIGURES

CHAPTER 1

Introduction

1.1 FUEL CELLS

Fuel cells are electrochemical devices which convert chemical energy directly into electrical energy. The conventional power generators involving the conversion of fuel to heat, to mechanical energy, and then to electrical energy are limited by the carnot-cycle with a low efficiency of ~ 30 %. Interestingly, fuel cells eliminate the intermediate fuel to heat to mechanical energy conversion losses, offering high efficiencies (> 50 %). Since the invention of the concept of fuel cells first by Sir William Robert Grove (1811-1896), the fuel cell technology has grown and evolved into different types of fuel cells. Moreover, recent environmental concerns and energy crisis have stimulated enhanced interest in fuel cell technologies.

1.1.1 Basic Principles

The first fuel cell concept was invented by Sir William Robert Grove in 1839. He first electrolyzed water into oxygen and hydrogen by applying a current (Figure 1.1a).[1,2] After replacing the current source to an ammeter, he discovered that a small amount of current was produced by a recombination of hydrogen and oxygen (Figure

1.1b). Simply, the H_2 gas is first oxidized with the assistance of Pt to produce protons and electrons as below:

$$2H_2 \rightarrow 4H^+ + 4e^- \tag{1.1}$$

The protons migrating through the acidic electrolyte then combines with the O_2 gas and the electrons flowing through the external circuit to form water with the assistance of Pt as below:

$$4H^+ + O_2 + 4e^- \rightarrow 2H_2O \tag{1.2}$$

The overall chemical reaction is as follows:

$$2H_2 + O_2 \rightarrow 2H_2O \tag{1.3}$$

Here, the acid electrolyte exclusively transports protons and blocks the electron passage; the electrons flow only through the external circuit. However, the resulting current generated by the fuel cell in Figure 1.1b was not high due to the large electrolyte resistance between the Pt electrodes and low area of active sites where gas-electrode-electrolyte meets together. In modern fuel cells, electrolyte properties and the area of gas-electrode-electrolyte boundaries are well-controlled to optimize the chemical reaction.

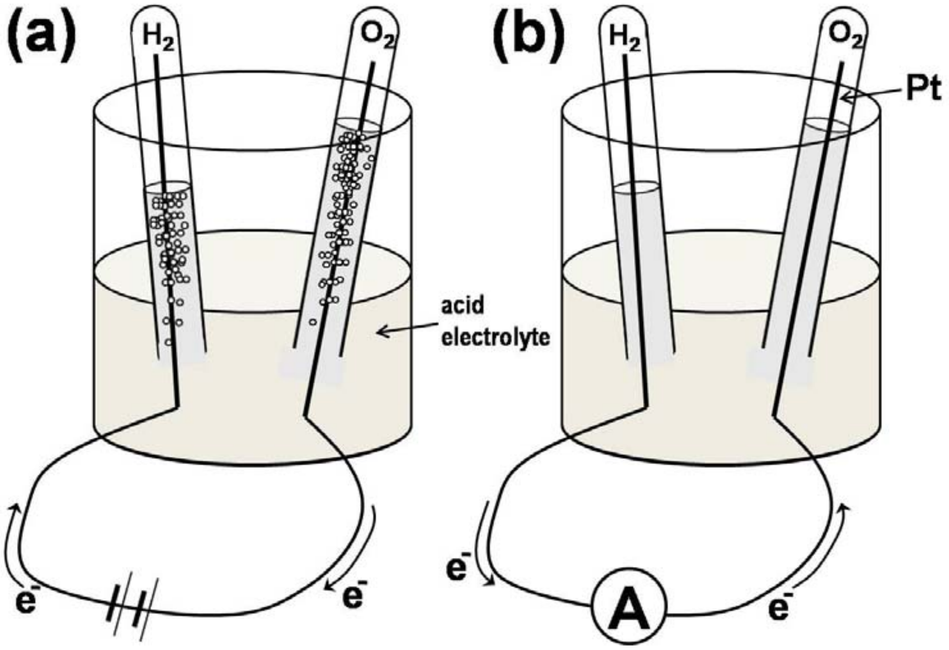

Figure 1.1 (a) Water electrolysis and (b) spontaneous fuel cell reaction producing current.

1.1.2 Types of Fuel Cells

Since the first successful fuel cell experiments by Sir William Robert Grove in a labolatory scale, many different types of fuel cells have been proposed. Modern fuel cells can be classified according to the electrolyte or catalyst used or the operating temperature as seen in Table 1.1.[3,4,5]

Table 1.1 Characteristics of various fuel cells.[3]

	Phosphoric Acid Fuel Cell (PAFC)	**Alkaline Fuel Cell (AFC)**	**Polymer Electrolyte Fuel Cell (PEFC)**	**Direct Methanol Fuel Cell (DMFC)**	**Molten Carbonate Fuel Cell (MCFC)**	**Solid Oxide Fuel Cell (SOFC)**
Operation Temperature (^{o}C)	190-200	80-90	25-80	25-90	650	600-1000
Electrolyte	H_3PO_4	KOH	Proton conducting polymer	Proton conducting polymer	Li_2CO_3-K_2CO_3	YSZ
Mobile ion	H^+	OH^-	H^+	H^+	CO_3^{2-}	O^{2-}
Cathode	Pt	Pt-Au	Pt	Pt	Li-NiO	(La,Sr)MnO_3
Cathode Reaction	$H_2 \rightarrow 2H^+ + 2e^-$	$O_2 + 2H_2O + 4e^- \rightarrow 4OH^-$	$O_2 + 4H^+ + 4e^- \rightarrow 2H_2O$	$3/2O_2+6H^++6e^- \rightarrow 3H_2O$	$O_2 + 2CO_2 + 4e^- \rightarrow 2\ CO_3^{2-}$	$O_2 + 4e^- \rightarrow 2O^{2-}$
Anode	Pt	Pt-Pd	Pt	Pt-Ru	Ni	Ni/YSZ
Anode Reaction	$O_2 + 4H^+ + 4e^- \rightarrow 2H_2O$	$H_2 + 2OH^- \rightarrow 2H_2O + 2e^-$	$H_2 \rightarrow 2H^+ + 2e^-$	$CH_3OH + H_2O \rightarrow CO_2 + 6H^+ + 6e^-$	$H_2 + CO_3^{2-} \rightarrow H_2O + CO_2 + 2e^-$	$H_2 + O^{2-} \rightarrow H_2O + 2e^-$

1.2 SOLID OXIDE FUEL CELL

A solid oxide fuel cell (SOFC) is an all-solid-state energy conversion device in which a solid electrolyte is combined with ceramic or ceramic-metal (cermet) electrodes (cathode and anode).[3] During the SOFC operation, oxygen from air is used as an oxidant in the cathode side and hydrogen or hydrocarbons are used as fuels in the anode side. The solid electrolyte transports O^{2-} ions from the cathode to anode side. To realize adequate oxide-ion conductivity with the solid electrolyte, SOFC requires high operating temperatures of $> 500\ ^{o}C$, which facilitates the use of inexpensive ceramic or cermet catalysts instead of the expensive and scarcely available platinum catalysts.[6] In addition, the higher temperatures allow the direct use of hydrocarbon fuels without requiring an external reformer to produce hydrogen fuel.[7]

1.2.1 Principles of SOFC Operation

The schematic diagram illustrating the operation of SOFC is shown in Figure 1.2. At the cathode side, the oxygen reduction reaction occurs by accepting electrons from the external circuit. The generated oxide ions (O^{2-}) pass through the electrolyte to the anode side, where the O^{2-} ions combine with the protons produced by oxidation of hydrogen gas to produce water. The electrons flowing from the anode to the cathode produce electrical work in the "Load". Through this process, chemical energy is directly converted to electrical energy.

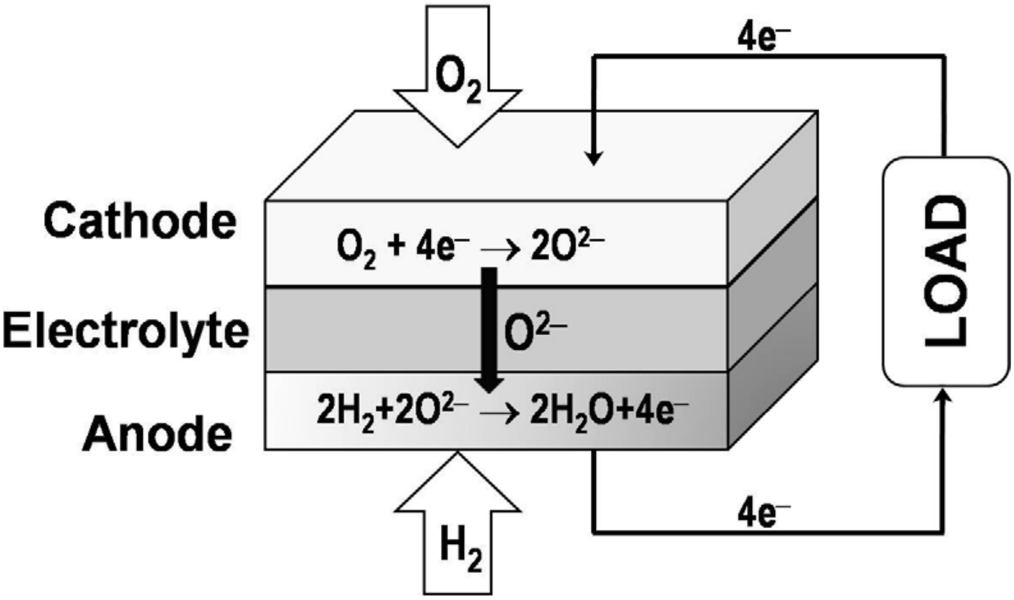

Figure 1.2 Schematic diagram showing the operation of SOFC.

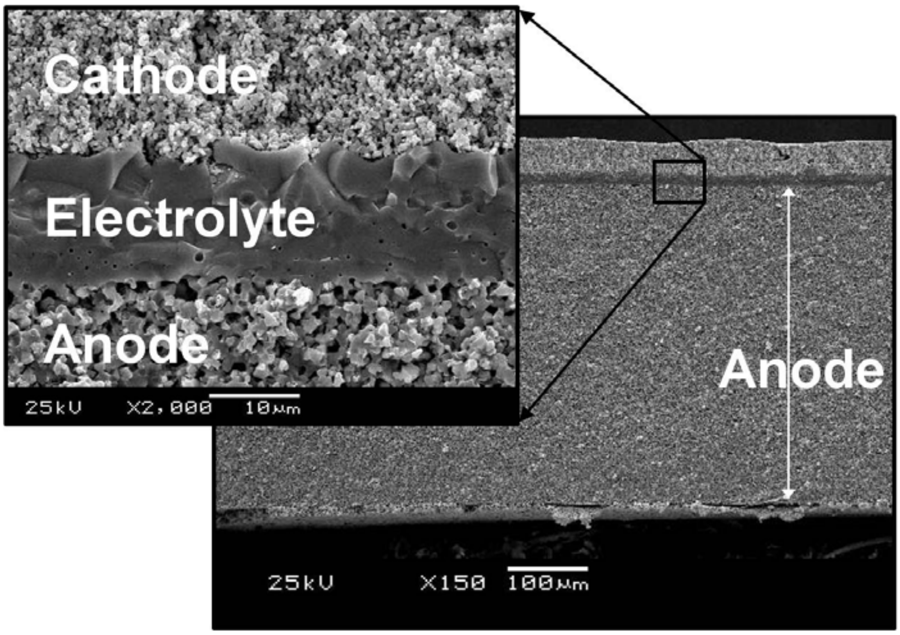

Figure 1.3 Microstructure of anode-supported single cell SOFC.

To increase the active area where the oxygen reduction reaction (cathode) or hydrogen oxidation reaction (anode) occurs, a porous electrode structure is employed. Meanwhile, the dense electrolyte provides a physical barrier to prevent the direct mixing of fuel and air. Figure 1.3 shows the cross-sectional view of a single SOFC. The expanded view shows the dense electrolyte film (~ 15 μm) providing a good separation between the porous cathode and anode.

1.2.2 Thermodynamics of SOFC

Considering the basic SOFC chemical reaction,

$$H_2 + 1/2\ O_2 \rightarrow H_2O\ (g) \tag{1.4}$$

the difference in the Gibbs free energy of formation ΔG_f during the reaction can be given as

$$\Delta G_f = G_{H_2O(g)} - G_{H_2} - 1/2\, G_{O_2} \tag{1.5}$$

where G_{H_2O}, G_{H_2}, and G_{O_2} refer, respectively, to the free energies of water, hydrogen, and oxygen. If all the Gibbs free energy is consumed to electrical work, then

$$\Delta G_f = -nFE \tag{1.6}$$

If the reactants and products are all in their standard conditions, the reversible standard potential E^0 of the electrochemical reaction is defined as

$$E^0 = -\frac{\Delta G_f^0}{nF} \tag{1.7}$$

where n is number of electrons involved in the chemical reaction and F is the Faraday constant. Here, the Gibbs free energy is dependent on the temperature by the relation

$$\Delta G_f = \Delta H_f - T\Delta S_f \tag{1.8}$$

where ΔH_f is the enthalpy change for the reaction, T is the absolute temperature, and ΔS_f is the entropy change for the reaction. The different ΔG_f values at different temperatures are available in the literature.[2] Substitution of the standard condition values into Eq. (1.7) gives

$$E^0 = -\frac{(-237300\ \mathrm{J/mol})}{2(96485\ \mathrm{C/mon})} = 1.23\ \mathrm{V} \tag{1.9}$$

Beyond the standard condition, the theoretical reversible potential E_{th} can be expressed by the Nernst equation[8,9] as

$$E_{th} = E^0 - \frac{RT}{2F}\ln\left(\frac{p_{\mathrm{H_2O}}}{p_{\mathrm{H_2}} \cdot p_{\mathrm{O_2}}^{\frac{1}{2}}}\right) \tag{1.10}$$

where R is the gas constant, T is the absolute temperature, p is the partial pressure of each gas.

1.2.3 El ectrochemistry of SOFC

A typical current-voltage (I-V) curve obtained in SOFC is displayed in Figure 1.4. The actual cell potential drops as current is drawn during the SOFC operation. The degree of potential dropt is affected by several factors such as temperature, electrode or electrolyte materials, electrolyte thickness, microstructure of the electrodes, gas flow rates, etc. The difference between the theoreticl reversible potential and the actual cell potential is termed as polarization loss or over-potential (η). The overall polarization loss in the fuel cell system is composed of three contributions:[2,3,10]

- Activation polarization, η_{Act}
- Ohmic polarization, η_{Ohm}
- Concentration polarization, η_{Con}

The activation polarization (η_{Act}) is related to the kinetics of the electrode reaction. For the electrode reaction to occur, activation energy needs to be provided to overcome the energy barrier and undergo charge transfer or the surface exchange reactions in the electrode. In other words, the activation polarization can be understood as the overpotential consumed to provide the activation energy for the redox reactions in the electrode.

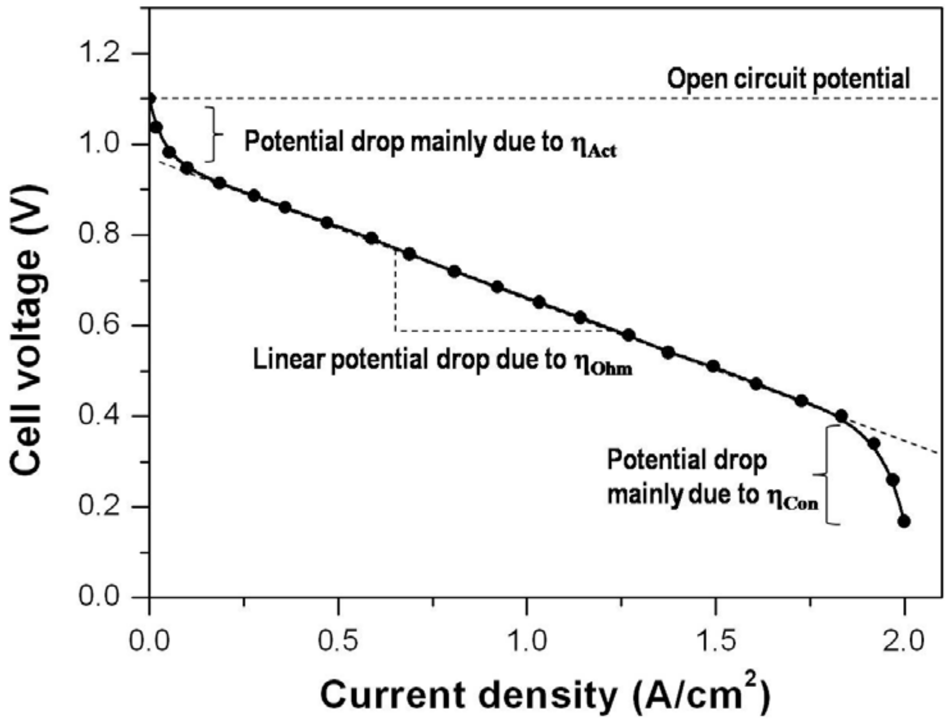

Figure 1.4 Characteristics of a typical current-voltage curve in SOFC.

The ohmic polarization (η_{Ohm}) is related to the electrical resistance of the fuel cell components. It includes ionic resistance in the electrolyte, electronic resistances in the electrodes (cathode and anode), interfacial resistance between the electrodes and electrolyte, and wire resistance in the external circuit.

The concentration polarization (η_{Con}) is related to the mass-transport or diffusion limitation during the SOFC operation. When the reactants could not be supplied fast enough to maintain the rate of the electrode reaction, depletion of reactants causes the contentration polarization. Therefore, the concentration polarization is highly dependent on the type of gas, diffusion length, and pore size. The concentration polarization can be observed especially under high current drain as shown in Figure 1.4.

The overall polarization in the fuel cell system is expressed as sum of these three principal polarizations as

$$\eta_{\text{Total}} = \eta_{\text{Act}} + \eta_{\text{Ohm}} + \eta_{\text{Con}} \tag{1.11}$$

1.2.4 Advantages and Disadvantages of SOFC

The characteristics of SOFC in comparison to some of the other types of fuel cells are all-solid-state system and high operating temperatures (> 500 ^{o}C). The advantages of SOFC can be summarized as follows:[3,11,12]

- Use of inexpensive ceramic or cermet catalyst as cathode or anode
- Direct use of hydrocarbon fuels without requiring external reformer to produce hydrogen fuel
- Higher energy conversion efficiency (> 60 %) achievable in combination with a gas-turbine system
- Elimination of corrosion problems encountered with liquid electrolytes as in phosphoric acid fuel cells (PAFC) and molten carbonate fuel cells (MCFC) due to the use of solid electrolytes

In contrast, the SOFC technology has the following problems to overcome:[3,11,12]

- High electrolyte resistance of the yttria-stabilized zirconia (YSZ) electrolyte at the intermediate temperatures of 500 – 800 °C
- Chemical and mechanical durability problems of alternative electrolytes with higher oxide-ion conductivity at the intermediate temperatures (*e.g.* divalent or trivalent metal ion doped ceria)
- Slow oxygen reduction kinetics with the conventional cathode materials at the intermediate operating temperatures of 500 – 800 °C
- Thermal expansion mismatch especially between the electrolyte and the cathode
- Carbon cracking and poor tolerance to sulfur impurities with the conventional Ni-based anodes on using hydrocarbon fuels directly

1.3 MATERIALS IN SOLID OXIDE FUEL CELLS

After the observation of oxide ion conduction first by Nernst in YSZ in 1899, Baur and Preis demonstrated the first SOFC in 1937 using YSZ as an electrolyte.[11,13] Early SOFC employed noble metals such as Pt as electrode materials. However, metal oxide materials have been developed as electrode or interconnect materials since the 1980s.

1.3.1 Electrolyte

The requirements of electrolyte materials for SOFC application can be summarized as follows:

- High oxide-ion conductivity
- Low electronic conductivity with an ionic transport number > 0.9
- Good mechanical strength with fracture strength > 400 MPa at room temperature
- Phase stability in wide temperature ranges

YSZ is being used as a traditional electrolyte material in SOFC. The undoped ZrO_2 has a monoclinic crystal structure at room temperature and undergoes phase transitions to tetragonal ($T > 1170\ ^{o}C$) to cubic fluorite ($T > 2370\ ^{o}C$) structures with increasing temperature.[3,14] The Y^{3+} substitution for Zr^{4+}, however, stabilizes the cubic fluorite structure at room temperature and eliminates the phase transition problem. More importantly, the Y^{3+} substitution induces large amount of oxygen vacancies in the crystal lattice and provides channels for oxygen ion conduction.

YSZ has the advantages of acceptable ionic conductivity at high temperature (0.15 S/cm at 1000 ^{o}C with $E_a = 0.91$ eV for 8 mol% Y_2O_3 stabilized ZrO_2), good chemical stability with an ionic transport number > 0.99 in H_2 atmosphere, and good mechanical strength.[15,16] However, YSZ suffers from its low ionic conductivity at intermediate temperatures of 500 – 800 ^{o}C. To overcome this problem thin YSZ films (thickness: ~ 10 μm) with anode-supported cell geometry has been a developed for intermediate temperature SOFC.

Ceria-based electrolytes have been investigated as a possible alternative to YSZ due to its high oxide ion conductivity at intermediate temperatures of 500-800 °C (see Figure 1.5). The ionic conductivity could be maximized by a substitution of Gd (GDC) or Sm (SDC) for Ce in CeO_2. However, the main problem of doped ceria is the reduction of Ce^{4+} to Ce^{3+} ions at low oxygen partial pressures. This creates electronic conduction within ceria (n-type small-polaron conduction) and leads to a leakage of current through the electrolyte.[17] To overcome this problem, thin layers of YSZ has been employed in between the anode and the ceria electrolyte.[18,19] Although the YSZ functional layer prevents ceria from direct contact with the fuel, formation of impurity phases with low ionic conductivity at the YSZ-GDC interface has been an issue.[20,21]

$LaGaO_3$-based electrolyte materials have the perovskite structure. High oxide ionic conductivity can be obtained by appropriate amount of cation substitutions for both La and Ga. The maximum value of oxide ion conductivity has been reported for $x = 0.1 – 0.2$ and $y = 0.15 – 0.2$ in $La_{1-x}Sr_xGa_{1-y}Mg_yO_{3-\delta}$ (LSGM).[22-24] The optimized LSGM shows higher oxide ion conductivity compared to that obtained with the YSZ electrolyte while maintaining the low electronic conductivity at low oxygen partial pressures. Therefore, LSGM is considered as a promising electrolyte for intermediate temperature SOFC. Nevertheless, the high cost of Ga becomes an obstacle for the commercialization prospects of LSGM. In addition, LSGM reacts with Ni anode and produces undesired $LaNiO_3$ or La_2NiO_4 phases at the interfaces, which deteriorate the ionic conductivity of LSGM. Further optimization is necessary to employ LSGM as electrolyte in practical SOFCs.

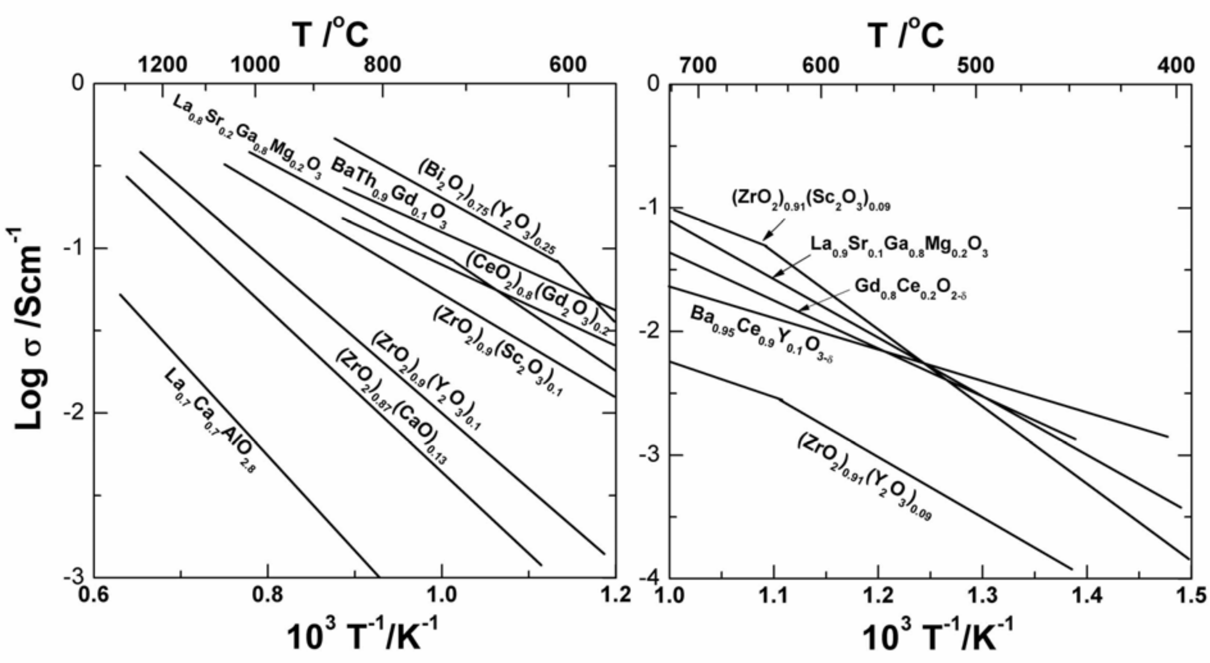

Fiugre 1.5 Temperature dependence of electrical conductivity of various electrolytes.[10]

1.3.2 Cathode

The requirements of cathode materials for SOFC applications can be summarized as follows:[3,11,12]

- Thermal expansion coefficient matching with those of other cell components
- High catalytic activity for the oxygen reduction reaction
- Good chemical stability against electrolyte and interconnect at high temperatures
- Acceptable electrical conductivity (> 100 S/cm)
- Acceptable oxide ion conductivity (> 0.1 S/cm)

The Perovskite $La_{1-x}Sr_xMnO_3$ (LSM) has been investigated as a traditional cathode material for SOFC. The advantage of LSM compared to other cathode materials is the low thermal expansion coefficient of $11 \times 10^{-6} – 13 \times 10^{-6}$ $^oC^{-1}$ in a temperature range of 35-1000 ^oC.[25,26] These low TEC values show good compatibility with YSZ (TEC: 10.5×10^{-6} $^oC^{-1}$).[27] Although LSM shows acceptable electronic conductivity, it shows poor oxide ion conductivity and inadequate catalytic activity at intermediate temperatures because of the stability of Mn^{4+} ions and the difficulty of creating oxygen vacancies in the lattice.[28,29] Due to the sluggish oxygen diffusion rate,[30] the oxygen reduction reaction in LSM mainly occurs at the triple (cathode-electrolyte-gas) phase boundary (TPB). To increase the TPB area, LSM + YSZ composite cathode has been adopted, which provides improved cathode performances compared to the single LSM cathode.[31,32] However, LSM and YSZ reacts with each other and forms a $La_2Zr_2O_7$ impurity phase at the interface.[33] This electronic and oxide ionic insulator phase in between LSM and YSZ decreases the TPB area and finally deteriorates the cathode performance. The side reaction between LSM and YSZ can, however, be suppressed by adopting A-site deficient LSM.[34]

Reducing the operation temperature (< 800 °C) for intermediate temperature SOFC requires cathode materials with a high catalytic activity. In this regard, alternative cathode materials with a mixed oxide ion and electron conducting (MIEC) properties are preferred because the TPB is extended to the surface of the cathode particles. $La_{1-x}Sr_xCoO_{3-\delta}$ (LSC) perovskite cathode has been appealing in this regard due to its good MIEC properties. The LSC cathode shows high oxygen diffusivity due to the large amount of oxygen vacancies.[35,36] Therefore, LSC is more favorable as a cathode material for intermediate temperature SOFC compared to LSM. However, LSC readily reacts with YSZ to form a resistive phase such as $La_2Zr_2O_7$ or $SrZrO_3$ at high temperatures.[37,38] As LSC shows better chemical stability with GDC at high temperatures, a GDC buffer layer has been adopted in between LSC and YSZ electrolyte. However, interfacial reactions between GDC and YSZ has also been reported.[20,21] In addition, the thermal expansion coefficient of LSC (22 to 24 × 10^{-6} $^{o}C^{-1}$) is significantly higher than those of YSZ and GDC.[39,40] The large thermal expansion mismatch between the cathode and the electrolyte can lead to delamination of or cracks in the cathode layer during the thermal cycling of SOFC.[3]

The abnormally high TECs of the cobalt-based perovskite have been attributed to the low-spin to high-spin transition of octahedral-site Co^{3+} ions[41] and the accompanying increase in ionic radius. Attempts such as partial substitution of other elements like Mn, Fe, and Ni for Co have been pursued to lower the TEC, and the Fe-rich $La_{1-x}Sr_xFe_{1-y}Co_yO_{3-z}$ (LSFC) shows moderate TEC with acceptable cathode performance on employing it as a LSCF + electrolyte composite cathode.[42-44] The decreasing Co content in LSFC offers a trade-off between catalytic activity and TEC. Nevertheless, there is immense interest to develop new cathode materials with high catalytic activity and low TEC that is compatible with the electrolyte for intermediate temperature SOFC.

Another class of materials that have drawn some attention is the perovskite-related intergrowth oxides belonging to the Ruddlesden-Popper (R-P) series[45] having the general formula of $(AO)(ABO_3)_n$ with n = 1, 2, 3. These intergrowth oxides have rock-salt AO layers alternating with a single (n = 1), double (n = 2), or triple (n = 3) perovskite $(ABO_3)_n$ layers along the *c* axis.[46,47] For example, Figure 1.5 shows the crystal structure of $(Sr,Ln)_3(Fe,Co)_2O_7$ (n = 2) having (Sr,Ln)O rock salt layers alternating with two $(Sr,Ln)(Fe,Co)O_3$ perovskite layers along the *c* axis. Various compositions in this R–P series have been reported with A = Sr and La, and B = Mn, Fe, Co, Ni, Cu, and Ga.[46-59] The total electrical conductivity and the oxygen permeation flux of the $(Sr,La)_{n+1}(Fe,Co)_nO_{3n+1}$ phases increase with n and reach a maximum value for the $SrCo_{0.8}Fe_{0.2}O_{3-\delta}$ perovskite, which can be considered as the $n = \infty$ member.[47,50,51] Some $Sr_{n+1}(Fe,Co)_nO_{3n+1}$ phases suffer from structural and chemical instability at room temperature due to a slow reaction with H_2O and CO_2 in air.[50] Although La substitution for Sr in the A-sites suppresses the phase degradation in air, their chemical stability need to be assessed further more carefully.

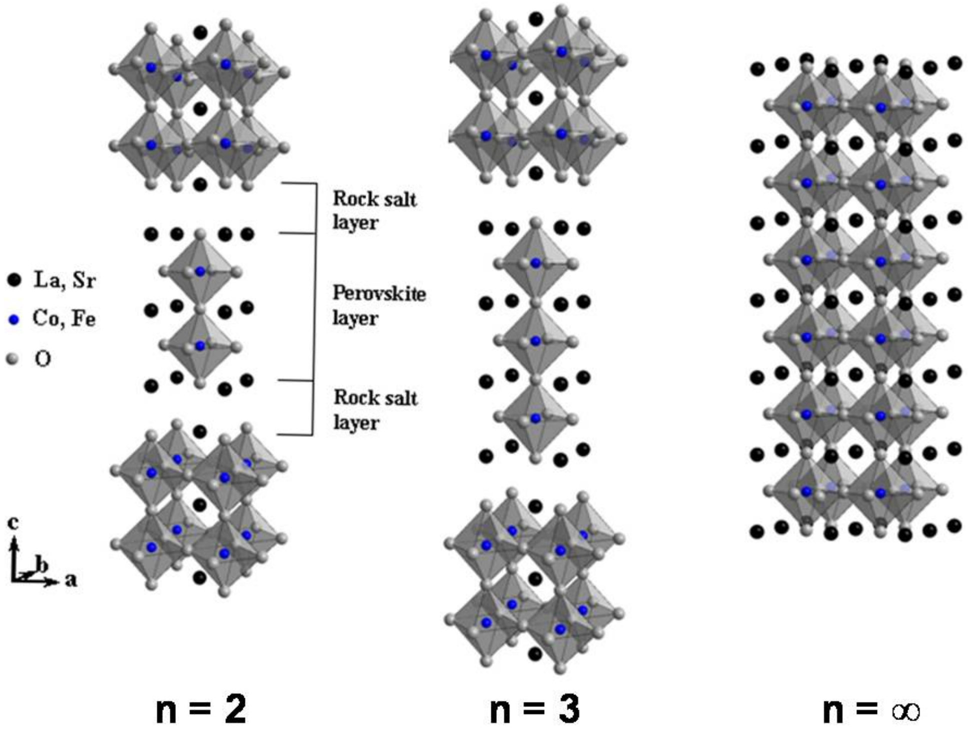

Figure 1.6 Crystal structures of the Ruddlesden-Popper (R-P) series having the general formula of $(AO)(ABO_3)_n$ with $n = 2, 3, \infty$. The perovskite structure is considered to be the $n = \infty$ member.

1.3.3 Anode

The requirements of anode materials for SOFC application can be summarized as follows:[3,11,12]

- Stability in low oxygen partial pressures

- High catalytic activity for hydrogen oxidation and hydrocarbon fuel reactions
- Good chemical stability against the electrolyte and interconnect at high temperatures
- Tolerance to carbon cracking or sulfur impurities when using hydrocarbon fuels directly

The most common anode material in SOFC is the Ni-YSZ cermet, which provides both good oxide ionic conductivity (from YSZ) and electronic conductivity (from Ni).[60] Although the Ni-YSZ cermet anode shows stable performance with H_2 fuel, it experiences critical problems with hydrocarbon fuels. As Ni also shows good catalytic activity for carbon cracking, carbon is easily deposited on the surface of Ni, resulting in performance degradation.[61,62] In addition, direct use of hydrocarbon fuels leads to a strong adsorption of the H_2S impurity from the fuel on the Ni particles, which leads to huge activation polarization and severe performance loss.[63]

Anode materials consisting of Cu, ceria, and YSZ have been found to show high activity with hydrocarbon fuels.[64-68] It has been reported that CeO_2 promotes hydrocarbon oxidation and Cu is not active for carbon cracking. However, Cu shows lower catalytic activity than Ni, and its low melting temperature make it readily react with other cell components during the high temperature cell-fabrication process.[69]

In an effort to develop alternative anodes that can withstand sulfur contamination and carbon deposition with hydrocarbon fuels, some perovskite or perovskite-related oxide materials have been explored as anode. For example, $La_{0.75}Sr_{0.25}Cr_{0.5}Mn_{0.5}O_3$ (LSCM) perovskite oxide has been found to exhibit performance comparable to the Ni-YSZ cermet anode at $T > 800$ °C.[70] More importantly, the LSCM anode also shows stable performance in methane. Recently, $Sr_2MgMoO_{6-\delta}$ double perovskite anode has been found by Goodenough's group to exhibit good activity.[71] This double perovskite anode shows stable performance in dry methane and good tolerance to sulfur at $T > 750$ °C. However, their catalytic activity and resistivity against carbon-deposition and sulfur impurity at low temperatures ($T < 700$ °C) need to be investigated further.

1.4 MOTIVATION AND OBJECTIVE OF THIS WORK

Intermediate temperature (500 – 800 °C) SOFC technology is confronted with severe materials challenges as the conventional materials used in high temperature (~ 900 °C) SOFC are hampered by inadequate performance at 500 – 800 °C. For example, the slow oxygen reduction reaction at the cathodes at intermediate temperatures is one of the serious problems.

In this regard, the cobalt-containing perovskite cathodes such as $La_{1-x}Sr_xCoO_{3-\delta}$ (LSC) are appealing as they show good oxide ion conductivity compared to LSM at the intermediate temperatures (500-800 °C). However, the use of LSC in practical SOFC is plagued by its high TEC > 20×10^{-6} $^{o}C^{-1}$ compared to that of the electrolytes.[3-6] Development of alternative cathodes with adequate catalytic activity and acceptable TEC is a critical issue for the successful development of the intermediate temperature SOFC technology.

With this perspective, this dissertation focuses on the following:

- Design and synthesis of alternative cathode materials with a layered perovskite structure such as $LnBaCo_2O_{5+\delta}$ (Ln = lanthanide) and a modification of their compositions ($LnBa_{1-x}Sr_xCo_{2-y}M_yO_{5+\delta}$) to tune further the crystal structure, thermal properties, and performance parameters for SOFC applications
- Design and synthesis of non-perovskite oxide cathode materials such as $RBa(Co,M)_4O_7$ (R = Y, Ca, In, M = Zn, Fe, Al) with a hexagonal structure and characterization of their MIEC properties for application as cathodes in SOFC
- Investigation of the crystal chemistry of synthesized cathode materials including high temperature structural analysis and possible phase transitions
- Investigation of the oxygen-transport mechanism of the cathode materials by oxygen permeation measurements
- Characterization of their thermal and electrochemical properties
- Evaluation of their cathode performance with single cell SOFCs

CHAPTER 2

Experimental Techniques

2.1 MATERIALS SYNTHESIS

The various cathode materials presented in this dissertation were synthesized by conventional solid-state reactions. The conditions and procedures employed varied depending on the material system. While the general procedures are given in this Chapter, more details of the synthesis will be given in the relevant Chapters.

For the NiO-$Ce_{0.9}Gd_{0.1}O_{1.95}$ (10GDC) cermet (Ni:10GDC = 70:30 vol %) anode, GDC was synthesized by the glycine-nitrate combustion method.[72,73] The method involved the addition of glycine to a dilute nitric acid solution of required amounts of Gd_2O_3 and $(NH_4)_2Ce(NO_3)_6$, followed by an evaporation of water and a self-sustaining combustion of the solid mass on a hot plate. The residual carbon was then removed by calcining at 600 ^oC for 2 h in air. The thus obtained 10GDC powders were then mixed with appropriate amounts of NiO using ball-milling for 3 days.

The $La_{0.8}Sr_{0.2}Ga_{0.8}Mg_{0.2}O_{2.8}$ (LSGM) electrolyte was prepared by firing required amounts of La_2O_3, $SrCO_3$, Ga_2O_3, and MgO at 1100 ^oC for 5 h, followed by pelletizing and sintering at 1500 ^oC for 10 h. The $Ce_{0.8}Gd_{0.2}O_{1.9}$ (GDC) electrolyte was prepared by firing required amounts of Gd_2O_3 and CeO_2 at 1600 ^oC for 8 h.

2.2 CRYSTAL STRUCTURE ANALYSIS

The crystal structures of the synthesized materials were analyzed by X-ray powder diffraction (XRD) techniques. The XRD data were refined with the Rietveld method with the Fullprof program.[74]

2.2.1 X-ray Powder Diffraction

Room temperature X-ray diffraction (XRD) was carried out using Philips Model APD 3520 or Phlips X′Pert diffractometer with Cu Kα radiation. High temperature XRD was carried out using a Scintag X1 or an Anton Paar HTK-10 camera coupled to a Philips PW1700 diffractometer with Cu Kα radiation. For the high temperature XRD measurements, powder samples were mounted on platinum or platinum-rhodium alloy ribbon and resistively heated in the range of 20 – 1000 °C in air. At each step, the temperature was kept constant until no variations in the diffraction patterns were detected. Similar procedure was utilized during the cooling process as well.

Crystal structures of the samples were first checked by matching measured XRD patterns with the XRD database at the International Centre for Diffraction Data (ICDD) using the JADE 7 software.

2.2.2 Rietveld Refinement

Further crystal chemistry of the samples was analyzed by the Rietveld refinement method with the Fullprof program.[74] The XRD patterns for the Rietveld refinement were recorded using a fixed slit and stepwise scan method with a slow scan rate (~ 10 seconds per 0.03°) to improve the signal-to-noise ratio.

The Rietveld method is a least squares refinement process to match the experimental data with the calculated pattern. The aim of the refinement procedure is minimizing the sum of differences in numerical intensity (y_i) between the observed and calculated values:[75,76]

$$S = \sum_i w_i(y_i(obs) - y_i(calc))^2 \tag{2.1}$$

where $y_i(obs)$ and $y_i(calc)$ are the observed and calculated intensities, respectively, at the ith data point and w_i is the weight assigned at the ith data point.

$$w_i = (y_i(obs))^{-1} \tag{2.2}$$

During the refinement procedure, the entire XRD pattern including background is refined using various parameters. The Rietveld method is based on a known structure model and the starting parameters on the crystal structure should be reasonable. Therefore, structural parameters reported in the literature were adopted as starting values.

The shapes of the peaks can be fitted using the Gaussian or Lorentzain functions. However, real peak shape can be described better by employing a mixed model such as Pseudo-Voigt. Table 2.1 shows the different shape functions. During the Rietveld refinement of the XRD patterns, the Pseudo-Voigt shape function was employed.

Table 2.1 Various shape function commonly used in the Rietveld method.[75,76]

Gaussian	$G = I_0 \exp\left(-\ln 2 \left(\frac{2\Theta - 2\Theta_0}{FWHM/2} \right)^2 \right)$
Lorentzian	$L = I_0 \left(1 + \left(\frac{2\Theta - 2\Theta_0}{FWHM/2} \right)^2 \right)^{-n}$
Pseudo-Voigt	$V = \eta L + (1-\eta)G \quad (0 \le \eta \le 1)$
Pearson VII	$P = I_0 \left(1 + \left(\frac{2\Theta - 2\Theta_0}{ma^2} \right)^2 \right)^{-m}$

I_0 is peak intensity, $2\Theta_0$ is peak position, 2Θ-$2\Theta_0$ is the Bragg angle with its origin at the $2\Theta_0$ position, *FWHM* is the full width at half maximum of the peak, η is the mixing parameter between Gaussian and Lorentzian, and m is the shape parameter.

2.3 IODOMETRIC TITRATION

The oxygen content and average oxidation state of the transition metal ions in the samples were determined by iodometric titration at room temperature.[77,78] The sample powders were dissolved in 15 mL of 10 % KI solution. After adding 10 mL of 3.5 N HCl, the solution was stirred until the sample dissolved completely. The clear solution was then titrated against 0.03 N sodium thiosulfate ($Na_2S_2O_3$) solution using starch as an indicator.

2.4 THERMAL ANALYSIS

2.4.1 Thermogravimetric Analysis

Weight changes of the samples during heating and cooling were monitored with a Perkin-Elmer Series 7 thermogravimetric analyzer and a Netzsch STA 449 F3 instrument. Thermogravimetric analysis (TGA) was carried out from room temperature to 1000 ^{o}C with a heating/cooling rate of 2-4 ^{o}C/min in air or nitrogen. The variations in the actual oxygen content and the oxidation state of the transition metal ions in the samples were derived using the initial room-temperature oxygen content values determined by the iodometric titration and the TGA data.

2.4.2 Thermal Expansion Measurements

Thermal expansion behavior of the samples was measured with a dilatometer or a thermomechanical analyzer (TMA). The specimens for the thermal expansion measurement were prepared as cylinder-shape pellets with a height of > 5 mm. Thermal expansion coefficient (TEC) of the sample was determined as

$$\alpha = \frac{1}{L_0}\frac{dL}{dT} \tag{2.3}$$

where α is the TEC, L_0 is the length of the specimen at a specific temperature, and T is the absolute temperature. The average TECs of the specimens were measured for three consecutive heating/cooling cycles in the temperature range of 80 – 900 °C with a heating/cooling rate of 3 °C/min and an intermediate dwelling at 900 °C for 0.5-1 h.

2.5 ELECTROCHEMICAL ANALYSIS

2.5.1 Electrical Conductivity Measurement

The electrical conductivity was measured with a four-probe dc method using the Van der Pauw configuration on heating/cooling in air.[79,80] The schematic Van der Pauw configuration is shown in Figure 2.1. The specific resistivity ρ of a flat sample can be calculated as[79]

$$\rho = \frac{\pi d}{\ln 2} \frac{(R_{AB,CD} + R_{BC,DA})}{2} f\left(\frac{R_{AB,CD}}{R_{BC,DA}}\right) \qquad (2.4)$$

where R is the resistance, and d is the thickness of the sample, and f is a function of the ratio $R_{AB,CD}/R_{BC,DA}$ (see Figure 2.1)

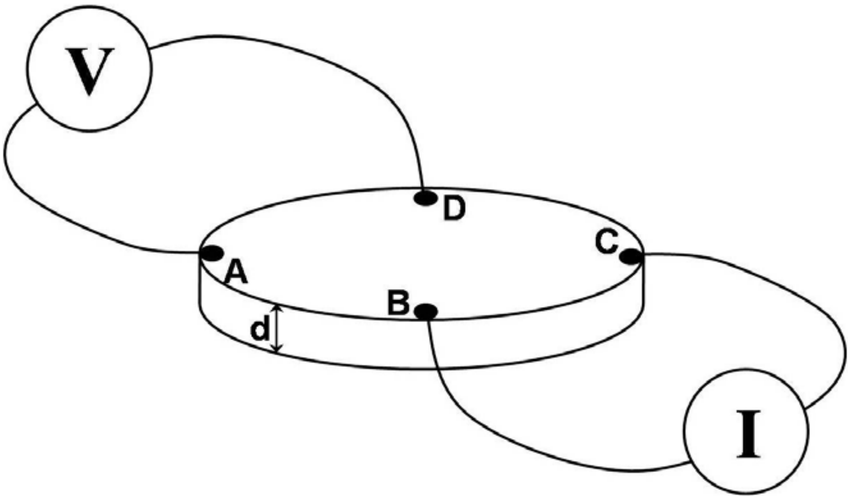

Figure 2.1 Schematics of the Van der Pauw configuration.

Assuming the four probes are equally located in a square on a disc type sample, $f\left(\frac{R_{AB,CD}}{R_{BC,DA}}\right)$ equals to 1, and then the conductivity σ can be calculated as

$$\sigma = \frac{1}{\rho} = 0.2207 \frac{I}{V \cdot d} \qquad (2.5)$$

where I is the applied current, V is the measured voltage, and d is the sample thickness.

2.5.2 AC -impedance Spectroscopy

The polarization resistance (R_p) of the cathode in contact with electrolyte pellets was measured in the temperature range of 400 – 800 ^oC by AC impedance spectroscopy (Solartron 1260 FRA). The polarization was measured using a two or three electrode configuration. Pt mesh and paste were used as both the current collector and the reference electrode.

2.5.3 Oxygen Permeation Measurement

Oxygen permeation measurement was carried out with coin-type mixed oxide ion and electronic conducting (MIEC) pellets with a theoretical density of > 90 %. The specimen was mounted on the top of a supporting alumina tube with a pyrex glass ring (see Figure 2.2). An alumina ring with the same inner diameter as the pyrex glass ring was also used as a weight to keep the seal leak-tight while maintaining the same permeation area on both sides of the pellet. To eliminate edge effects,[81] the edge of the sample pellet was sealed using a glass paste. While one side of the pellet was open to air (pO_2'), the other side was exposed to a lower oxygen partial pressure (pO_2'') that was controlled by regulating the helium gas flow inside the alumina tube. The resulting oxygen permeation flux was measured with a gas chromatograph (GC, SRI 8610C). Any nitrogen detected in the carrier gas was used to correct the oxygen flux (jO_2) values for air leaks.

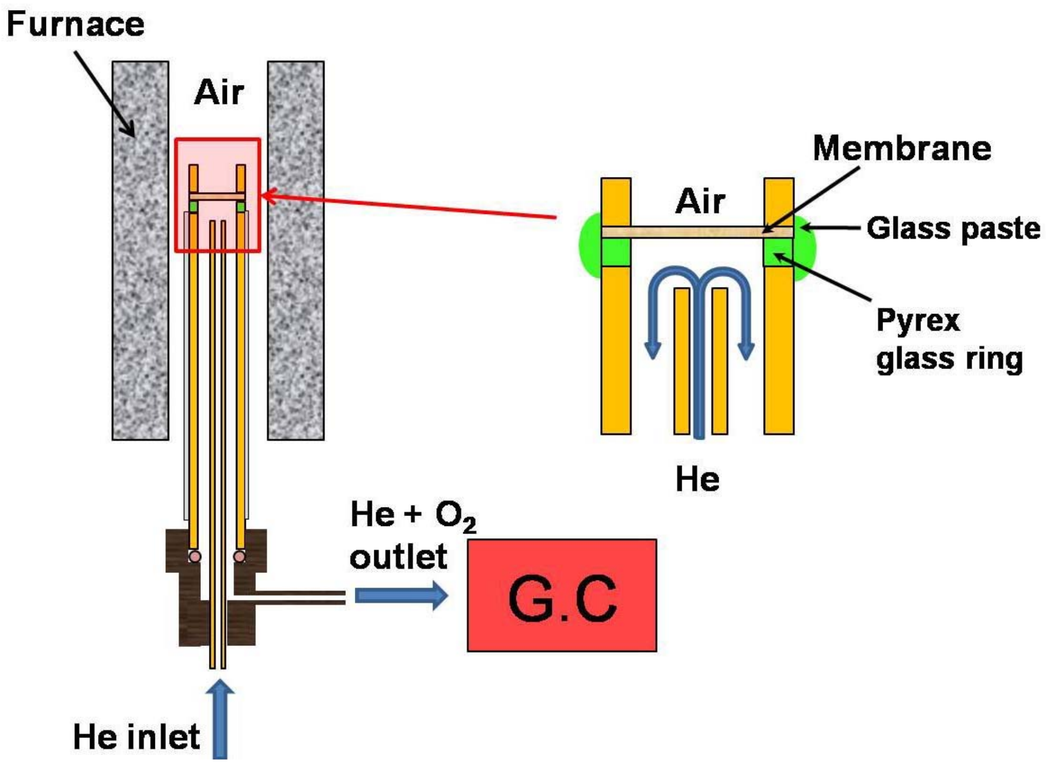

Figure 2.2 Schematic configuration of the oxygen permeation measurement set-up.

2.5.4 Single Cell Performance Test

Fuel cell performances of various cathodes were evaluated with LSGM or GDC electrolyte supported single cells. The sintered LSGM or GDC electrolyte pellets with densities of > 95% of the theoretical value were ground and polished to 0.4-0.5 mm thickness. The cathode powders synthesized were ball milled for 1-3 days in ethanol using zirconia milling media. All the electrode materials were mixed with an organic binder (Heraeus V006) to form a slurry and then applied onto both the sides of a dense electrolyte pellet by screen printing. For the LSGM-supported single cell, a $La_{0.4}Ce_{0.6}O_{1.8}$ (LDC) buffer layer was first prepared by screen printing onto the anode side of the LSGM electrolyte to prevent the formation of $LaNiO_3$ or La_2NiO_4 at the anode|electrolyte interface.[82] The NiO + 10GDC cermet anode was screen printed onto the LDC layer and heated at 1300 °C for 1 h. Similarly, to prevent the side reaction between some cathode materials and LSGM, a GDC buffer layer was applied by screen printing onto the cathode side of the LSGM electrolyte and heating at 1200 °C for 2 h.[48] The specific firing temperature of various cathode compositions will be described in the respective chapters. The geometrical area of the electrode was 0.25 cm^2. Pt meshes and wires were attached to each electrode using Pt paste as current collector and reference. During the single SOFC operation, humidified H_2 (~3 % H_2O at 25 °C) and air were supplied, respectively, as fuel and oxidant at a rate of 100 cm^3 min^{-1}.

Current-voltage (*I-V*) measurements were carried out with a three electrode configuration consisting of a cathode, anode, and Pt reference electrode, which allowed a seperate monitoring of the cathode over-potentials during the cell operation. The schematic configuration of the test cell is shown in Figure 2.3. *I-V* and cathode over-potentials were measured *in situ* during cell operation with an Arbin BT2000/fuel cell test station.

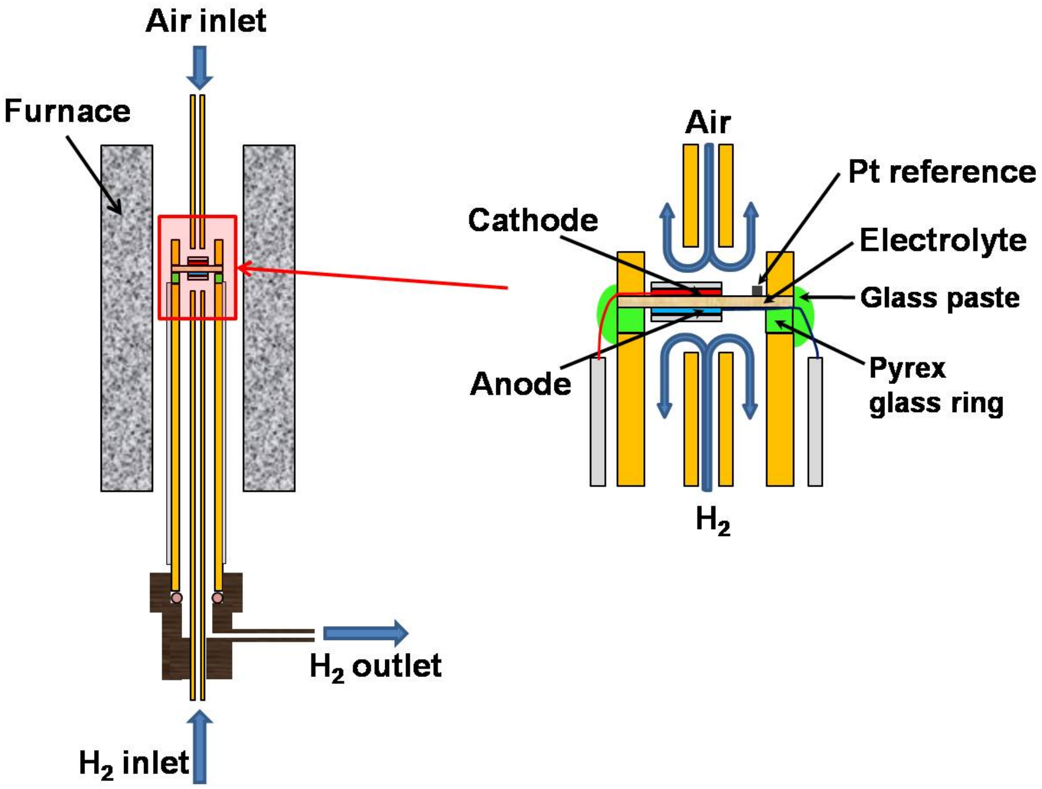

Figure 2.3 Schematic configuration of the single cell performance test set-up.

2.6 SCANNING ELECTRON MICROSCOPY

Microstructural characterization of the cathodes and the interfacial reaction analysis were carried out with a JEOL JSM-5610 scanning electron microscope (SEM) equipped with an OXFORD Instruments INCA Energy 200 X-ray detector for elemental analysis by energy dispersive spectroscopy (EDS).

PART I

LAYERED PEROVSKITE OXIDE CATHODE MATERIALS FOR INTERMEDIATE TEMPERATURE SOFC

CHAPTER 3

$LnBaCo_2O_{5+\delta}$ Oxides as Cathodes for Intermediate Temperature SOFC

3.1 INTRODUCTION

Solid oxide fuel cells (SOFCs) offer the advantage of directly using hydrocarbon fuels without requiring external fuel reforming due to the higher operating temperatures of > 500°C compared to the proton exchange membrane fuel cells. However, the intermediate-temperature SOFC technology is confronted with slow oxygen reduction kinetics with the conventional cathode materials at intermediate operating temperatures of 500–800 °C. Conventional $La_{1-x}Sr_xMnO_3$ cathodes show poor oxide ion conductivity and inadequate catalytic activity at intermediate temperatures because of the stability of Mn^{4+} ions at such temperatures and the difficulty of creating oxygen vacancies in the lattice.[28,29] In this regard, the cobalt-containing perovskite cathodes such as $La_{1-x}Sr_xCoO_{3-\delta}$ are appealing as they show good oxide ion conductivity, but the use of $La_{1-x}Sr_xCoO_{3-\delta}$ in practical SOFCs is limited due to its much higher thermal expansion coefficient (TEC) compared to that of the yttria-stabilized zirconia electrolyte.[39,40] Development of alternative cathodes with adequate catalytic activity and acceptable TEC is a critical issue for the successful development of intermediate-temperature SOFC technology.

Recently, several groups have focused extensively on the structural aspects and low-temperature electrical and magnetic properties of $LnBaCo_2O_{5+\delta}$ (Ln = Pr, Nd, Sm, Eu, Gd, Tb, Dy, Ho, and Y) oxides.[83-88] These oxides have perovskite-related structures with varying oxygen contents $5+\delta$, depending on the Ln^{3+} ion and synthetic conditions. Figure 3.1 shows the crystal structure of the $LnBaCo_2O_{5+\delta}$ oxides, in which the Ln^{3+} and Ba^{2+} ions occupy alternate layers of the perovskite lattice along the c-axis, as indicated by high-resolution transmission electron microscopy and neutron diffraction data.[85,86] The oxide ion vacancies are exclusively located in the Ln^{3+} layers due to the smaller size of Ln^{3+} ions compared to that of Ba^{2+} ions, which results in the formation of chains of CoO_5 square pyramids and CoO_6 octahedra.[85,86] It is possible that these oxides could exhibit a combination of high electronic and oxide ion conductivity. However, despite the extensive low-temperature studies, not much data are available on their high-temperature electrical properties. Moreover, this new class of materials has not been explored for use as cathodes for SOFCs. We present in this paper a systematic investigation of the high-temperature properties of the $LnBaCo_2O_{5+\delta}$ series of oxides with Ln = La, Nd, Sm, Gd, and Y, and an exploration of their use as cathodes for intermediate-temperature SOFCs. The influence of the Ln^{3+} ions on the structure, oxygen content, TEC, electrical conductivity, and catalytic activity for the oxygen reduction reaction in SOFCs is discussed.

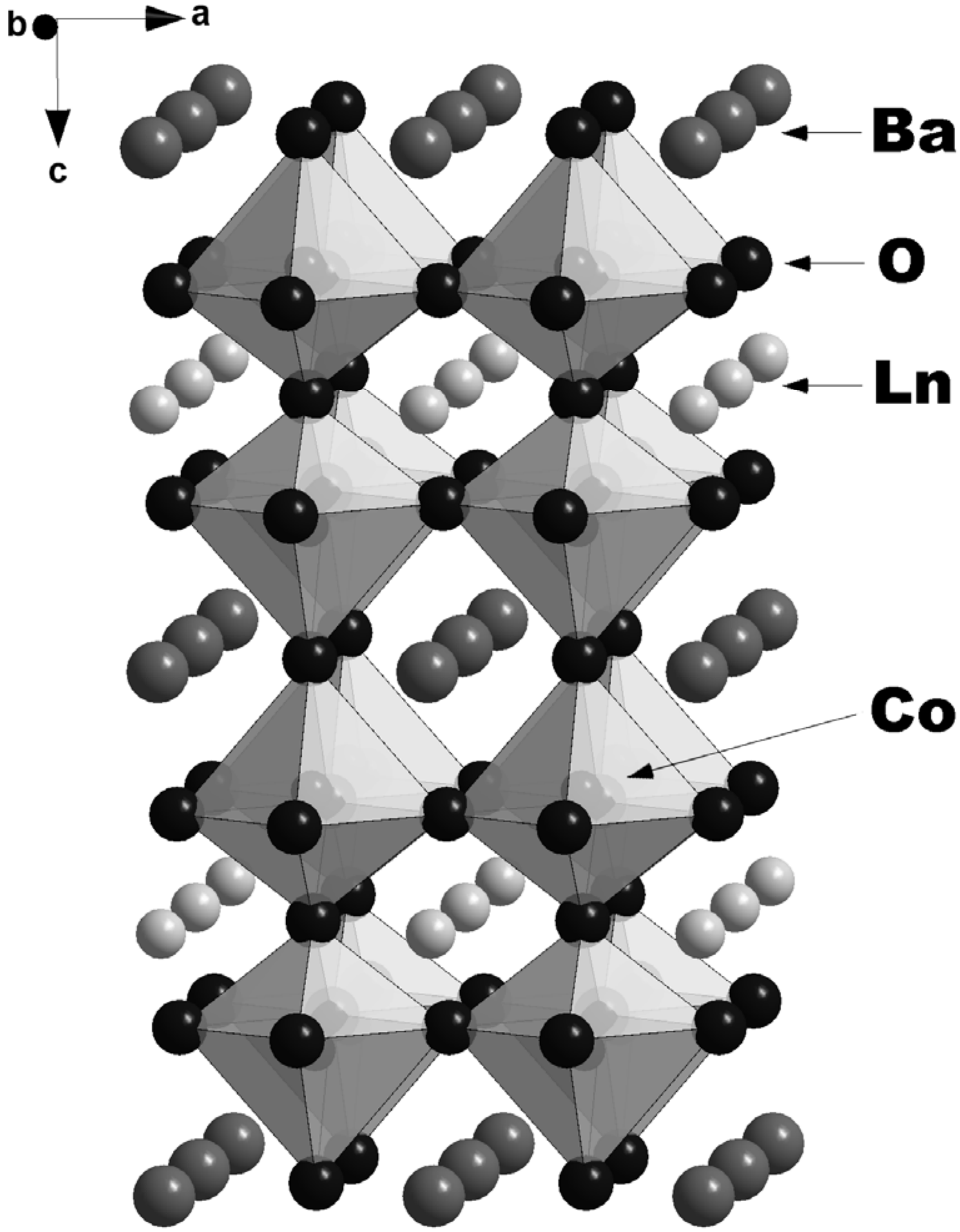

Figure 3.1 Crystal structure of the ordered $LnBaCo_2O_{5+\delta}$.

3.2 EXPERIMENTAL

3.2.1 Materials Synthesis

The $LnBaCo_2O_{5+\delta}$ (Ln = La, Nd, Sm, Gd, and Y) oxides were synthesized by conventional solid-state reaction methods. Required amounts of the lanthanide oxides (La_2O_3, Nd_2O_3, Sm_2O_3, Gd_2O_3, or Y_2O_3), $SrCO_3$, and Co_3O_4 were thoroughly mixed with ethanol using an agate mortar and pestle and calcined at 1000 ^oC for 12 h in air. The calcined powders were then ground, pressed into pellets, and finally sintered at 1100 ^oC for 24 h. The $La_{0.8}Sr_{0.2}Ga_{0.8}Mg_{0.2}O_{2.8}$ (LSGM) electrolyte disks, the NiO-10GDC cermet anode, and LDC powder were synthesized as described in Chapter 2.

3.2.2 Characterization

The synthesized $LnBaCo_2O_{5+\delta}$ samples were characterized by XRD, iodometric titration, TGA, TMA, electrical conductivity, SEM, and single cell performance measurements as described in Chapter 2. The specimens for the reactivity tests were obtained by mixing the $LnBaCo_2O_{5+\delta}$ and the LSGM electrolyte powders in a 1:1 weight ratio, followed by heating in air at 1100 ^oC for 0.5 h and 1000 ^oC for 3 h.

3.2.3 Fabrication of Single Cells

Single cells consisting of $LnBaCo_2O_{5+\delta}$ | $LnBaCo_2O_{5+\delta}$ + LSGM | LSGM(520 μm thickness) | LDC|Ni + 10GDC were fabricated as described in Chapter 2. The composite layer ($LnBaCo_2O_{5+\delta}$: LSGM = 1 : 1 wt. ratio) and the $LnBaCo_2O_{5+\delta}$ cathode were heated, respectively, at 1100 °C for 0.5 h and 1000 °C for 3 h.

3.3 RESULTS AND DISCUSSION

3.3.1 Crystal Structure and Oxygen Content Analysis

Figure 3.2 shows the XRD patterns of the $LnBaCo_2O_{5+\delta}$ (Ln = La, Nd, Sm, Gd, and Y) samples and Table 3.1 gives their structural data. All the reflections of the Ln = La sample could be indexed with a cubic structure, suggesting a lack of long-range ordering between La^{3+} and Ba^{2+} ions in the perovskite lattice.[83,89] Furthermore, iodometric titration indicated the room-temperature oxygen content to be 6.0 (Table 3.1) without any oxygen vacancies ($\delta = 1.0$) in the perovskite lattice. The reflections of the Ln = Nd samples could be indexed with a tetragonal structure, suggesting an ordering between Nd^{3+} and Ba^{2+} ions along the *c*-axis.[85,87] Iodometric titration indicated a room temperature oxygen content of 5.78 (Table 3.1), and with cation ordering, the oxide ion vacancies were predominantly located in the Nd^{3+} layer. Similarly, the reflections of the Ln = Sm and Gd samples could be indexed with an orthorhombic structure while those of the Ln = Y sample could be indexed with a tetragonal structure, implying cation ordering in the Ln = Sm, Gd, and Y samples as well. Iodometric titration indicated that the room-temperature oxygen content decreased from 6.0 for Ln = La to 5.41 for Ln = Y, which is consistent with the decreasing ionic radius from La^{3+} to Y^{3+} and a consequent preference for lower coordination numbers. The unit cell volume in Table 3.1 decreases upon changing from Ln = La to Y, which is consistent with the decreasing size of the Ln^{3+} ions. Although the decreasing oxygen content from Ln = La to Gd would be expected to increase the unit cell volume due to the reduction of the smaller Co^{4+} ions into the larger Co^{3+} ions, the decreasing size of the Ln^{3+} ions play a dominant role in controlling the overall unit cell volume.

3.3.2 Thermal and Electrical Properties

Figure 3.3 compares the TGA plots of the $LnBaCo_2O_{5+\delta}$ (Ln = La, Nd, Sm, Gd, and Y) samples recorded in air. All the samples experience weight loss above about 200 °C due to the loss of oxygen from the lattice except for the Ln = Y sample that shows a slight initial weight gain before losing oxygen. This is because of the incomplete oxygen absorption during the cooling of the Ln = Y sample in the furnace, following the synthesis firing at 1100 °C. All the $LnBaCo_2O_{5+\delta}$ samples show nearly the same weight loss of 1.3–1.4 % upon heating to 900 °C in air.

Table 3.1 Structural parameters, oxygen content, and TEC of the $LnBaCo_2O_{5+\delta}$ oxides.

Ln	Space group	*a* (Å)	*b* (Å)	*c* (Å)	V(Å^3)	Oxydation state of Co	Oxygen content (5+δ)	TEC (× 10^{-6} / $^{o}C^{-1}$)	
								80 – 900°C	500 – 900°C
La*	*Pm*-3*m*	3.881	–	–	58.456	3.50	6.00	24.3	29.8
Nd	*P*4/*mmm*	3.895	–	7.611	115.467	3.28	5.78	19.1	21.1
Sm	*Pmmm*	3.880	3.907	7.559	114.588	3.15	5.65	17.1	18.7
Gd	*Pmmm*	3.873	3.912	7.529	114.073	3.07	5.57	16.6	16.8
Y	*P*4/*mmm*	3.874	–	7.483	112.304	2.91	5.41	15.8	14.9

* Lattice parameter and volume are based on the chemical formula of $La_{0.5}Ba_{0.5}CoO_3$. For other samples, the structural data are based on the chemical formula of $LnBaCo_2O_{5+\delta}$.

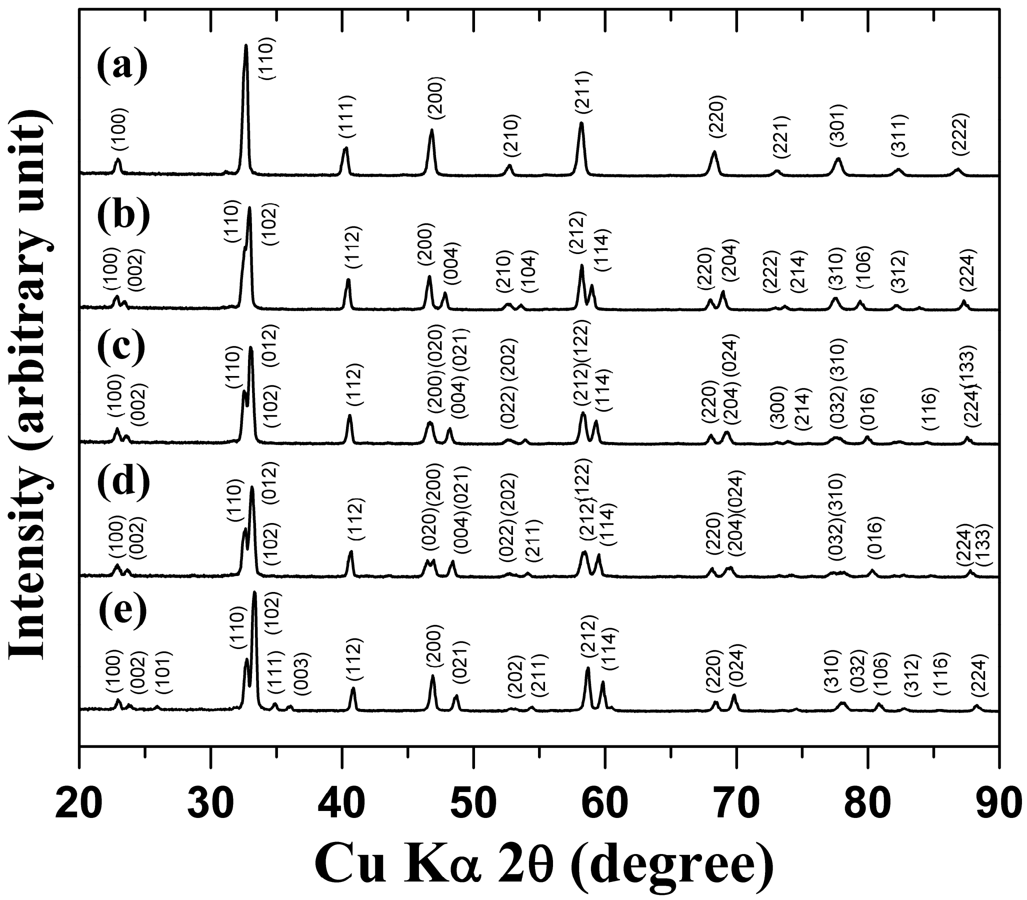

Figure 3.2 X-ray powder diffraction patterns of the $LnBaCo_2O_{5+\delta}$ samples: (a) Ln = La, (b) Ln = Nd, (c) Ln = Sm, (d) Ln = Gd, and (e) Ln = Y.

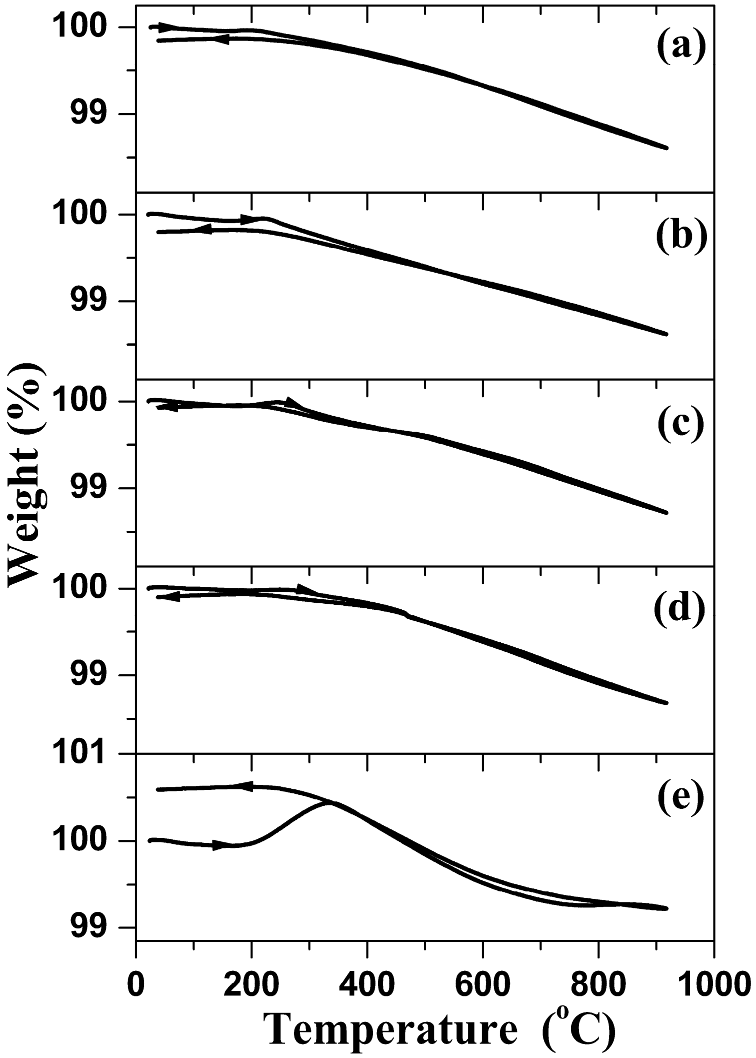

Figure 3.3 TGA plots of the $LnBaCo_2O_{5+\delta}$ samples, recorded in air with a heating/cooling rate of 3 °C/min.: (a) Ln = La, (b) Ln = Nd, (c) Ln = Sm, (d) Ln = Gd, and (e) Ln = Y.

Figure 3.4 shows the variations of the oxygen content and oxidation state of cobalt with temperature in air for the various $LnBaCo_2O_{5+\delta}$ samples. These curves were derived using the initial oxygen content values determined by the iodometric titration and the TGA data. The samples lose 0.3–0.4 oxygen atoms per formula unit upon heating to 900°C. However, the oxidation state of cobalt at 900°C decreases significantly on going from from Ln = La to Y due to the decreasing initial, room temperature oxygen content values. For example, while the oxidation state of cobalt decreases from +3.50 to +3.09 for Ln = La, it decreases from +3.07 to +2.73 for Ln = Gd upon heating to 900°C. In fact, the oxidation state of cobalt is lower than +3 at $T > 660$°C for Ln = Nd, Sm, Gd, and Y in $LnBaCo_2O_{5+\delta}$.

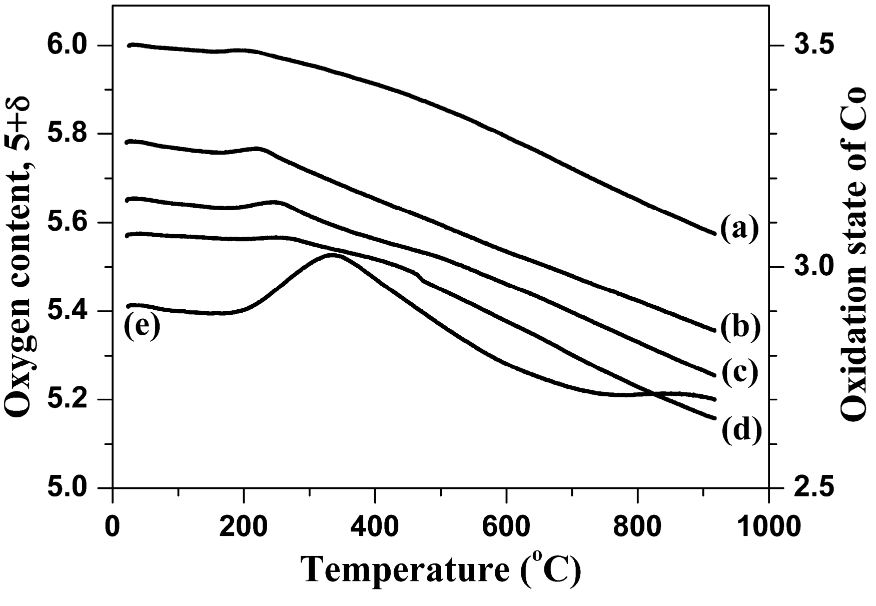

Figure 3.4 Variations of the oxygen content and the oxidation state of cobalt with temperature in air: (a) Ln = La, (b) Ln = Nd, (c) Ln = Sm, (d) Ln = Gd, and (e) Ln = Y.

The thermal expansion behaviors of the $LnBaCo_2O_{5+\delta}$ samples in air are shown in Figure 3.5, and the average TEC values are given in Table 3.1 for two different temperature ranges, 80–900 and 500–900°C. The TEC values decrease significantly with the shift from Ln = La to Y in both temperature ranges. The decrease in TEC is due to the decrease in the ionicity of the Ln–O bonds as the ionic bonds generally exhibit larger thermal expansion than covalent bonds. Similar trends with Ln–O bond ionicity have been observed with various $La_{1-x}A_xMnO_3$ systems in the literature.[90-92] Comparing the data in the two temperature regions, the average TEC values in the 500–900°C range are higher than those in the 80–900°C range for the Ln = La, Nd, Sm, and Gd samples, which could be partly due to the loss of oxygen from the lattice at higher temperatures (Figure 3.4). However, the difference between the two regions becomes smaller with the change from Ln = La to Gd, although the amount of oxygen loss does not vary significantly. In addition, the Ln = Y sample shows slightly lower TEC in the high-temperature region, partly due to a lower amount of oxygen loss from the lattice compared to that in the samples with Ln = La, Nd, Sm, and Gd.

Figure 3.6 shows the variations of electrical conductivity with temperature up to about 900°C for the $LnBaCo_2O_{5+\delta}$ samples. The conductivity increases with decreasing temperature for all the samples due to oxygen loss from the lattice. At a given temperature, the electrical conductivity decreases from Ln = La to Y due to an increasing concentration of oxygen vacancies and a consequent perturbation of the

O–Co–O interaction and carrier delocalization.[93] In addition, the decreasing size of the Ln^{3+} ions from Ln = La to Y will cause an increasing bending of the O–Co–O bonds from the ideal 180° bond angle as evidenced by the structural change from cubic to tetragonal to orthorhombic. The increasing bending can narrow the bandwidth due to a decrease in the overlap between the Co:3*d* and O:2*p* orbitals and consequently cause a decrease in electrical conductivity.[92] Although the $YBaCo_2O_{5+\delta}$ sample shows the lowest electrical conductivity, it is still higher than 250 S/cm up to 900°C, which is adequate for the material to be employed as a cathode in SOFC.

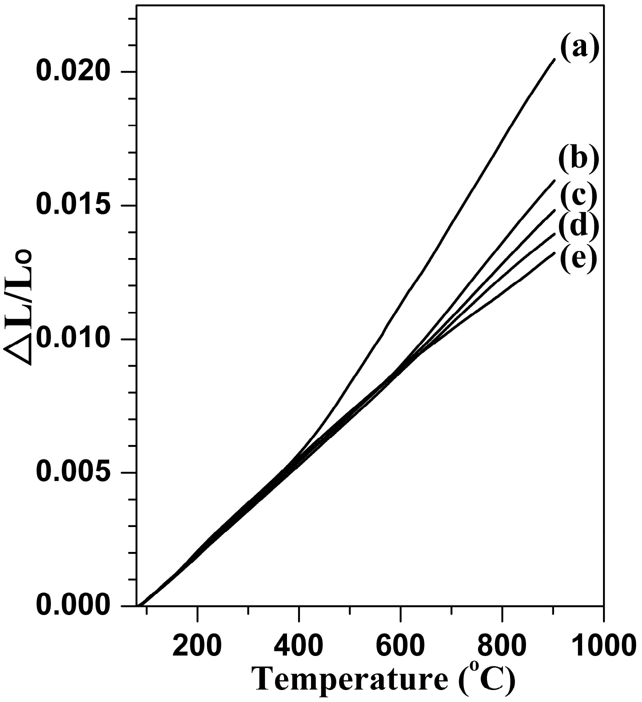

Figure 3.5 Thermal expansion ($\triangle L/L_o$) curves of the $LnBaCo_2O_{5+\delta}$ samples in the temperature range of 80 – 900 °C in air: (a) Ln = La, (b) Ln = Nd, (c) Ln = Sm, (d) Ln = Gd, and (e) Ln = Y.

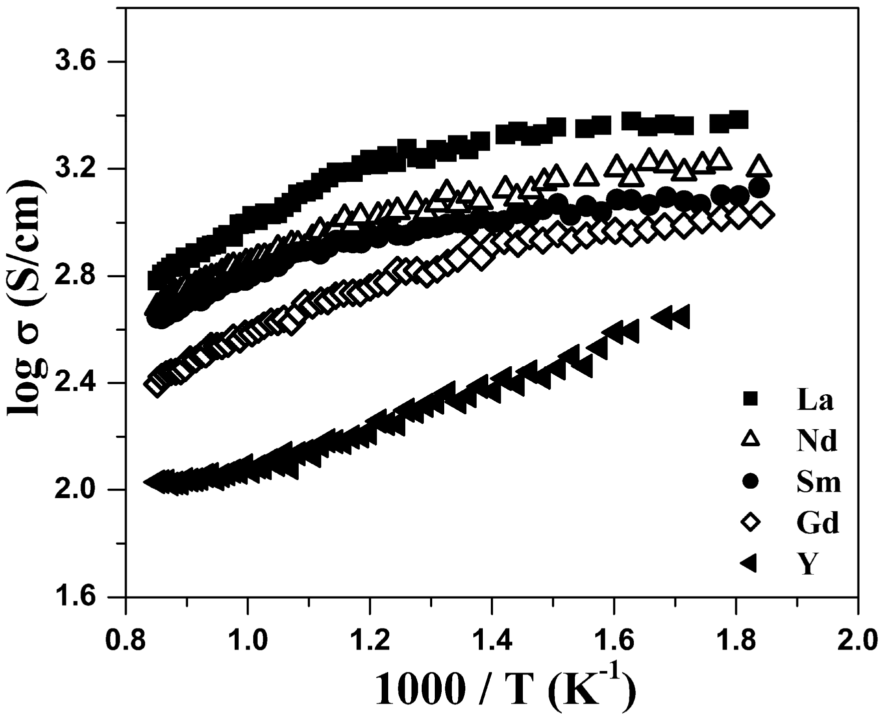

Figure 3.6 Temperature dependence of the electrical conductivities of the $LnBaCo_2O_{5+\delta}$ samples.

3.3.3 Chemical Stability and Microstructure

Before the electrochemical evaluation of the catalytic activity for the oxygen reduction reaction in single-cell SOFC, the chemical stability of the $LnBaCo_2O_{5+\delta}$ (Ln = La, Nd, Sm, Gd, and Y) cathodes in contact with the LSGM electrolyte was assessed by heating a mixture of $LnBaCo_2O_{5+\delta}$ and LSGM at 1100°C for 0.5 h and 1000°C for 3 h. Figure 3.7 shows the XRD patterns after heating the mixture at 1100°C for 0.5 h. While the Ln = La, Nd, and Sm samples do not show any reaction, the Ln = Gd sample shows a small unknown reflection at $2\theta \approx 30.2^{o}$, and the Ln = Y sample shows several new reflections, indicating an interfacial reaction between

LSGM and the Ln = Gd and Y samples. Figure 3.8 shows the XRD patterns after heating the mixture at 1000°C for 3 h. While the Ln = La, Nd, Sm, and Gd samples show no reaction products at this temperature, the Ln = Y sample indicates the formation of reaction products. These results suggest that the Ln = Y sample suffers from interfacial reaction with the LSGM electrolyte, preventing its use as a cathode in SOFC.

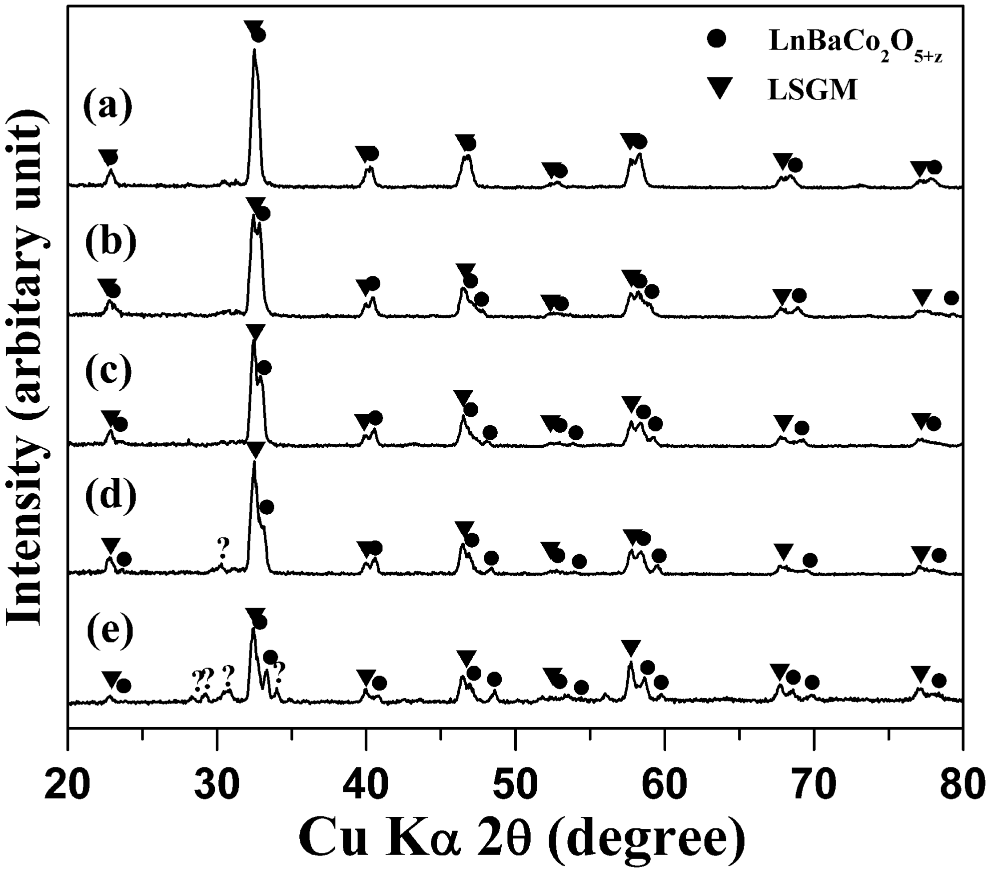

Figure 3.7 X-ray power diffraction patterns of the $LnBaCo_2O_{5+\delta}$ and LSGM mixture after firing at 1100 °C for 0.5 h in air: (a) Ln = La, (b) Ln = Nd, (c) Ln = Sm, (d) Ln = Gd, and (e) Ln = Y.

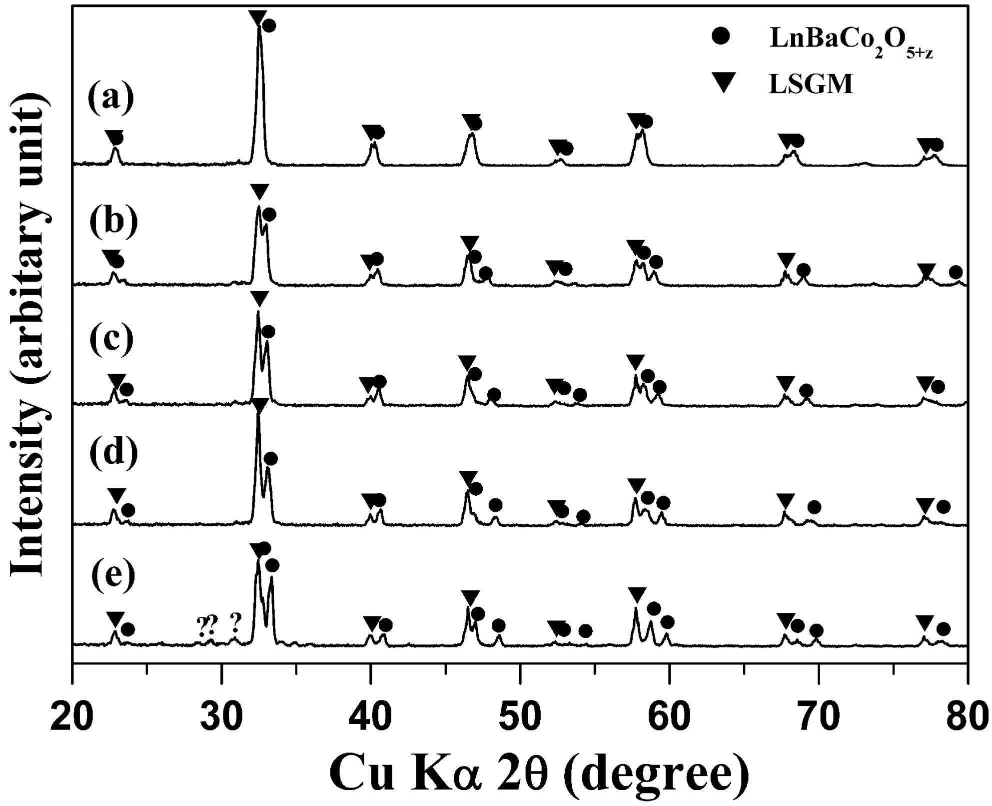

Figure 3.8 X-ray power diffraction patterns of the $LnBaCo_2O_{5+\delta}$ and LSGM mixture after firing at 1000 °C for 3 h in air: (a) Ln = La, (b) Ln = Nd, (c) Ln = Sm, (d) Ln = Gd, and (e) Ln = Y.

The microstructures of the single cells were assessed by SEM, and Figure 3.9 shows the cross sections of the cathode / composite electrode / electrolyte for Ln = La, Nd, Sm, and Gd in $LnBaCo_2O_{5+\delta}$. While the bottom of the micrograph indicates the dense, sintered LSGM electrolyte, the upper portion shows the porous cathode/composite electrodes. The SEM images indicate good bonding and continuous contact at the interfaces. It is apparent that the $LnBaCo_2O_{5+\delta}$ + LSGM composite electrodes heated at 1100°C show a larger particle size than the

$LnBaCo_2O_{5+\delta}$ cathodes heated at 1000°C, although the former helps to achieve good adhesion between the LSGM electrolyte and the cathode.

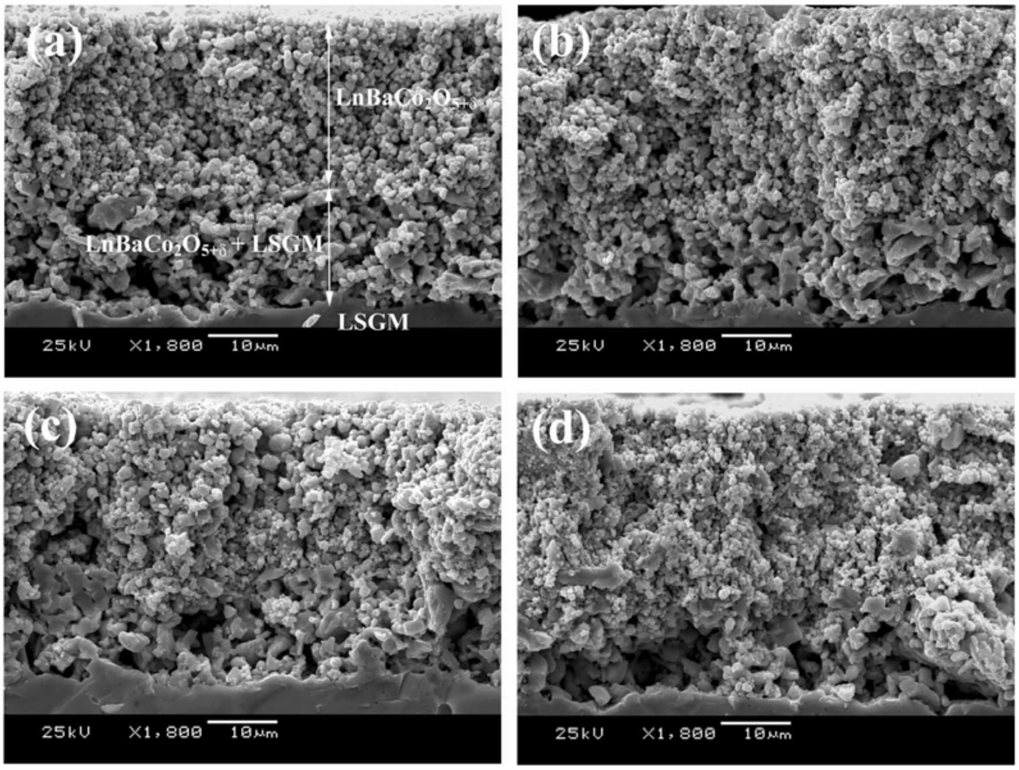

Figure 3.9 SEM micrographs showing the cross sections of the $LnBaCo_2O_{5+\delta}$/$LnBaCo_2O_{5+\delta}$-LSGM composite/LSGM portion of a single cell SOFC: (a) Ln = La, (b) Ln = Nd, (c) Ln = Sm, and (d) Ln = Gd.

3.3.4 Single Cell Performances

Figure 3.10 shows the current–voltage (*I-V*) curves and the corresponding power density curves recorded at 700, 750, and 800°C for the various $LnBaCo_2O_{5+\delta}$ cathodes. At 800°C, the maximum power density values of $LnBaCo_2O_{5+\delta}$ decrease

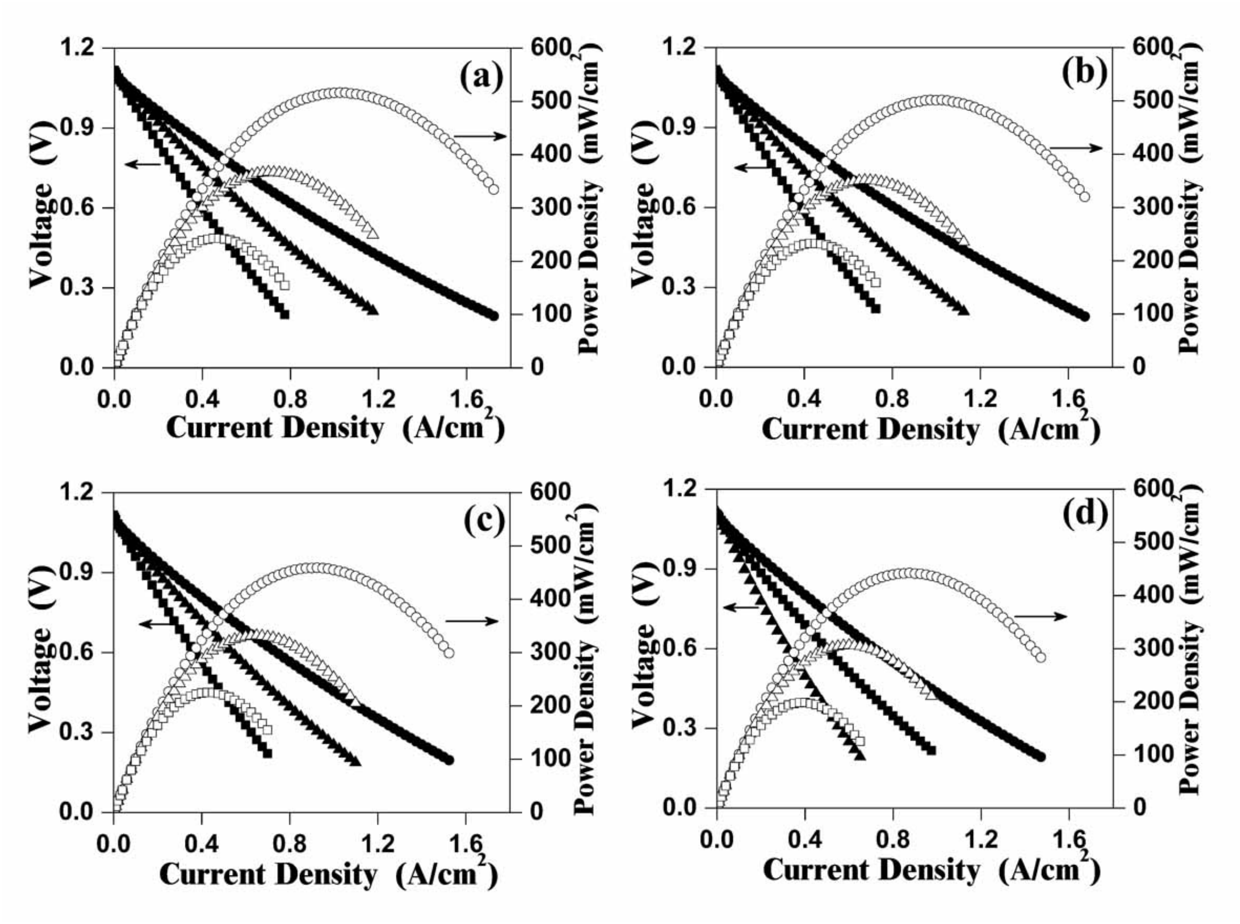

Figure 3.10 Electrochemical performance data of the $LnBaCo_2O_{5+\delta}$/$LnBaCo_2O_{5+\delta}$-LSGM/LSGM/LDC/Ni-GDC single cells at 700 °C (square), 750 °C (triangle), and 800 °C (circle): (a) Ln = La, (b) Ln = Nd, (c) Ln = Sm, and (d) Ln = Gd.

from 516 to 443 mW/cm^2 on going from from Ln = La to Gd. The oxide ion mobility and surface exchange (the adsorption/dissociation of oxygen molecules) as well as the electronic conductivity of the cathode materials are critical to maximize the electrochemical performance. However, considering the high electrical conductivity values, the differences in oxide ion conductivity may play a dominant role in determining the electrochemical performance, and future work can shed more light on this.

Despite its good electrochemical performance, the Ln = La sample may encounter a faster degradation in electrochemical performance due to the larger difference in TEC (Table 3.1) with the LSGM electrolyte ($11.4 \times 10^{-6}\ ^{o}C^{-1}$)[94], which could cause microcracks or delamination. Therefore, the $LnBaCo_2O_{5+\delta}$ cathodes with an intermediate size lanthanide ion such as Ln = Nd, Sm, and Gd may be preferred, considering a trade-off between electrochemical performance and TEC.

3.4 CONCLUSIONS

With an aim to develop new cathode materials for intermediate-temperature SOFCs, the mixed electronic–ionic conducting $LnBaCo_2O_{5+\delta}$ (Ln = La, Nd, Sm, Gd, and Y) oxides have been investigated. The room-temperature oxygen content decreases from 6.0 to 5.41 from Ln = La to Y due to a decrease in the size of the Ln^{3+} ions and the consequent preference for lower coordination numbers. Although the increasing oxygen vacancy concentration and bending of the O–Co–O bonds lead to a decrease in electrical conductivity with decreasing size of the Ln^{3+} ions, the smaller lanthanide ions provide an important advantage of lowering the thermal expansion due to a decreasing ionicity of the Ln–O bonds. The power density of single-cell SOFCs fabricated with the $LnBaCo_2O_{5+\delta}$ cathodes decreases with the decreasing size of the Ln^{3+} ions due to the decreasing electrical conductivity. The $LnBaCo_2O_{5+\delta}$ cathodes with an intermediate-size lanthanide ion like Sm^{3+} may provide a trade-off between TEC and catalytic activity.

CHAPTER 4

High Temperature Crystal Chemistry and Oxygen Permeation Properties of the Mixed Ionic-Electronic Conductors $LnBaCo_2O_{5+\delta}$ (Ln = lanthanide)

4.1 INTRODUCTION

Transition metal oxides with mixed oxide-ion and electronic conducting (MIEC) properties find unique applications as oxygen separation membranes and as electrode (cathode and anode) materials in solid oxide fuel cells (SOFC). These applications require both high electronic and oxide-ion conductivities[3,29] along with good structural and chemical stabilities[12] under the operating conditions of high temperatures and low or high oxygen partial pressures (pO_2). Particularly, mixed conductors with high oxide ion conductivity can be used as oxygen separation membranes without the use of electrodes and external circuitry required for traditional ceramic oxygen pumps. In this regard, mixed conducting oxides with perovskite or perovskite-related structures such as $Ln_{1-x}Sr_xMO_3$ (Ln = lanthanide, M = Mn, Fe, and Co),[41,94-97] $Ba_{1-x}Sr_x(Co,Fe)O_{3-\delta}$,[98,99] and $(La,Sr)_{n+1}M_nO_{3n+1}$ (n = 1 – 3 and M = Ni, Fe, and Co)[46-59] have been widely investigated as candidate materials.

Chapter 3 presented a systematic investigation of the correlation of the thermal and electrochemical properties of $LnBaCo_2O_{5+\delta}$ to the ionic size of the Ln^{3+} ions. The difference in the ionic radii between the Ln^{3+} and Ba^{2+} ions played a dominant role in determining the oxygen content values and the crystal structure. For example, the oxygen content (5 + δ) value decreases with decreasing size of the Ln^{3+} ions in the air-synthesized $LnBaCo_2O_{5+\delta}$ samples. This oxygen vacancy ordering leads to a phase transition from tetragonal to orthorhombic structure with cell dimensions of $a_p \times 2a_p \times 2a_p$ (p refers to perovskite). However, recent studies have reported that the $LnBaCo_2O_{5+\delta}$ oxides with Ln = Pr and Gd lose the oxygen vacancy ordering with a structural transition from orthorhombic to tetragonal on heating.[100,101]

In addition, the $LnBaCo_2O_{5+\delta}$ layered perovskite oxides have been gaining much attention recently due to their promising MIEC properties. Taskin *et al.*[102] reported enhanced oxygen transport behavior in layered $GdBaMn_2O_{5+\delta}$ compared to that in the disordered $Gd_{0.5}Ba_{0.5}MnO_{3-\delta}$ pervoskite. In addition, the oxide ion diffusion and surface exchange kinetics of $LnBaCo_2O_{5+\delta}$ (Ln = Pr and Gd) have been measured using $^{18}O/^{16}O$ isotope exchange depth profile, and the results showed values comparable to those of disordered perovskite oxides.[103,104] The SOFC performance data in chapter 3 suggest that the overall oxygen transport rate could decrease from La to Gd in the $LnBaCo_2O_{5+\delta}$ system. However, the oxygen transport properties of $LnBaCo_2O_{5+\delta}$ could be influenced by their high temperature structure since the ordering of oxygen vacancies will impede the oxygen transport within the lattice. Accordingly, this Chapter focuses on the high temperature crystal chemistry and the oxygen permeation properties of the $LnBaCo_2O_{5+\delta}$ (Ln = La, Pr, Nd, or Sm) oxides and a correlation of the oxygen permeation flux to the high temperature structures.

4.2 EXPERIMENTAL

4.2.1 Materials Synthesis

The $LnBaCo_2O_{5+\delta}$ (Ln = La, Pr, Nd, and Sm) oxides were synthesized by conventional solid-state reaction methods. Required amounts of the lanthanide oxides (La_2O_3, Pr_6O_{11}, Nd_2O_3, or Sm_2O_3), $BaCO_3$, and Co_3O_4 were thoroughly mixed with ethanol using an agate mortar and pestle and calcined at 1000 ^oC for 12 h in air. The calcined powders were then ground, pressed into pellets, and finally sintered at 1100 ^oC for 24 h. The resulting powders were annealed at 900 ^oC for 6 h in air, followed by slow cooling to room temperature at a rate of 1 ^oC/min to maximize the oxygen content.

4.2.2 Characterization

The synthesized $LnBaCo_2O_{5+\delta}$ samples were characterized by XRD, high temperature XRD, Rietveld refinement, iodometric titration, TGA, electrical conductivity, and oxygen permeation measurement as described in Chapter 2.

4.2.3 Oxygen Permeation Measurements

Oxygen permeation measurements were carried out using coin-type $LnBaCo_2O_{5+\delta}$ (Ln = La, Nd, and Sm) membranes with > 90 % of theoretical density as described in Chapter 2.

4.3 RESULTS AND DISCUSSION

4.3.1 Thermal and Electrical Properties

TGA experiments were carried out in air and N_2 atmospheres since the samples are exposed to air on one side and lower oxygen partial pressures on the other side during the oxygen permeation experiments. Figure 4.1 shows the variations with temperature of the oxygen contents and oxidation states of cobalt in $LnBaCo_2O_{5+\delta}$ (Ln = La, Pr, Nd, and Sm) in a flowing air and N_2 atmospheres. These curves were derived using the initial oxygen content values determined by the iodometric titration and the TGA data. The $LnBaCo_2O_{5+\delta}$ samples lose 0.41 - 0.45 oxygen atoms per formula unit on heating to 900 ^{o}C in air (Figure 4.1(a)). The amount of oxygen loss increases to 0.55 – 0.60 per formula unit on changing the atmosphere to N_2 (Figure 4.1(b)). Although the amount of oxygen loss does not vary significantly on going from Ln = La to Sm in $LnBaCo_2O_{5+\delta}$ (both air and N_2 atmospheres), the oxidation state of cobalt ions at a given temperature decreases significantly from Ln = La to Sm due to the decreasing initial, room temperature oxygen content values. It is also interesting to note that the Ln = La sample shows a linear slope in the TGA curves in both air and N_2 at $T > 300$ °C while the Ln = Pr, Nd, and Sm samples show a slight variation in slopes especially in N_2 atmosphere, which could be related to structural transitions (see later).

Figure 4.2 shows the variations of the total electrical conductivity of $\mathrm{LnBaCo_2O_{5+\delta}}$ with temperature. For the Ln = Sm sample, the sudden drop in conductivity at $T < 200$ °C is characteristic of a metal-insulator (M-I) transition, which occurs due to an ordering of the low spin $\mathrm{Co^{III}}(t_{2g}^{6}e_{g}^{0})$ and intermediate spin $\mathrm{Co^{iii}}(t_{2g}^{5}e_{g}^{1})$ ions[84,87] This M-I transition becomes less pronounced for the Ln = Nd and Sm samples and finally disappears in the Ln = La sample due to the increasing oxidation state of cobalt and the consequent decrease in oxide ion vacancy concentration and increase in the Co-O covalency and bandwidth.[91-93] All the samples show a decrease in electrical conductivity with increasing temperature for $T > 200$ °C due to an increasing concentration of oxygen vacancies. For the same reason, at a given temperature, the electrical conductivity decreases from Ln = La to Sm due to an increasing concentration of oxygen vacancies. However, as the temperature increases, the difference between the electrical conductivity values of the cation-disordered cubic and the cation-ordered layered perovskites tend to decrease, and the electrical conductivity values at ~ 900 ºC are in the range of 400 - 750 S/cm irrespective of the $\mathrm{Ln^{3+}}$ ions.

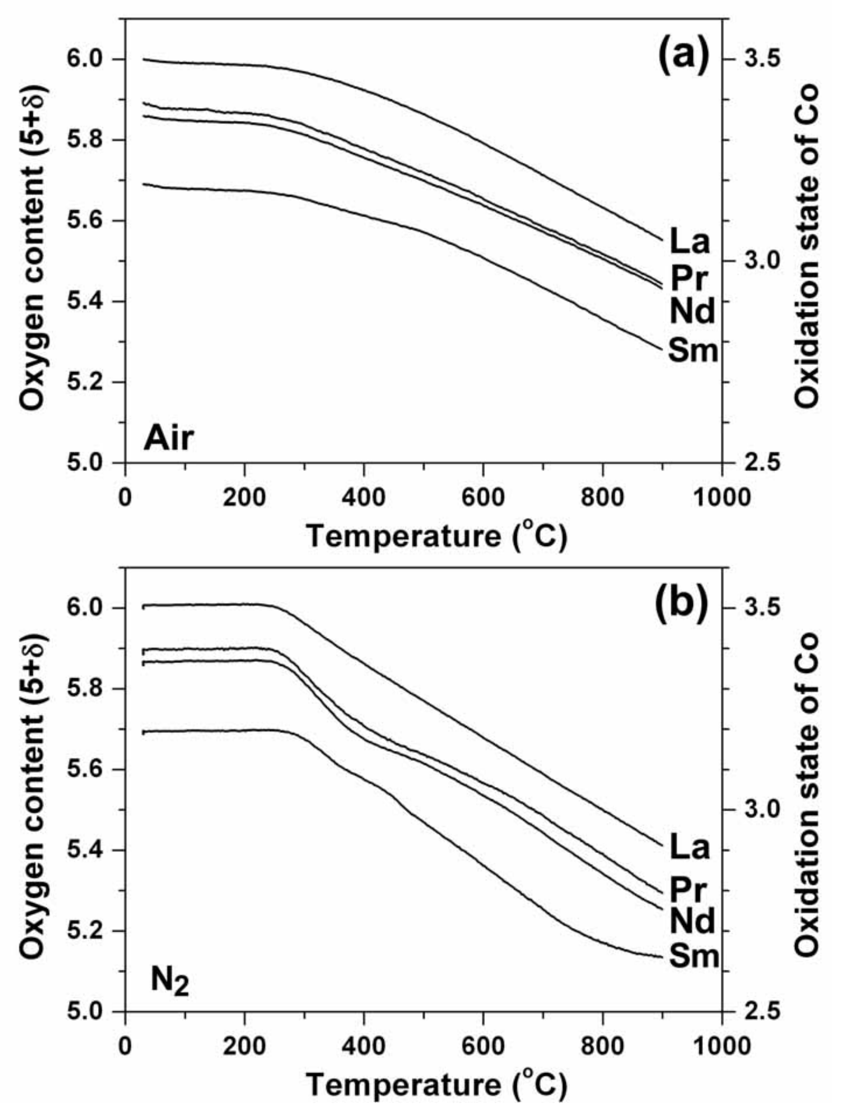

Figure 4.1 Variations of the oxygen content and the oxidation state of cobalt in $LnBaCo_2O_{5+\delta}$ (Ln = La, Pr, Nd, Sm) with temperature in (a) air and (b) nitrogen atmosphere with a $pO_2 \approx 10^{-5}$ atm.

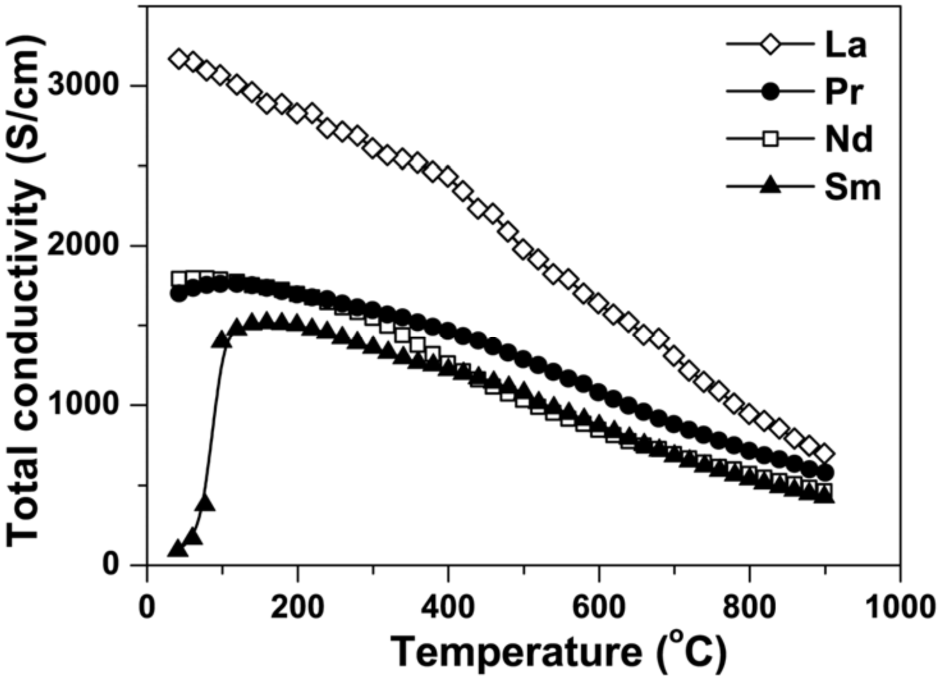

Figure 4.2 Temperature dependence of the total conductivity of $LnBaCo_2O_{5+\delta}$ (Ln = La, Pr, Nd, Sm) in air.

4.3.2 Structural Transitions

Figures 4.3 – 4.6 show the high-temperature XRD patterns and lattice parameter variations of the Ln = Pr and Nd samples in the temperature range of 20 – 900 °C in air. Both the samples have a tetragonal structure (space group: *P*4/*mmm*) at 20 °C. A recent study on the room-temperature crystallographic structure of the Ln = Pr samples has reported different phases depending on the oxygen content value.[105] For example, the Ln = Pr sample with $(5 + \delta) \approx 5.5$ showed oxygen vacancy ordering along the *b* axis with an orthorhombic (space group: *Pmmm*) cell dimensions of $a_p \times$

$2a_p \times 2a_p$. Similarly, an earlier study on the Ln = Nd sample with $(5 + \delta) = 5.69$ also suggested it to be orthorhombic (space group: *Pmmm*).[106] In our study, the Ln = Pr and Nd samples have higher room-temperature oxygen contents $(5 + \delta)$ of, respectively, 5.89 and 5.85 after annealing at 900 °C in air and show a tetragonal structure (space group: *P*4/*mmm*) with cell dimensions of $a_p \times a_p \times 2a_p$ (Figures. 4.3 and 4.5). It is likely that the high oxygen content values (close to 6.0) of the Ln = Pr and Nd samples may destroy the ordering of oxygen vacancies, resulting in a tetragonal structure. For example, the XRD pattern of the Ln = Sm sample with an oxygen content of 5.69 shows distinct peak splitting at 20 °C, which could be indexed on the basis of an orthorhombic (space group: *Pmmm*) structure in Figure 4.7. However, the low X-ray scattering factor of oxygen atoms compared to those of the heavier Ba and Ln atoms hinder us from observing the subtle orthorhombic distortion even if there is a weak ordering of oxygen vacancies. Future neutron diffraction studies will be helpful to observe the ordering of oxygen vacancies.

However, the XRD data of the Ln = Pr and Nd samples show the splitting of the (212) peak into (142) and (124) peaks, which belong to an orthorhombic (space group: *Pmmm*) phase, with increasing temperature from 20 to 200 °C. This orthorhombic distortion has been explained to be related to the M-I transition as observed from the electrical conductivity data in Figure 4.2.[85,100] Further increase in temperature leads to another phase transition from orthorhombic to tetragonal (space group: *P*4/*mmm*) in both the Ln = Pr and Nd samples. Expanded views in Figures

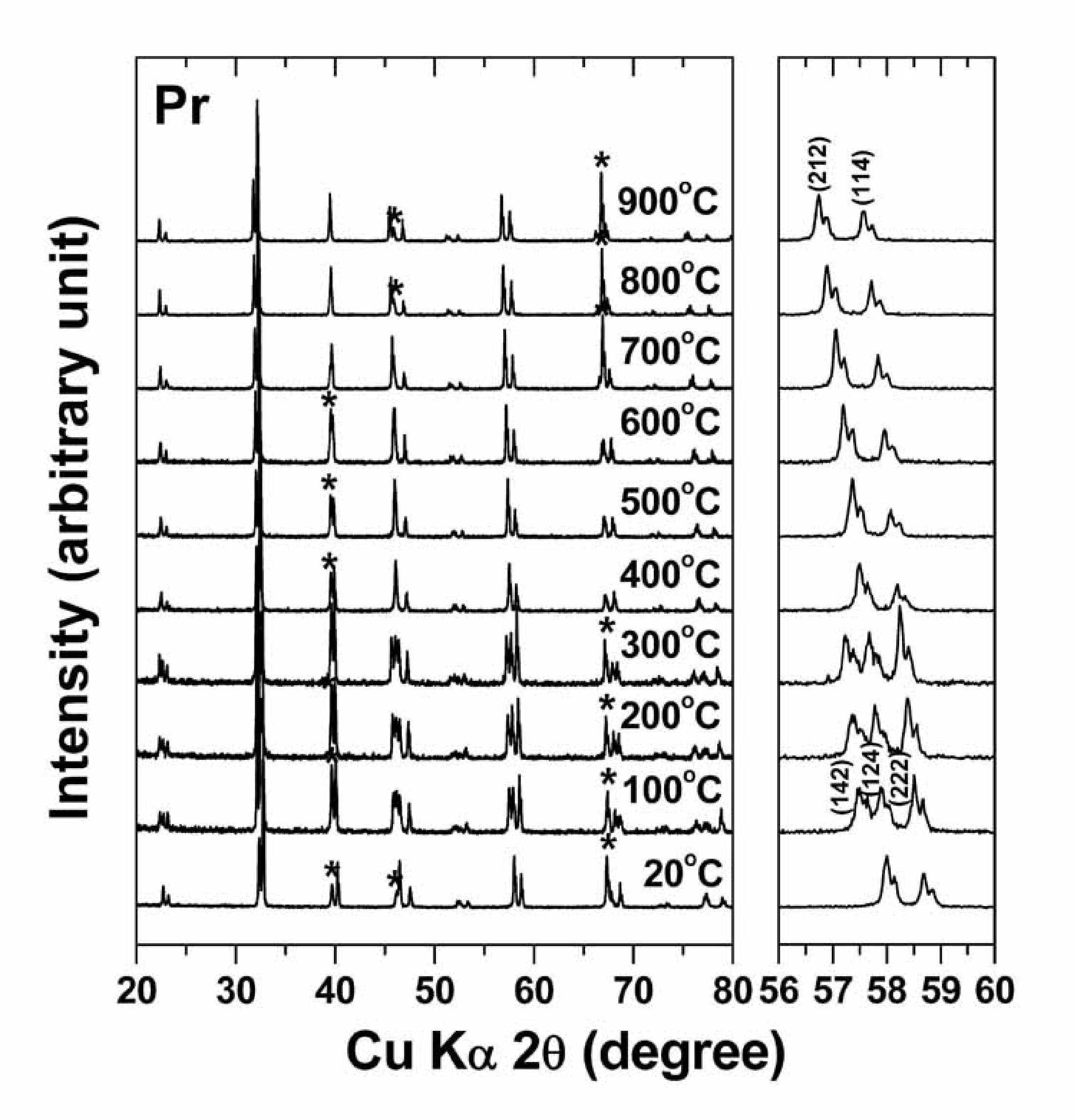

Figure 4.3 High-temperature XRD patterns of $PrBaCo_2O_{5+\delta}$ recorded with increasing temperature in air. An expanded view in the range of 56 ° ≤ 2θ ≤ 60 ° is displayed in the right panel. Reflections marked with * belong to Pt from the sample stage.

4.3 and 4.5 show that the (142) and (124) peaks of the orthorhombic phase merge again into tetragonal (212) peak at 400 °C for the Ln = Pr sample and at 500 °C for the Ln = Nd sample. Streule *et al.*[100] explained this to be due to the thermally activated order-disorder transition with a phase transition from orthorhombic to tetragonal. This high-temperature tetragonal phase (space group: *P*4/*mmm*) is observed up to 900 °C in air.

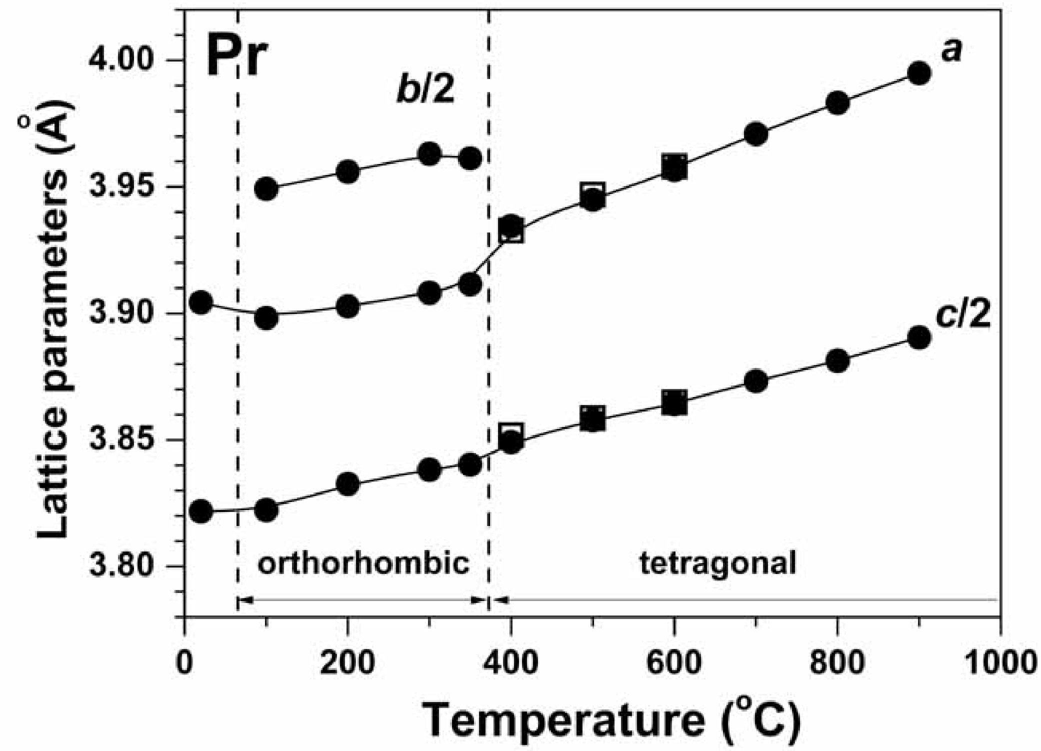

Figure 4.4 Variations of the lattice parameters of $PrBaCo_2O_{5+\delta}$ with temperature. The data were collected during heating (closed symbol) and cooling (open symbol) in air.

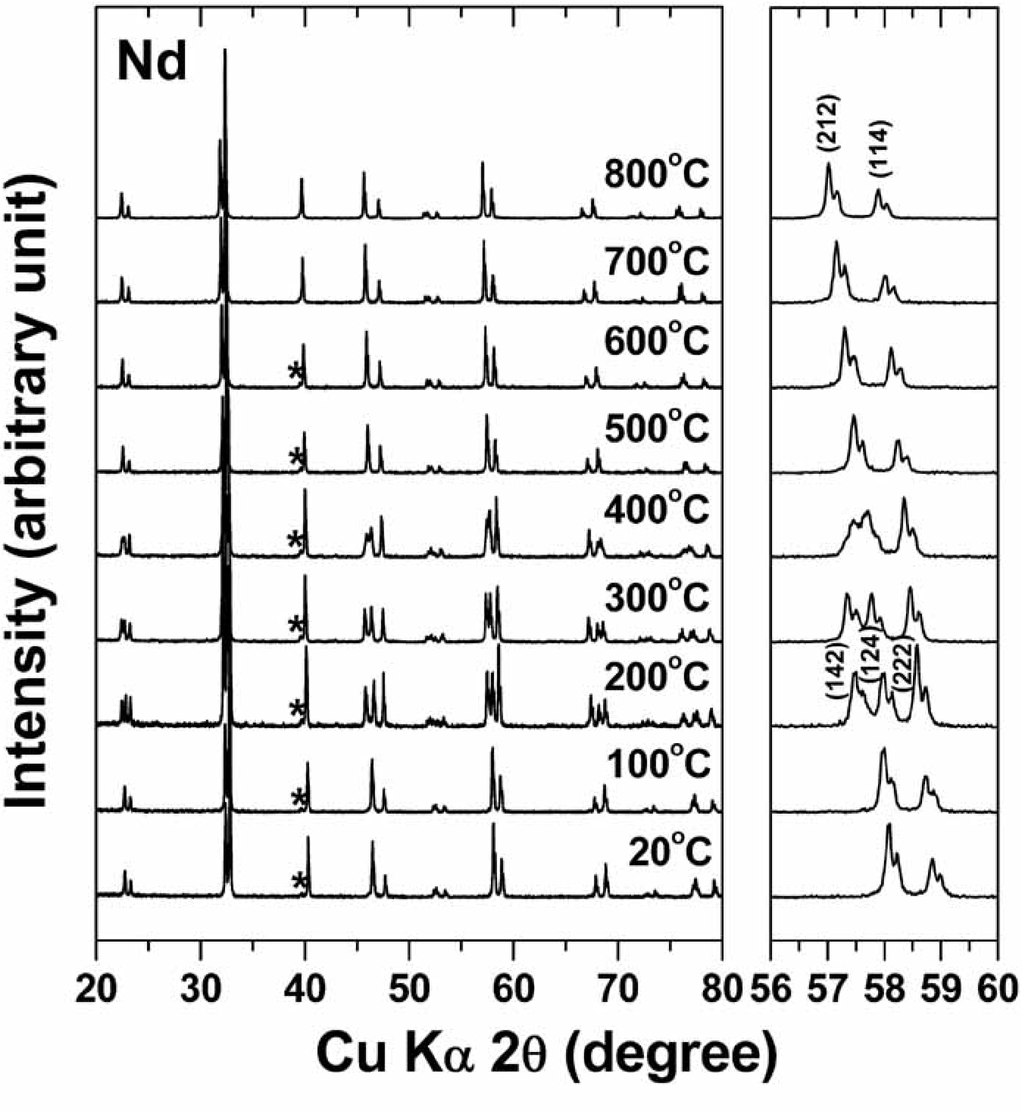

Figure 4.5 High-temperature XRD patterns of $NdBaCo_2O_{5+\delta}$ recorded with increasing temperature in air. An expanded view in the range of 56 ° ≤ 2θ ≤ 60 ° is displayed in the right panel. Reflections marked with * belong to Pt from the sample stage.

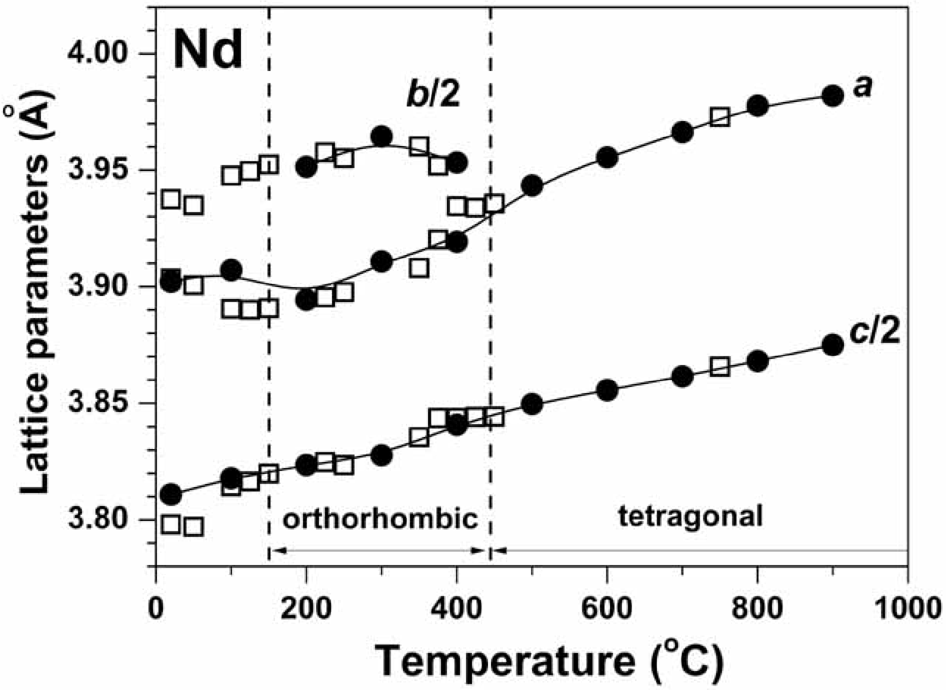

Figure 4.6 Variations of the lattice parameters of $NdBaCo_2O_{5+\delta}$ with temperature. The data were collected during heating (closed symbol) and cooling (open symbol) in air.

Figures 4.4 and 4.6 show the variation of the lattice parameters with temperature, respectively, for the Ln = Pr and Nd samples on heating and cooling in air. The oxygen loss on heating results in a reduction of the cobalt ions in $LnBaCo_2O_{5+\delta}$ (Figure 4.1) and a consequent increase in the lattice parameters. Especially, the high temperature phase transitions accompanying the M-I transitions and oxygen vacancy order-disorder transition lead to sudden variations in the lattice parameters *a* and *b*. Figure 4.6 shows that the oxygen vacancy order-disorder transition in the Ln = Nd sample is reversible at $T \sim 450\ ^{o}C$ on heating/cooling. However, the XRD pattern of the Nd sample recorded at room temperature after the cooling process showed well-separated peaks corresponding to an orthorhombic distortion with a clear deviation between the *a* and *b* parameters. Although this may appear inconsistent with the clear tetragonal structure observed with the starting material (Figure 4.5), it can be understood by considering the following. In our high temperature XRD experiments, the cooling rate was not controlled and the Nd sample was cooled rapidly to a lower temperature. As a result, the Ln = Nd sample after the high temperature XRD experiment had a lower oxygen content value after cooling to 20 ^{o}C due to the insufficient oxygen uptake during cooling compared to the starting sample ($5 + \delta = 5.85$). For example, the XRD pattern of the Ln = Nd sample recorded after the TGA measurement with a slow heating/cooling rate of 2 ^{o}C/min in air shows the same tetragonal phase as the $NdBaCo_2O_{5.85}$.

Figure 4.7 shows the high-temperature XRD patterns of the Ln = Sm sample on heating in air. With an oxygen content of 5.69, the Ln = Sm sample has the orthorhombic structure (space group: *Pmmm*) at 20 ^{o}C. At $100\ ^{o}C \leq T \leq 200\ ^{o}C$, the splitting between the (142) and (124) peaks increases (Figure 4.7) with increasing gap between *a* and *b*/2 in Figure 4.8. This increase in orthorhombicity is accompanied by the M-I transition as observed in Figure 4.2. The Ln = Sm sample also shows a phase transition from orthorhombic to tetragonal at $T \sim 400\ ^{o}C$.

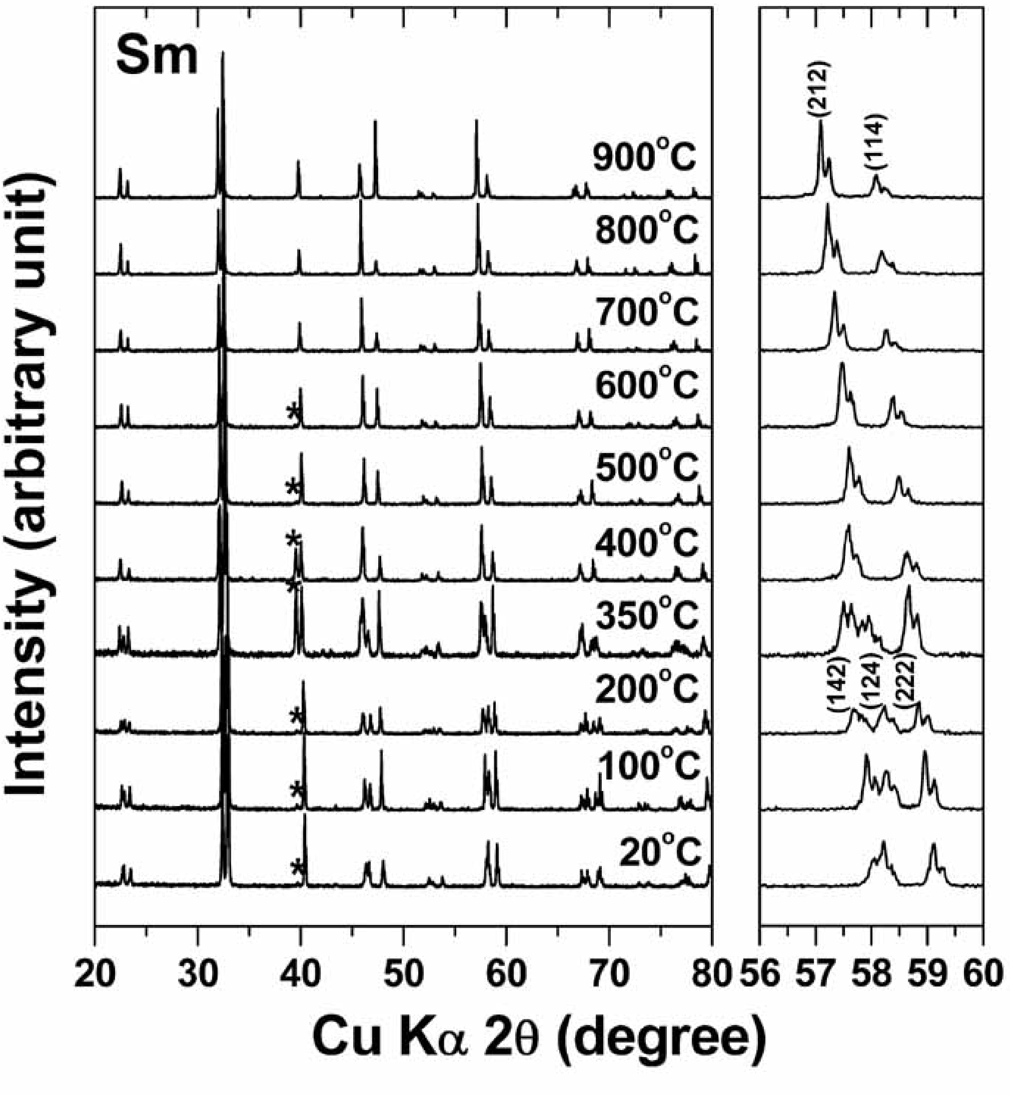

Figure 4.7 High-temperature XRD patterns of $SmBaCo_2O_{5+\delta}$ recorded with increasing temperature in air. An expanded view in the range of $56\,^{o} \leq 2\theta \leq 60\,^{o}$ is displayed in the right panel. Reflections marked with * belong to Pt from the sample stage.

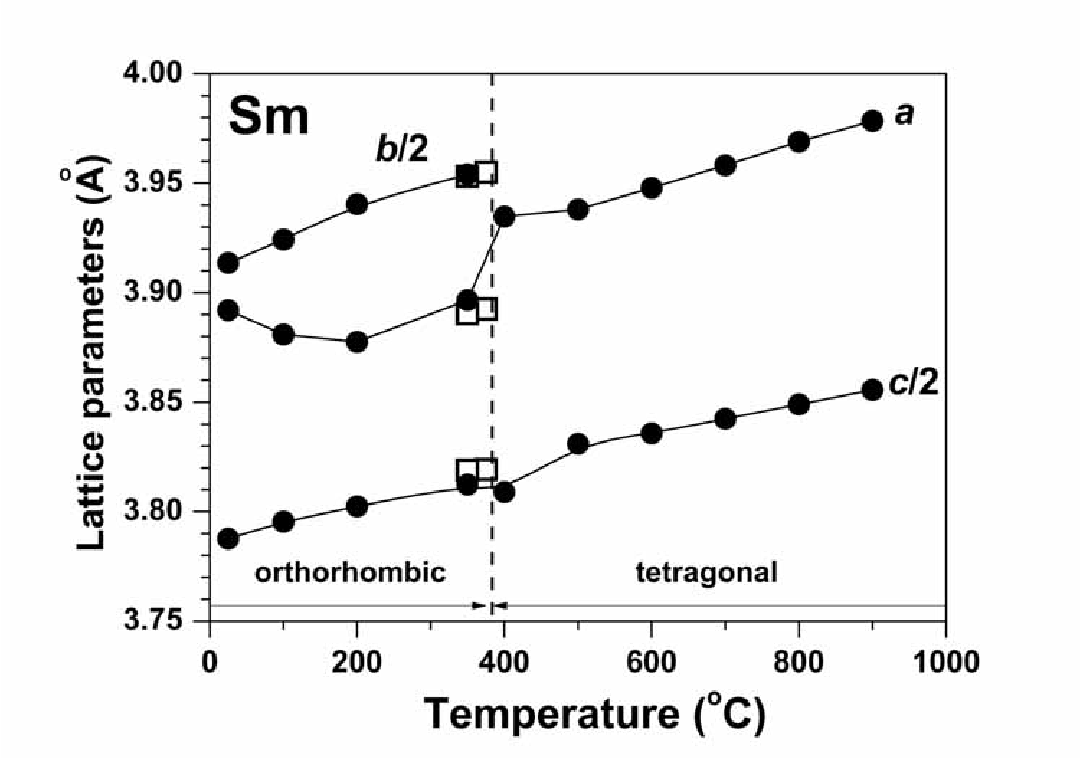

Figure 4.8 Variations of the lattice parameters of $SmBaCo_2O_{5+\delta}$ with temperature. The data were collected during heating (closed symbol) and cooling (open symbol) in air.

To assess the structural stability of the $LnBaCo_2O_{5+\delta}$ (Ln = La, Pr, Nd, and Sm) layered perovskites under N_2, we have refined the crystal structure of the samples obtained after the TGA measurements in N_2. Table 4.1 gives the room temperature oxygen content (5 + δ) values obtained by iodometric titration and the crystallographic data of these samples. After the TGA experiment in N_2, the Ln = La sample has an oxygen content (5 + δ) of 5.46 and maintains the original cubic structure with the space group *Pm*-3*m* as evidenced by a good agreement between the observed and calculated profiles in Figure 4.9. The Ln = Pr, Nd, and Sm samples, on the other hand, have oxygen contents of, respectively, 5.36, 5.30, 5.18 with a tetragonal structure (space group: *P*4/*mmm*) due to the loss of oxygen vacancy ordering. However, the Ln = Nd sample shows additional reflections (*e.g.*, a shoulder at $2\theta \approx 46.5\ ^{o}$) in the XRD pattern corresponding to a secondary phase. A similar secondary phase has also been observed in the $NdBaCo_2O_{5.38}$ sample and it has been refined to be $NdBaCo_2O_{5.5}$.[106] Therefore, the XRD pattern of the Ln = Nd sample was refined based on $NdBaCo_2O_{5.30}$ (space group: *P*4/*mmm*) and $NdBaCo_2O_{5.50}$ (space group: *Pmmm*) phases, and their Bragg peak positions are marked individually in Figure 4.9. The amount of the $NdBaCo_2O_{5.50}$ secondary phase was calculated to be 1.2 %. All the XRD patterns in Figure 4.2 indicate that the $LnBaCo_2O_{5+\delta}$ samples are stable under N_2 atmosphere up to 900 ^{o}C.

4.3.3 Oxygen Permeation Properties

Figure 4.10 compares the variations of the oxygen permeation flux (jO_2) through the $LnBaCo_2O_{5+\delta}$ (Ln = La, Nd, and Sm) ceramic membranes as a function of (pO_2'/pO_2''). All the three membranes had the same thickness (L) of 1.1 mm. The experiments were carried out by adjusting the helium flow rate to vary the pO_2'' on one side of the sample (inside the ceramic tube) while the other side was exposed to air (pO_2' = 0.209 atm). All the three membranes show an increase in jO_2 with temperature due to the increasing amount of oxygen vacancies (Figure 4.1) and

Table 4.1 Room temperature oxygen contents and crystallographic data[a] after the TGA measurements in N_2 atmosphere of $LnBaCo_2O_{5+\delta}$ (Ln = La, Pr, Nd, Sm).

Ln	La	Pr	Nd[b]	Sm
Oxygen contents $(5 + \delta)$	5.46	5.36	5.30	5.18
Space group	*Pm*-3*m*	*P*4/*mmm*	*P*4/*mmm*	*P*4/*mmm*
a	3.940	3.946	3.936	3.928
b	-	-	-	-
c	-	7.610 (1)	7.581 (1)	7.540
Co(z)	-	0.248 (1)	0.254 (2)	0.255 (1)
O2(z)	-	0.294 (1)	0.296 (2)	0.306 (1)
R_p	8.03	8.01	10.2	9.53
R_{wp}	10.9	10.5	13.3	12.3
χ^2	1.78	1.52	3.29	2.55

[a] For the cubic structure (*Pm*-3*m*), the atomic positions are (Ln, Ba) (0,0,0), Co (1/2,1/2,1/2), O (0,1/2,1/2). For the tetragonal structure (*P*4/*mmm*), the atomic positions are Ln (0,0,1/2), Ba (0,0,0), Co (1/2,1/2,z), O1 (1/2,1/2,0), O2 (1/2,0,z), O3 (1/2,1/2,1/2).

[b] The Ln = Nd sample has 1.2 % of $NdBaCo_2O_{5.50}$ as a secondary phase.

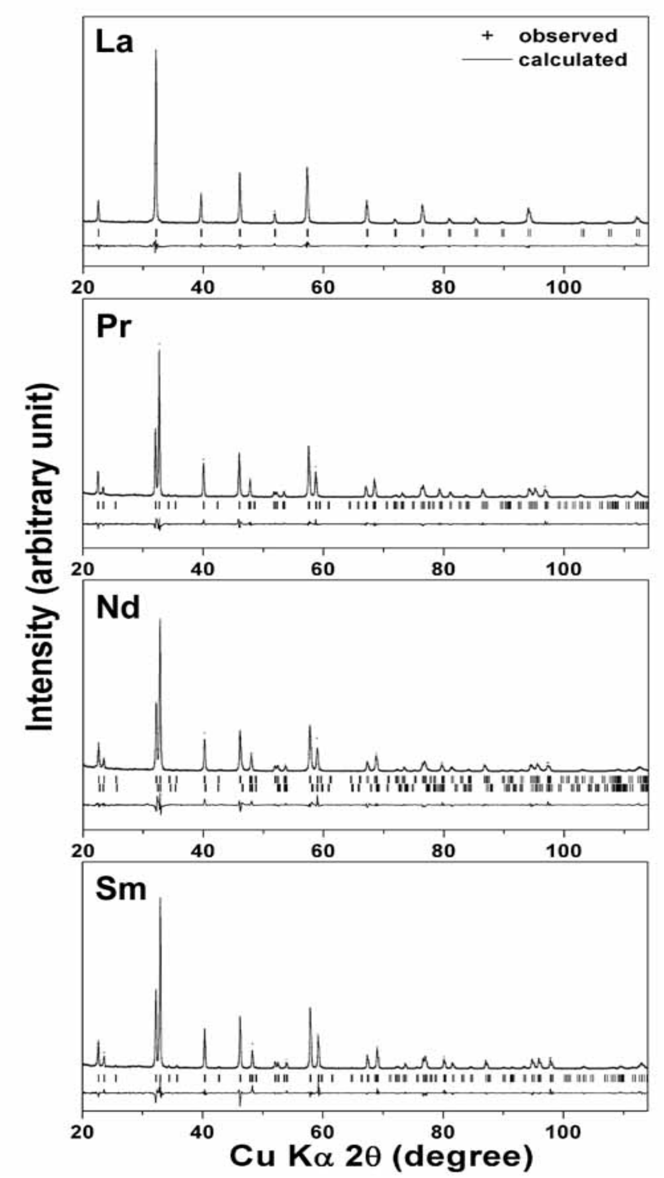

Figure 4.9 Room-temperature XRD patterns, calculated profiles, peak positions, and the difference between the observed and calculated profiles for the $LnBaCo_2O_{5+\delta}$ (Ln = La, Pr, Nd, and Sm) samples after the TGA experiments in N_2 atmosphere. For the Ln = Nd sample, the upper peak positions belong to $NdBaCo_2O_{5.30}$ (space group: *P*4/*mmm*) while the lower peak positions belong to $NdBaCo_2O_{5.50}$ (space group: *Pmmm*).

increasing oxide ion conductivity as has been observed with other perovskite systems.[107] At a given temperature, jO_2 decreases from Ln = La to Nd to Sm (Figure 4.10) although the amount of oxygen vacancies increases (Figure 4.1). This could be understood by considering their high temperature crystal structures. The oxygen diffusion pathway is three-dimensional in the Ln = La sample having a disordered perovskite structure due to the smaller size difference between La^{3+} and Ba^{2+}. In contrast, the oxygen diffusion is expected to be two-dimensional in both the Ln = Nd and Sm samples having a tetragonal structure (space group: *P*4/*mmm*) at $T > 500$ °C (Figures 4.5–4.8), in which the oxygen vacancies are localized in the LnO plane due to a larger size difference between Ln^{3+} and Ba^{2+}. Additionally, structures free of lattice distortions and with low or no strain have been considered to exhibit high oxide-ion conductivity in the perovskite system.[108] Thus, the Ln = La sample with the cubic perovskite structure and three-dimensional oxygen diffusion exhibits higher oxide ion conductivity or jO_2 compared to the Ln = Nd and Sm samples with tetragonal structures and two-dimensional oxygen diffusion. Between the Ln = Nd and Sm samples, a larger strain in the latter due to the larger size difference between Sm^{3+} and Ba^{2+} leads to lower jO_2.

Figure 4.11 compares the temperature dependence of $\log(jO_2)$ for the Ln = La, Nd, and Sm membranes having the same thickness (L) of 1.1 mm at $\log(pO_2'/pO_2'') =$ 1.0 and 1.5. The data for the Ln = Nd specimen with $L = 3.3$ mm are also plotted in Figure 4.11 for a comparison. Although slight deviations in the slope occur due to small variations in the sample thickness and density, we can conclude that all the samples have similar activation energy for oxygen permeation in the temperature range of 700 °C – 900 °C.

With an aim to understand the oxygen permeation mechanism, the oxygen flux through the Ln = Nd membranes with three different thicknesses (*L*) of 1.1, 1.8. 3.3 mm were measured (Figure 4.12). When the oxygen permeation through a mixed ionic-electronic conductor is limited by surface exchange rate, jO_2 does not vary with the thickness of the membrane. On the other hand, if the oxygen permeation is bulk limited, jO_2 across the membrane varies with the thickness of the membrane in accordance with the Wagner equation,[109]

$$jO_2 = -\frac{RT}{4^2 F^2 L} \int_{\ln pO_2'}^{\ln pO_2''} \frac{\sigma_{el}\sigma_{ion}}{\sigma_{el} + \sigma_{ion}} d \ln pO_2 \tag{4.1}$$

where *R* is the gas constant, *F* is the Faraday constant, *T* is the temperature, *L* is the thickness of the membrane, and σ_{el} and σ_{ion} are, respectively, the electronic and ionic conductivities. Figure 4.12(a) shows that the jO_2 decreases with increasing *L* at 900 and 870 °C. In addition, the variations of jO_2 with the reciprocal of membrane thickness (1/*L*) exhibit a linear relationship and good extrapolation to the origin in Figure 4.12(b). These results suggest that the rate of oxygen permeation in the $LnBaCo_2O_{5+\delta}$ samples is governed by bulk diffusion rather than surface exchange for $L \geq 1.1$ mm. Based on the observed high total conductivity $\sigma_{total} > 400$ S/cm for the $LnBaCo_2O_{5+\delta}$ (Ln = La, Nd, and Sm) samples at $T \leq 900$ °C (Figure 4.2) and the

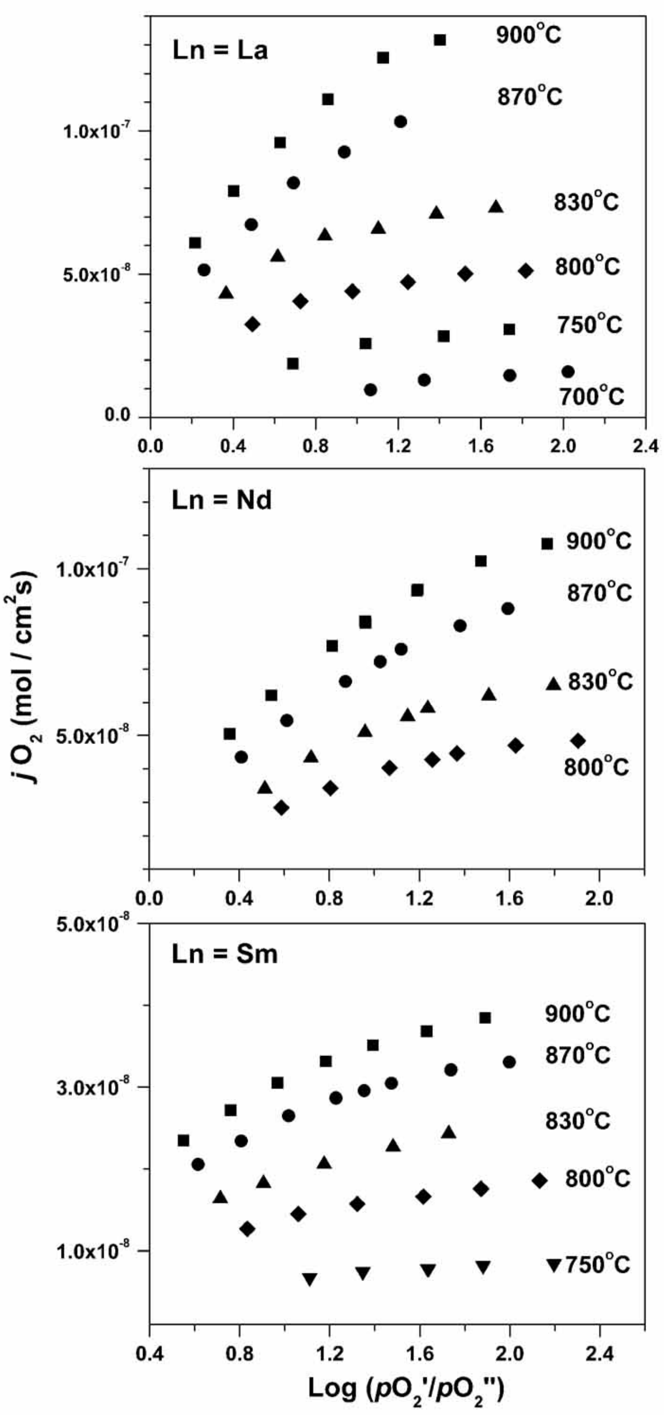

Figure 4.10 Variations of the oxygen permeation flux (jO_2) of $LnBaCo_2O_{5+\delta}$ (Ln = La, Nd, and Sm) with $\log(pO_2'/pO_2'')$ at different temperatures. The measurements were conducted with 1.1 mm thick samples.

recognition that perovskite oxides generally exhibit σ_{el} » σ_{ion}, Eq. 4.1 can be further simplified as

$$jO_2 = \frac{RT}{4^2 F^2 L}\bar{\sigma}_i \ln(pO_2' / pO_2'') \tag{4.2}$$

Using Eq. 4.2 and the experimental data in Figure 4.10, one can obtain the average ionic conductivity values for the $LnBaCo_2O_{5+\delta}$ (Ln = La, Nd, and Sm) samples. For example, the σ_{ion} values are calculated to be 0.056, 0.040, and 0.011 S/cm, respectively, for Ln = La, Nd, and Sm at 900 °C. The σ_{ion} values decrease to 0.046, 0.037, and 0.010 S/cm, respectively, for Ln = La, Nd, and Sm on lowering the temperature to 870 °C.

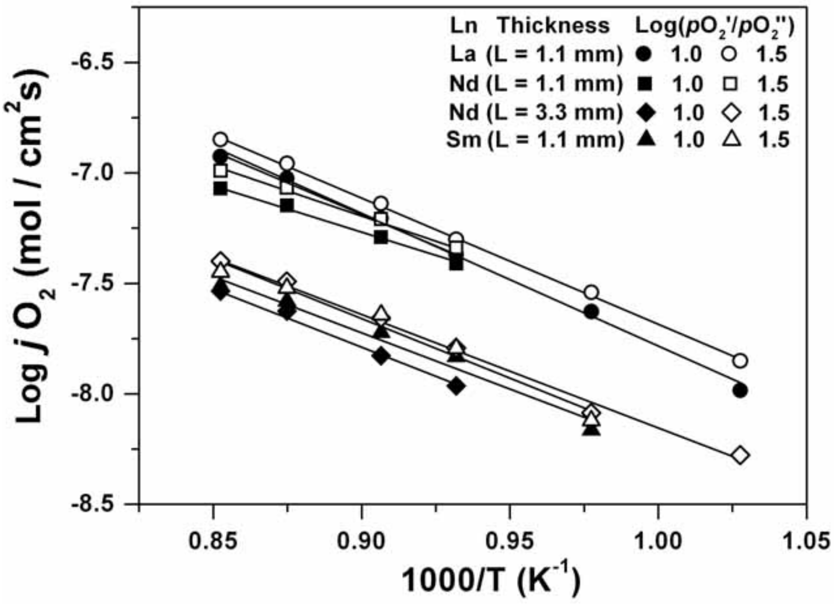

Figure 4.11 Arrhenius plots of the variations of the oxygen permeation flux (jO_2) of $LnBaCo_2O_{5+\delta}$ (Ln = La, Nd, and Sm) with inverse temperature at $\log(pO_2'/pO_2'')$ = 1.0 and 1.5.

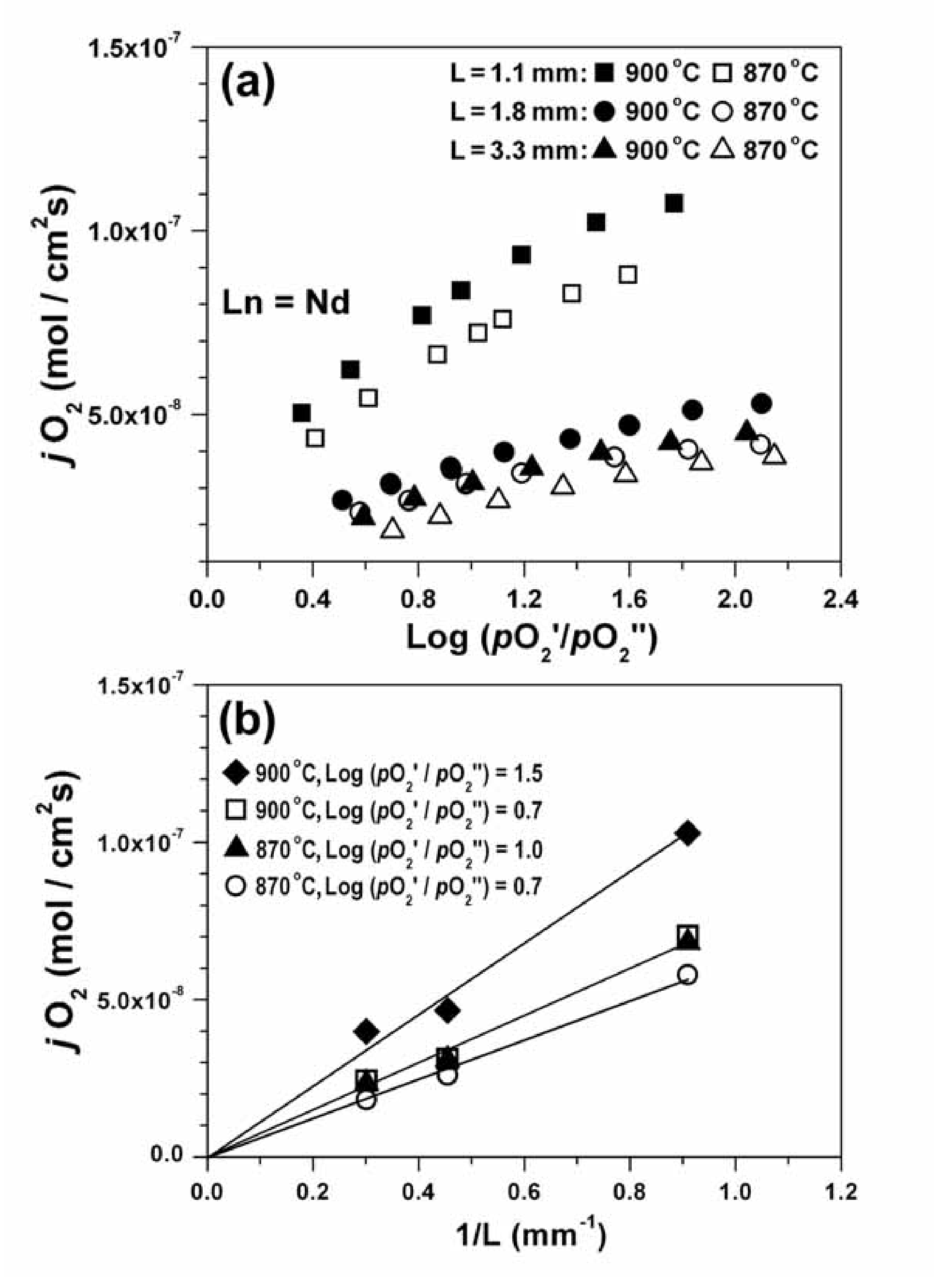

Figure 4.12 (a) Variations of the oxygen permeation flux (jO_2) of NdBaCo$_2$O$_{5+\delta}$ with log(pO_2'/pO_2'') for different sample thicknesses (L) and (b) variations of the oxygen permeation flux (jO_2) of NdBaCo$_2$O$_{5+\delta}$ with inverse sample thickness (1/L).

4.4 CONCLUSIONS

The high temperature structures and oxygen permeation properties of $LnBaCo_2O_{5+\delta}$ oxides have been investigated. The $LnBaCo_2O_{5+\delta}$ (Ln = Pr, Nd, and Sm) oxides exhibit metal-insulator transitions at $T < 200$ °C and oxygen vacancy order-disorder transitions accompanied by a transition from orthorhombic to tetragonal structure at $T > 350$ °C. At a given temperature, the oxygen permeation flux jO_2 through the $LnBaCo_2O_{5+\delta}$ membranes decreases from La to Nd to Sm due to a lowering of the crystal symmetry and lattice strain. A linear dependence of jO_2 with the reciprocal of membrane thickness ($1/L$) and its extrapolation to the origin in the Ln = Nd sample reveal that the oxygen transport mechanism is bulk diffusion limited. The oxide ion conductivity values calculated using the Wagner's equation decrease with decreasing size of the Ln^{3+} ions from Ln = La to Nd to Sm. Therefore, the decreasing single cell SOFC performance observed from Ln = La to Gd in Chapter 3 could be partly understood to be due to the decreasing oxygen diffusion rate within the $LnBaCo_2O_{5+\delta}$ cathode.

CHAPTER 5

Characterization of $GdBa_{1-x}Sr_xCo_2O_{5+\delta}$ ($0 \le x \le 1.0$) Double Perovskites as Cathodes for Intermediate Temperature SOFC

5.1 INTRODUCTION

Chapters 2 and 3 presented a systematic investigation of the relationship between the crystal structure and thermal and electrical properties of the layered $LnBaCo_2O_{5+\delta}$ perovskite system. The $LnBaCo_2O_{5+\delta}$ (Ln = Pr, Nd, and Sm) oxides exhibit a metal-insulator transition at $T < 200$ °C as evidenced by total conductivity measurements and high-temperature X-ray diffraction (XRD) data and an oxygen vacancy order-disorder transition at $T > 350$ °C in air as evidenced by an orthorhombic to tetragonal transition. The TEC decreases with decreasing size of the Ln^{3+} ions from Ln = La to Y due to the decreasing ionicity of the Ln-O bond. At a given temperature, the oxygen permeation flux decreases from Ln = La to Nd to Sm due to the changes in crystal symmetry and lattice strain. The oxygen permeation mechanism in the Ln = Nd is found to be bulk diffusion limited rather than surface exchange limited for a membrane thickness $L \ge 1.1$ mm. The lower oxygen diffusion rate and electrical conductivity with decreasing size of the Ln^{3+} ions from Ln = La to Gd are partly attributed to the decrease in the single fuel cell performances.

Although the $GdBaCo_2O_{5+\delta}$ showed lower TEC compared to those obtained with the Ln = La, Nd, and Sm samples, it is chemically unstable in contact with the

LSGM and GDC electrolytes at high temperatures. With an aim to improve the catalytic activity for ORR and the chemical stability with the electrolytes, this Chapter presents an investigation of the substitution of Sr for Ba in the $GdBa_{1-x}Sr_xCo_2O_{5+\delta}$ ($0 \leq x \leq 1.0$) system. The effects of Sr substitution on the crystal chemistry, oxygen content, chemical stability in contact with the electrolyte, and catalytic activity for ORR are discussed.

5.2 EXPERIMENTAL

5.2.1 Materials Synthesis

The $GdBa_{1-x}Sr_xCo_2O_{5+\delta}$ ($0 \leq x \leq 1.0$) oxides were synthesized by conventional solid-state reaction methods. Required amounts of Gd_2O_3, $BaCO_3$, $SrCO_3$, and Co_3O_4 were thoroughly mixed with ball milling in ethanol for 24 h and calcined at 1000 ^oC for 12 h in air. The calcined powders were then ground, pressed into pellets, and sintered at 1200 ^oC for 24 h in air. The resulting products were ground and finally heated at 900 ^oC for 6 h in air, followed by slow cooling to room temperature at a rate of 1^oC/min to maximize the oxygen contents. The $La_{0.8}Sr_{0.2}Ga_{0.8}Mg_{0.2}O_{2.8}$ (LSGM) electrolyte disks, the NiO-10GDC cermet anode, and the LDC powder were synthesized as described in Chapter 2.

5.2.2 Cha racterization

The synthesized $GdBa_{1-x}Sr_xCo_2O_{5+\delta}$ sample was characterized by XRD, Rietveld refinement, iodometric titration, TGA, TMA, electrical conductivity, SEM, and single cell performance measurements as described in Chapter 2. The specimens for the reactivity tests were obtained by mixing the $GdBa_{1-x}Sr_xCo_2O_{5+\delta}$ and the electrolyte powders in a 1:1 weight ratio, followed by calcining in air at 1100 ^oC for 0.5 and 1 h, respectively, for LSGM and GDC.

5.2.3 Fabrication of Single Cells

The single cells consisting of $GdBa_{1-x}Sr_xCo_2O_{5+\delta}$ | $GdBa_{1-x}Sr_xCo_2O_{5+\delta}$ + LSGM | LSGM(500 μm thickness) | LDC|Ni + 10GDC were prepared as described in Chapter 2. The composite layer ($GdBa_{1-x}Sr_xCo_2O_{5+\delta}$: LSGM = 1 : 1 wt. ratio) and the $GdBa_{1-x}Sr_xCo_2O_{5+\delta}$ cathode were heated, respectively, at 1100 ^oC for 0.5 h and 1000 ^oC for 3 h.

5.3 RESULTS AND DISCUSSION

5.3.1 Crystal Structure and Oxygen Content Analysis

Figure 5.1 shows the XRD patterns of the $GdBa_{1-x}Sr_xCo_2O_{5+\delta}$ ($0 \leq x \leq 1.0$) samples. All the reflections of the parent $GdBaCo_2O_{5+\delta}$ sample could be indexed with an orthorhombic structure with the space group of *Pmmm*.[85,87,104] Iodometric titration indicates the room temperature oxygen content to be 5.61 (Table 5.1) in $GdBaCo_2O_{5+\delta}$. The fully Sr-substituted $GdSrCo_2O_{5+\delta}$ has been reported to have an orthorhombic structure with the space group of *Pnma*.[110,111] The XRD pattern in Figure 5.1(f) is consistent with this earlier result, and our chemical analysis indicates an oxygen content of 6.0 as seen in Table 5.1. The room temperature crystal structures of the intermediate compositions with $0.2 \leq x \leq 0.6$ in $GdBa_{1-x}Sr_xCo_2O_{5+\delta}$ could be refined on the basis of a tetragonal symmetry with the space group *P*4/*mmm*. As an example, the experimental XRD data, calculated profile, and the difference between the experimental and calculated profiles are shown in Figure 5.2 for the x = 0.4 sample. There is a good agreement between the experimental and calculated profiles, and the resulting atomic positions and the quality of refinement are given in Table 5.2. The refinement was also performed assuming that Sr is partly located at the Gd site. However, the Sr amount at the Gd site reduced to zero at the end of refinement, suggesting that Sr prefers the Ba site. This is consistent with an earlier report by Nakamura *et al.*[112] that Sr occupies the Ba-sites in the $(Ba_{1-x}Sr_x)SmFe_2O_5$ double perovskite. The x = 0.8 sample in Figure 5.1(e) consists of a mixture of tetragonal (*P*4/*mmm*) and orthorhombic (*Pnma*) phases as revealed by the inset at $2\theta \approx 48^o$. The unit cell volume given in Table 5.1 decreases with increasing Sr content due to a substitution of a smaller Sr^{2+} for Ba^{2+} and an oxidation of the larger Co^{3+} ions into the smaller Co^{4+} ions as indicated by an increase in the oxygen content value (Table 5.1).

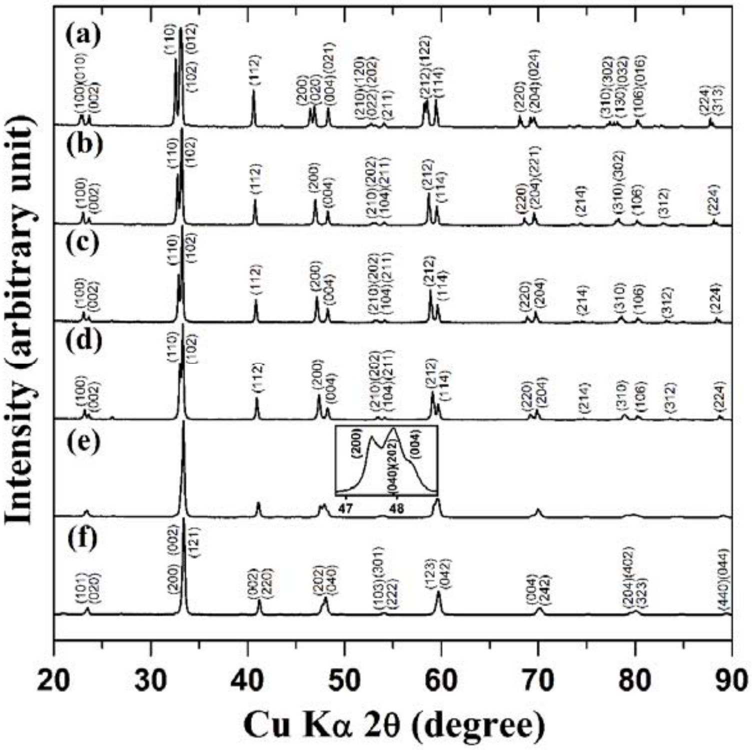

Figure 5.1 X-ray diffraction patterns of the $GdBa_{1-x}Sr_xCo_2O_{5+\delta}$ samples: (a) x = 0, (b) x = 0.2, (c) x = 0.4, (d) x = 0.6, (e) x = 0.8, and (f) x = 1.0.

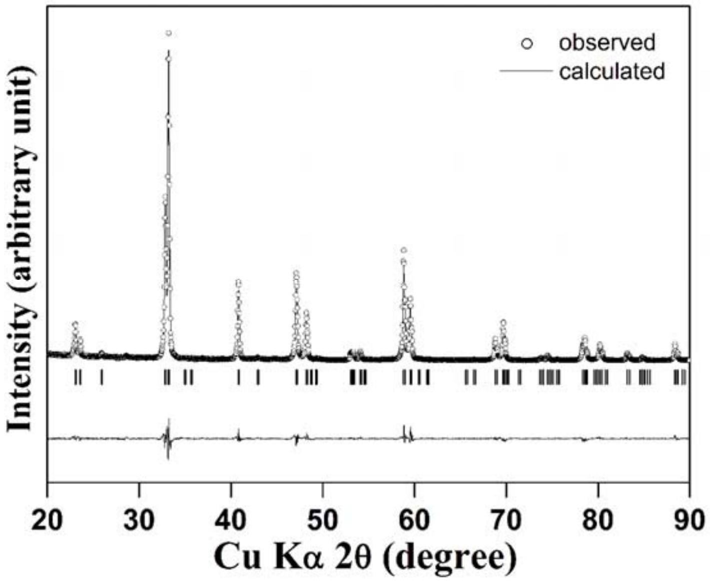

Figure 5.2 XRD pattern, calculated profile, peak position, and the difference between observed and calculated profiles for the $GdBa_{0.6}Sr_{0.4}Co_2O_{5+\delta}$ sample.

Table 5.1 Structural parameters, chemical analysis data, and TEC of the $GdBa_{1-x}Sr_xCo_2O_{5+\delta}$ oxides.

x	Space group	Z	a (Å)	b (Å)	c (Å)	V (Å^3)	Oxidation state of Co	Oxygen content (5+δ)	TEC × 10^6 ($^{o}C^{-1}$)		
									80 – 900°C	80 – 300°C	300 – 900°C
0.0	*Pmmm*	1	3.876	3.912	7.541	114.367	3.11	5.61	16.6	16.3	17.7
0.2	*P*4/*mmm*	1	3.872	3.872	7.550	113.155	3.19	5.69	18.0	15.9	18.7
0.4	*P*4/*mmm*	1	3.856	3.856	7.546	112.194	3.29	5.79	18.3	16.0	19.8
0.6	*P*4/*mmm*	1	3.840	3.840	7.549	111.304	3.33	5.83	19.5	15.7	20.9
1.0*	*Pnma*	4	5.373	7.572	5.402	219.763	3.50	6.00	18.8	15.3	19.9

* Lattice parameter and volume are based on the chemical formula $Gd_{0.5}Sr_{0.5}CoO_3$.

Table 5.2 Room temperature atomic positions in $GdBa_{1-x}Sr_xCo_2O_{5+\delta}$.

x	z_{Co}	$z_{O(2)}$	R_{wp}	χ^2
0.2	0.2566	0.2832	13.5	3.21
0.4	0.2523	0.2788	11.5	2.93
0.6	0.2520	0.2754	10.9	3.24

* Atomic positions are Gd (0,0,1/2), Ba/Sr (0,0,0), Co (1/2,1/2,z), O(1) (1/2,1/2,0), O(2) (1/2,0,z), and O(3) (1/2,1/2,1/2).

Iodometric titration data in Table 5.1 indicate that the room temperature oxygen content and the oxidation state of cobalt increase with increasing Sr content x. Although one would generally anticipate the more electropositive Ba^{2+} ions to enhance the stabilization of the higher valent Co^{4+} ions, the ordering between Ba^{2+} and Gd^{3+} ions in alternate layers due to a larger size difference between them and the tendency of the smaller Gd^{3+} ions to adopt a coordination number less than 12 result in a lower oxygen content value for $GdBaCo_2O_{5+\delta}$. On the other hand, a smaller size difference between the Sr^{2+} and Gd^{3+} ions and a consequent perturbation of the ordering between the two layers (Ba and Gd layers) result in a tendency to increase the coordination number and a consequent increase in oxygen content values. Similar increases in oxygen content values on decreasing the difference in the ionic radii values between Ln^{3+} and Ba^{2+} in $LnBaCo_2O_{5+\delta}$ have also been observed before, with a structural change from orthorhombic (Ln = Sm, Eu, Gd, and Tb) to tetragonal (Ln = Pr and Nd).[84,85,88,105,106,113,114] Figure 5.3 shows the relationship between the room temperature oxygen content ($5 + \delta$) and the difference in ionic radii between $(Ba_{1-x}Sr_x)^{2+}$ and Ln^{3+} ($r_A{}^{2+} - r_{Ln}{}^{3+}$) for the $Gd(Ba_{1-x}Sr_x)Co_2O_{5+\delta}$ and $LnBaCo_2O_{5+\delta}$ (Ln = La, Nd, Sm, Gd, and Y) samples synthesized in air; for a comparison, the ionic radii values used in Figure 5.3 are all for 12 fold coordination and they are listed in Table 5.3.[112,115-117] For smaller lanthanide ions like Gd^{3+} and Y^{3+} for which the12 fold coordinated radii are not available, the ionic radii for 12 fold coordination were obtained by extrapolating their 8 fold coordinated ionic radii values. Both the series of samples exhibit a linear relationship between oxygen non-stoichiometry and the ionic size difference (r_A^{2+} - r_{Ln}^{3+}). The larger the size difference between $(Ba_{1-x}Sr_x)^{2+}$ and Ln^{3+}, the greater is the tendency of $(Ba_{1-x}Sr_x)^{2+}$ and Ln^{3+} to order on the alternate planes along the *c* axis and the lower is the oxygen content as Ln^{3+} will tend to have less than 12 fold coordination. Thus, the trend in Figure 5.3 may be useful to predict the oxygen content based on the size difference between the A^{2+} and Ln^{3+} ions in $ALnCo_2O_{5+\delta}$ perovskites.

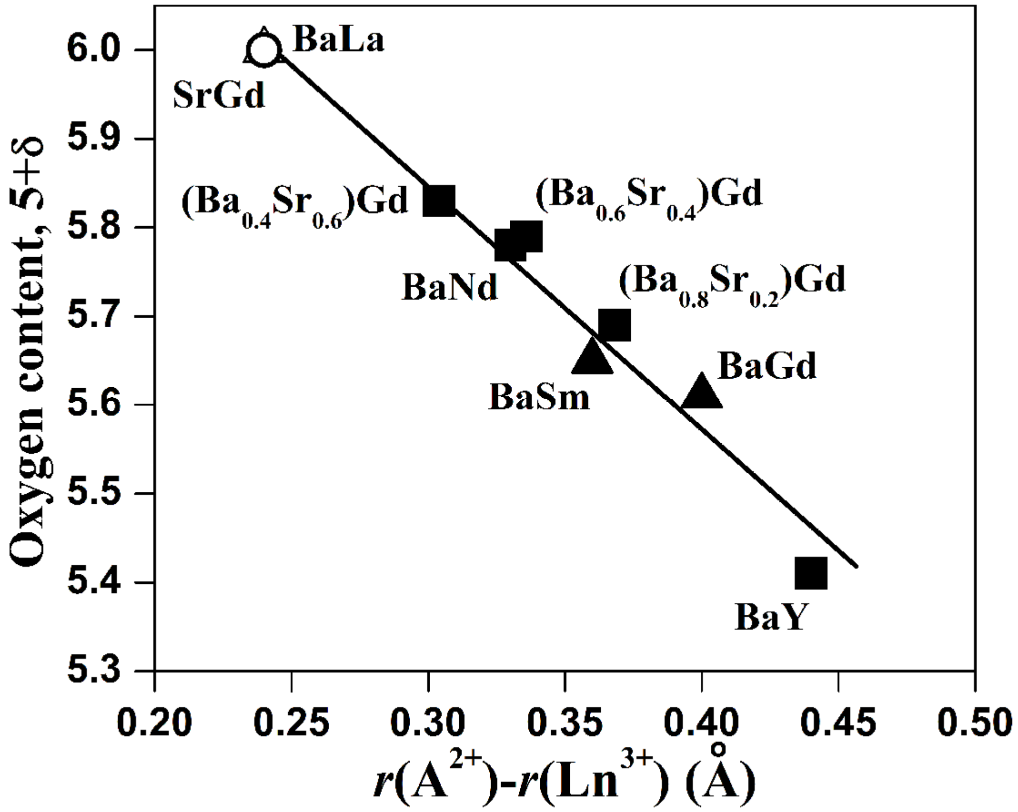

Figure 5.3 Variations of the room-temperature oxygen content (5+δ) values with the difference in ionic radii between $(Ba_{1-x}Sr_x)^{2+}$ and Ln^{3+} (r_A^{2+} - r_A^{3+}) in the $Gd(Ba_{1-x}Sr_x)Co_2O_{5+\delta}$ and $LnBaCo_2O_{5+\delta}$ (Ln = La, Nd, Sm, Gd, and Y) samples synthesized in

air. The different symbols refer to different crystal structures: ○: cubic (*Pm*-3*m*), ■: tetragonal (*P*4/*mmm*), ▲: orthorhombic (*Pmmm*), △: orthorhombic (*Pnma*).

Table 5.3 Comparison of the ionic radii values of the lanthanide and alkaline earth ions for 12-coordination.[115]

Ion	Ionic radius (Å)
Ba^{2+}	1.60
Sr^{2+}	1.44
La^{3+}	1.36
Nd^{3+}	1.27
Sm^{3+}	1.24
Gd^{3+}	1.21[a]
Y^{3+}	1.17[a]

[a] The values were obtained by extrapolating their 8-coordinated values.

5.3.2 Thermal and Electrical Properties

Figure 5.4 shows the variations of the oxygen content and oxidation state of cobalt with temperature in air for the $GdBa_{1-x}Sr_xCo_2O_{5+\delta}$ ($0 \leq x \leq 1.0$) samples. These curves were derived using the initial room temperature oxygen content values determined by the iodometric titration and the TGA data collected in air. The $GdBa_{1-x}Sr_xCo_2O_{5+\delta}$ samples lose oxygen on heating with a reduction of Co^{4+} to Co^{3+} as shown below using the Kroger-Vink notation[118]:

$$2\,\mathrm{Co}_{\mathrm{Co}}^{\bullet} + \mathrm{O}_{\mathrm{O}}^{\mathrm{X}} \leftrightarrow 2\,\mathrm{Co}_{\mathrm{Co}}^{\mathrm{X}} + \mathrm{V}_{\mathrm{O}}^{\bullet\bullet} + \tfrac{1}{2}\,\mathrm{O}_2 \tag{5.1}$$

In the case of $0 \leq x \leq 0.4$ samples, the Co^{3+} ions in $GdBa_{1-x}Sr_xCo_2O_{5+\delta}$ are further reduced to Co^{2+} on heating to 900 °C as shown below:

$$2\,Co_{Co}^{X} + O_{O}^{X} \leftrightarrow 2\,Co_{Co}^{/} + V_{O}^{\bullet\bullet} + \tfrac{1}{2}\,O_2 \qquad (5.2)$$

All the samples lose 0.35 – 0.4 oxygen atoms per formula unit on heating to 900 °C. However, at a given temperature, the oxidation state of cobalt increases with Sr content due to the higher initial, room temperature oxygen content values (Table 5.1).

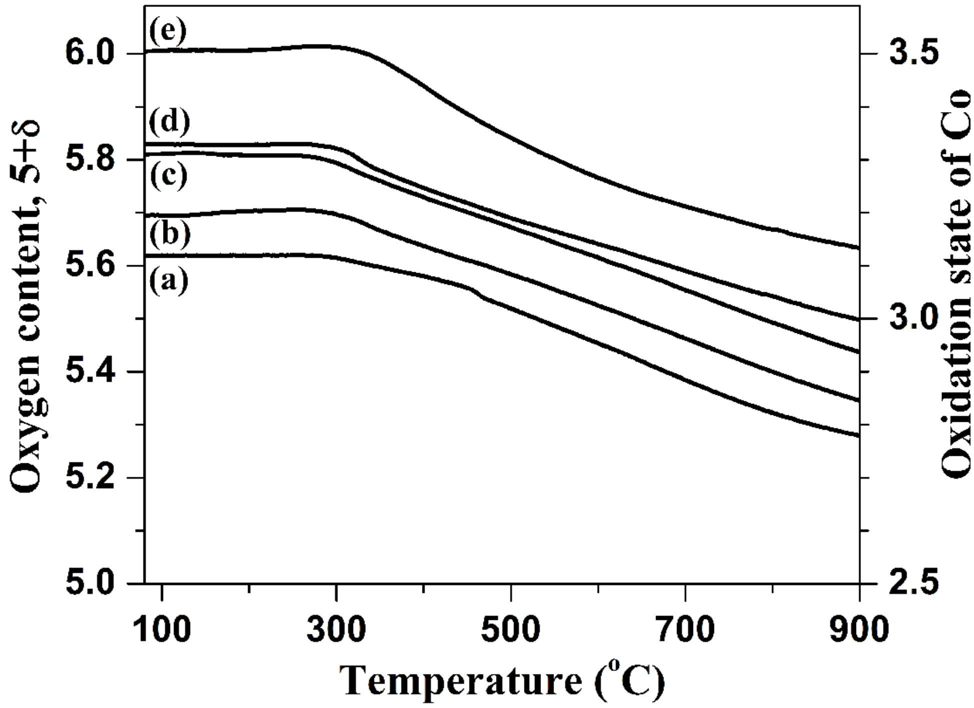

Figure 5.4 Variations of the oxygen content and the oxidation state of cobalt in the $GdBa_{1-x}Sr_xCo_2O_{5+\delta}$ with temperature in air: (a) x = 0, (b) x = 0.2, (c) x = 0.4, (d) x = 0.6, and (e) x = 1.0.

Figure 5.5 shows thermal expansion curves of the $GdBa_{1-x}Sr_xCo_2O_{5+\delta}$ samples measured in air. The $GdBa_{1-x}Sr_xCo_2O_{5+\delta}$ samples show a linear expansion in the low temperature region and an increase in slope at higher temperatures (> 300 ^oC). The increasing slope is due to the loss of oxygen from the lattice at high temperatures and the consequent reduction of smaller Co^{4+} to larger Co^{3+} or Co^{2+} ions as revealed by the TGA data (Figure 5.4). The thermal expansion curves were found to be reversible in the subsequent heating and cooling cycles. The thermal cycling was repeated three times in the temperature range of 80 – 900 ^oC, and the average TEC values of the three cycles are given in Table 5.1. Considering the oxygen loss from the lattice at T > 300 ^oC (Figure 5.4), the TEC values were calculated for two different temperature regions: 80 – 300 ^oC and 300 – 900 ^oC. In the low temperature region (80 – 300 ^oC) where oxygen loss is negligible, TEC decreases with increasing Sr content, which could be due to the replacement of more ionic Ba-O bonds with the less ionic Sr-O bonds. In contrast, in the high temperature region (300 – 900 ^oC) where oxygen loss occurs, TEC increases with increasing Sr content, which can be understood by considering the spin state transition associated with the Co^{3+} ions. For example, the high TEC of the cobalt-containing perovskites (*e.g.* $LnCoO_3$) has been considered to be due to the low spin $Co^{III}(t_{2g}^{6}e_{g}^{0})$ to intermediate spin $Co^{iii}(t_{2g}^{5}e_{g}^{1})$ or high spin $Co^{3+}(t_{2g}^{4}e_{g}^{2})$ transitions.[41,83,119] Although the oxidation state of cobalt below 300 ^oC is around 3.1+ for the x = 0 sample, the oxidation state begins to fall below 3+ for $T >$ 500 ^oC and reaches 2.77+ at 900 ^oC as seen in Figure 5.4, and Co^{2+} remains in the high spin state. On the other hand, the concentration of Co^{3+} ions in the temperature range 300 – 900 ^{o}C increases with increasing Sr content, and the x = 0.4 and 0.6 samples have the maximum amount of Co^{3+} ions, which undergo spin state transition. As a result, TEC increases on increasing the Sr content from 0 to 0.6 (Table 5.1). However, the x = 1.0 sample has a lower concentration of Co^{3+} ions than the x = 0.6 sample in the temperature range of 300 – 900 ^{o}C, resulting in a decrease in TEC for the x = 1.0 sample. The Co^{4+} ions are known to exist in the low spin Co^{IV} ($t_{2g}^{5}\ e_{g}^{0}$) state without undergoing spin state transitions.

Figure 5.6 shows the variations of the electrical conductivity with temperature for the $GdBa_{1-x}Sr_xCo_2O_{5+\delta}$ samples. All the $GdBa_{1-x}Sr_xCo_2O_{5+\delta}$ samples show a decrease in electrical conductivity with increasing temperature for $T > 300$ ^{o}C due to an increasing concentration of oxygen vacancies. However, there is a sudden drop in conductivity at low temperatures ($T < 200$ ^{o}C). The parent $GdBaCo_2O_{5+\delta}$ has been reported to have a metal-insulator (M-I) transition below 100 ^{o}C (see Figure 5.6 (a)) due to an ordering of the low spin $Co^{III}(t_{2g}^{6}e_{g}^{0})$ and intermediate spin $Co^{iii}(t_{2g}^{5}e_{g}^{1})$.[84,87] Thus, the drop in conductivity below 200 ^{o}C for the $0 \leq x \leq 1.0$ samples is due to M-I transition. However, the transition becomes less pronounced with increasing Sr content due to the increasing oxidation state of cobalt (Table 5.1 and Figure 5.4) and the consequent decrease in oxide ion vacancy concentration and increase in the Co-O covalency and bandwidth.[91-93] For the same reason, at a given temperature, the electrical conductivity increases with increasing Sr content due to the increasing oxygen content. In addition, the Sr substitution for $0.2 \leq x \leq 0.6$ relieves the compressive stress in the O-Co-O bonding due to a decreasing size of the cobalt ions (*i.e.* increasing Co^{4+} content) and increases the O-Co-O bond angle towards the ideal value of 180° as evidenced by the structural change from orthorhombic to tetragonal. The straightening of the O-Co-O bonds increases the overlap between the Co:3*d* and O:2*p* orbitals and consequently the electrical conductivity.[91,92,120] All the $GdBa_{1-x}Sr_xCo_2O_{5+\delta}$ samples show conductivity > 300 S/cm up to 800 °C, which is adequate for the samples to be employed as cathodes in SOFC.

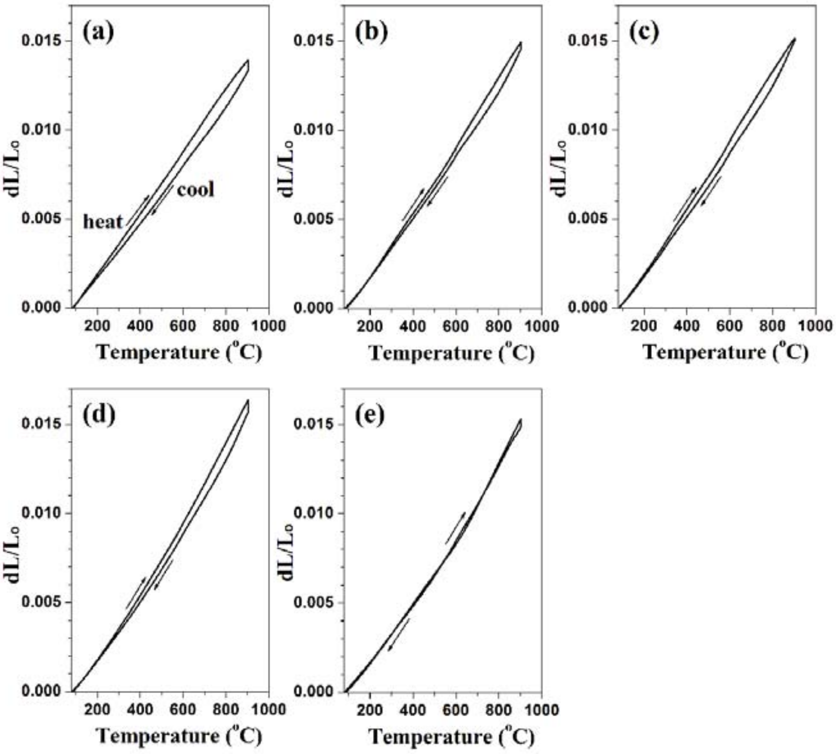

Figure 5.5 Thermal expansion (dL/L_o) curves of the $GdBa_{1-x}Sr_xCo_2O_{5+\delta}$ samples in the temperature range of 80 – 900 °C in air: (a) x = 0, (b) x = 0.2, (c) x = 0.4, (d) x = 0.6, and (e) x = 1.0.

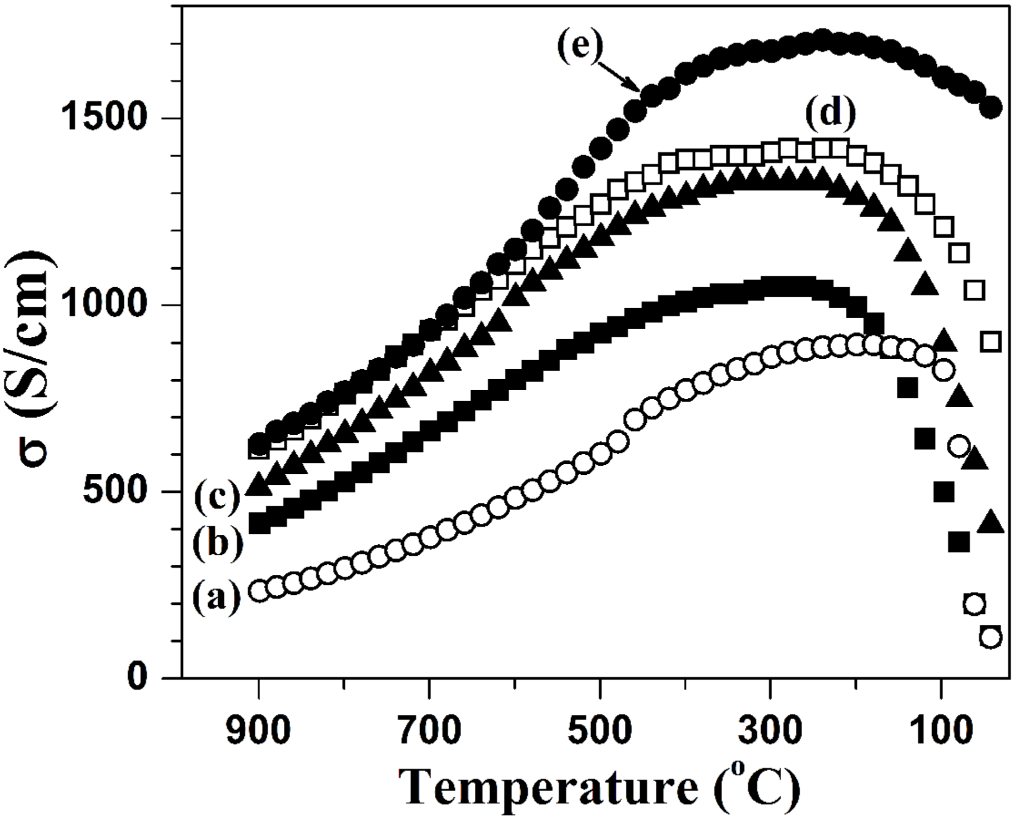

Figure 5.6 Temperature dependence of the electrical conductivity of the $GdBa_{1-x}Sr_xCo_2O_{5+\delta}$ samples in air: (a) x = 0, (b) x = 0.2, (c) x = 0.4, (d) x = 0.6, and (e) x = 1.0.

5.3.3 Chemic al Stability and Microstructure

The chemical stability of the $GdBa_{1-x}Sr_xCo_2O_{5+\delta}$ cathodes in contact with the GDC and LSGM electrolyte was assessed by heating the mixed powders at 1100 °C, respectively, for 1 h and 0.5 h. Figure 5.7 compares the XRD patterns of the $GdBa_{1-x}Sr_xCo_2O_{5+\delta}$ and GDC mixtures after heating at 1100 °C for 1 h. Several new reflections corresponding to $BaCoO_{3-\delta}$ (JCPDS # 52-0429) can be noticed in Figures 5.7(a) and 5.7(b), indicating severe interfacial reaction of the $x = 0$ and 0.2 samples with GDC. However, further Sr substitution ($0.4 \leq x \leq 1.0$) greatly improves the chemical stability of the $GdBa_{1-x}Sr_xCo_2O_{5+\delta}$ samples with the GDC, showing no impurity reflections in Figure 5.7 (c) – (e). Figure 5.8 compares the XRD patterns of the $GdBa_{1-x}Sr_xCo_2O_{5+\delta}$ and LSGM mixtures after heating at 1100 ^{o}C for 0.5 h. While the $x = 0 – 0.4$ samples shows a weak impurity reflection at $2\theta \approx 30^{o}$ in Figures 5.8 (a) – (c), the $x = 0.6$ and 1.0 samples show no impurity reflections in Figures 5.8 (d) and (e). The results thus demonstrate that the substitution of Sr for Ba improves the chemical stability of the $GdBa_{1-x}Sr_xCo_2O_{5+\delta}$ samples in contact with the LSGM and GDC electrolytes at high temperatures.

The microstructures of the single cells were assessed by SEM. Figure 5.9 shows the cross sections of the $GdBa_{1-x}Sr_xCo_2O_{5+\delta}$ ($0 \leq x \leq 1.0$) cathode / composite electrode (cathode + LSGM) / LSGM electrolyte interfaces after the fuel cell performance test. Although the composite layer (cathode + LSGM) may not be necessary with the mixed conducting perovskite cathodes, it was introduced in the present study to provide good adhesion between the LSGM electrolyte and the $GdBa_{1-x}Sr_xCo_2O_{5+\delta}$ cathodes. While the bottom of the micrograph indicates a dense, well-sintered LSGM electrolyte, the upper portion shows the porous cathode/composite electrodes. The SEM images indicate good adhesion and continuous contact at the interfaces.

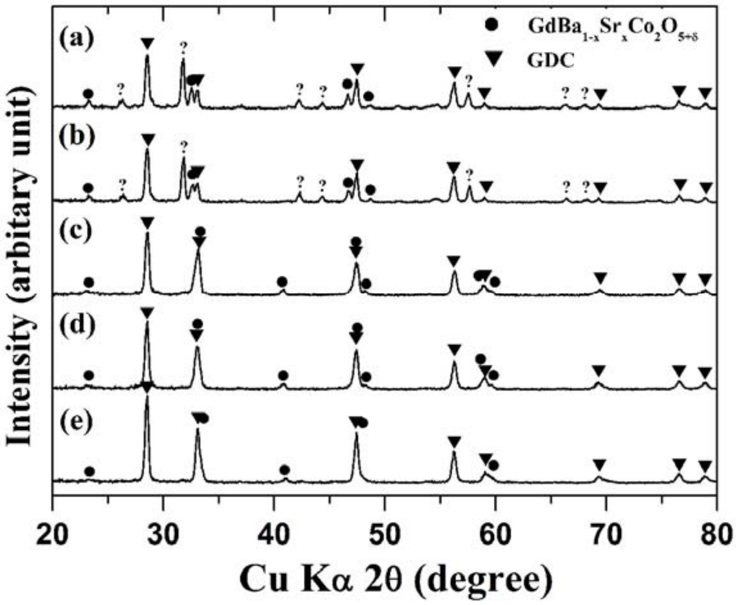

Figure 5.7 X-ray diffraction patterns of the $GdBa_{1-x}Sr_xCo_2O_{5+\delta}$ and GDC mixtures after firing at 1100 °C for 1 h in air: (a) x = 0, (b) x = 0.2, (c) x = 0.4, (d) x = 0.6, and (e) x = 1.0. Some of the reflections marked with ? belong to $BaCoO_{3-\delta}$.

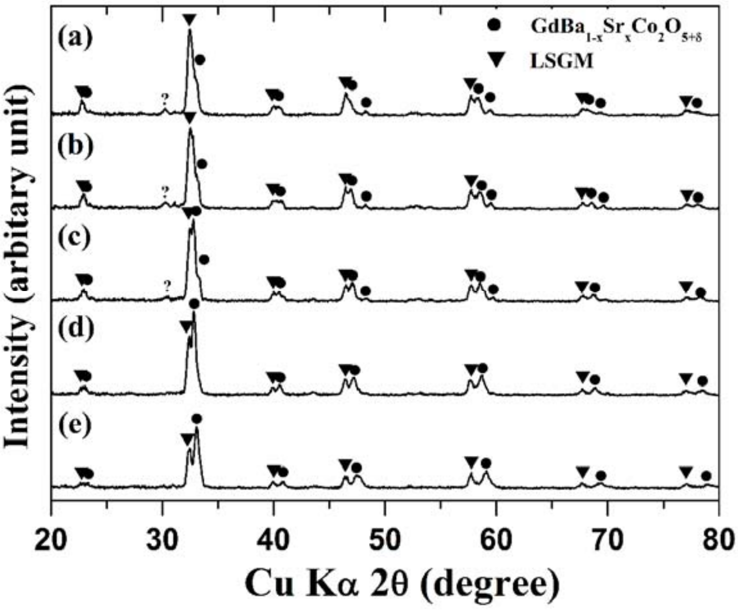

Figure 5.8 X-ray diffraction patterns of the $GdBa_{1-x}Sr_xCo_2O_{5+\delta}$ and LSGM mixtures after firing at 1100 °C for 0.5 h in air: (a) x = 0, (b) x = 0.2, (c) x = 0.4, (d) x = 0.6, and (e) x = 1.0. The reflections marked with ? belong to unknown phases.

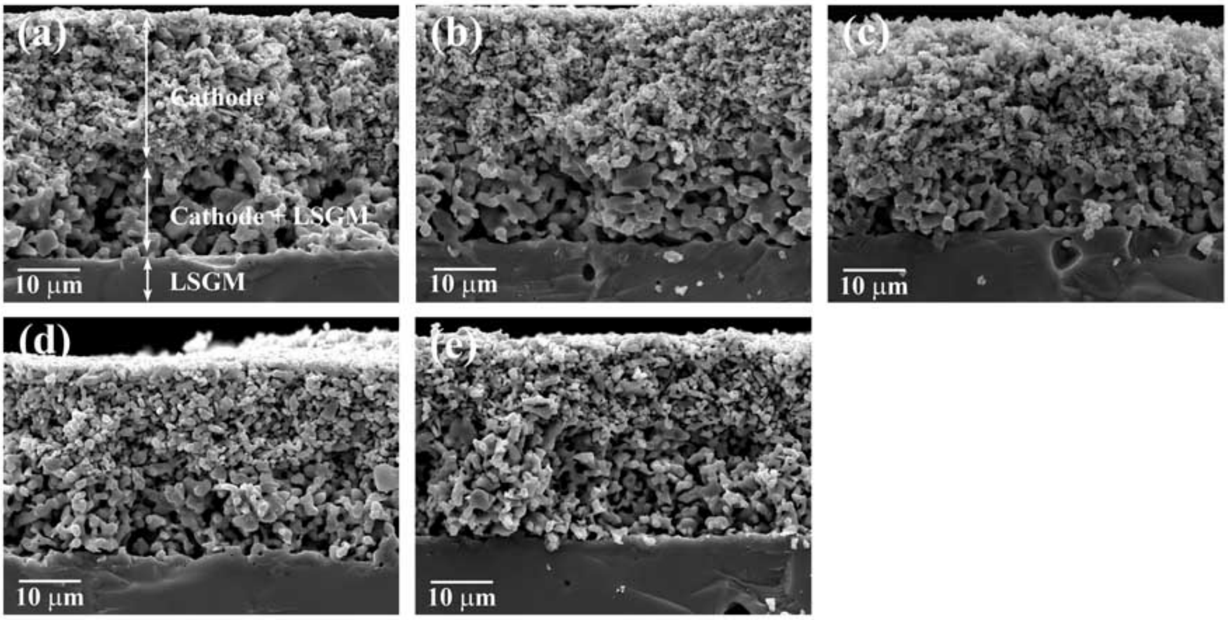

Figure 5.9 SEM micrographs showing the cross sections of the $GdBa_{1-x}Sr_xCo_2O_{5+\delta}$ / $GdBa_{1-x}Sr_xCo_2O_{5+\delta}$-LSGM composite / LSGM portion of single cell SOFC: (a) x = 0, (b) x = 0.2, (c) x = 0.4, (d) x = 0.6, and (e) x = 1.0.

5.3.4 Single Cell Performances

The single cell performance of the $GdBa_{1-x}Sr_xCo_2O_{5+\delta}$ cathodes in SOFC for the oxygen reduction reaction was evaluated using LSGM as an electrolyte. Figure 5.10 shows the current-voltage (*I*-*V*) curves and the corresponding power density curves measured at 700, 750, and 800 ^{o}C for the $GdBa_{1-x}Sr_xCo_2O_{5+\delta}$ ($0 \leq x \leq 1.0$) cathodes. The open-circuit voltages (OCV) of the $GdBa_{1-x}Sr_xCo_2O_{5+\delta}$ cells were typically 1.10 V at 800 ^{o}C, which is close to the theoretical value. There is a slight improvement in the fuel cell performance on substituting Ba partially by Sr (x = 0.2 and 0.6 samples) as seen in Figures 5.10 (b) and (d). For example, the maximum power density ($P_{\max}$) increased from 450 (x = 0) to 490 mW/cm^2 (x = 0.2 and 0.6). However, the x = 0.4 sample shows a slight decrease in $P_{\max}$ to 440 mW/cm^2 compared to the x = 0 sample, and the x = 1.0 sample exhibits the lowest performance with a $P_{\max}$ = 350 mW/cm^2. Since all the samples have high enough electrical conductivity as seen in Figure 5.6, the variations in the fuel cell performance of the $0 \leq x \leq 0.6$ samples could possibly be related to the changes in the ionic conductivity and catalytic activity. Recent studies on the oxide ion diffusion and surface exchange kinetics of the $LnBaCo_2O_{5+\delta}$ (Ln = Pr and Gd) samples have shown that the Ln = Pr sample with a tetragonal structure exhibits faster oxygen transport in the bulk and surface than the Ln = Gd sample with an orthorhombic structure.[103,104] Chapter 3 also showed that the Ln = Nd sample with a tetragonal structure in the $LnBaCo_2O_{5+\delta}$ system exhibits higher catalytic activity for the oxygen reduction reaction than the Ln = Sm and Gd samples with an orthorhombic structure. In addition, the oxygen permeability decreases from Ln = La to Nd to Sm due to a lowering of the crystal symmetry and lattice strain in the $LnBaCo_2O_{5+\delta}$. Therefore, the enhanced catalytic activity of the x = 0.2 and 0.6 samples (tetragonal) could be related to the faster oxygen transport compared to that in the x = 0 and 1.0 samples (orthorhombic).

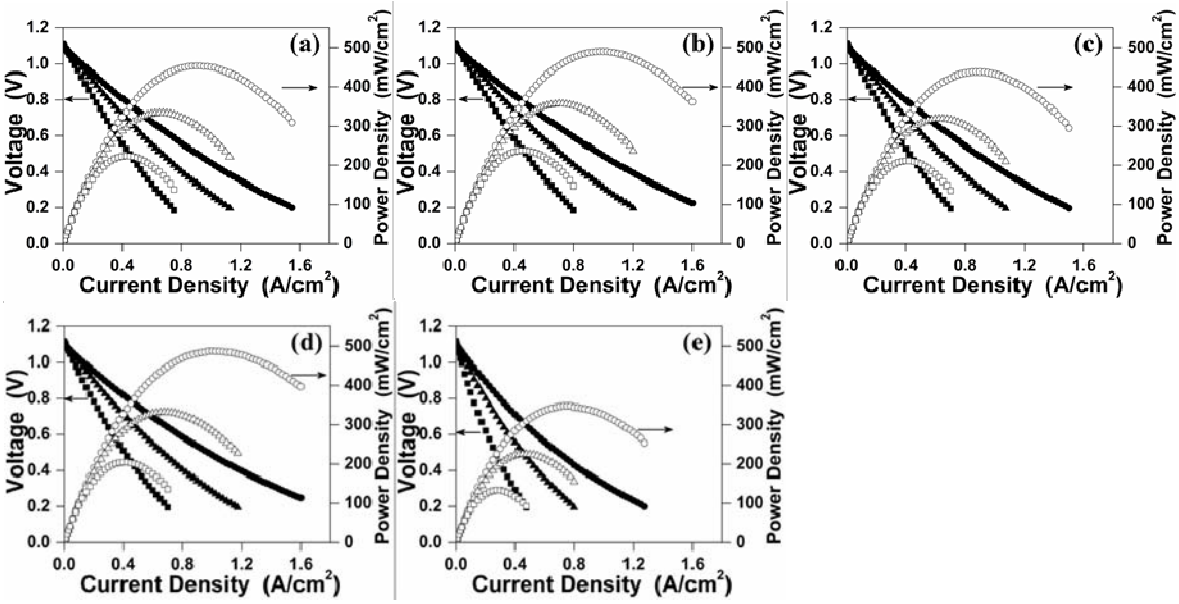

Figure 5.10 Electrochemical performance data of the $GdBa_{1-x}Sr_xCo_2O_{5+\delta}$ / $GdBa_{1-x}Sr_xCo_2O_{5+\delta}$-LSGM / LSGM/LDC/Ni-GDC single cells at 700 ^oC (square), 750 ^oC (triangle), and 800 ^oC (circle): (a) x = 0, (b) x = 0.2, (c) x = 0.4, (d) x = 0.6, and (e) x = 1.0.

5.4 CONCLUSIONS

The effect of Sr substitution for Ba in the layered perovskite $GdBa_{1-x}Sr_xCo_2O_{5+\delta}$ has been investigated. The $GdBa_{1-x}Sr_xCo_2O_{5+\delta}$ system exhibits a structural change from orthorhombic (x = 0) to tetragonal (x = 0.2 – 0.6) to orthorhombic (x = 1.0) with changes in space groups and an increase in oxygen content (5 + δ) with increasing Sr content. While the TEC decreases with increasing Sr content in the low temperature region (80 – 300 ^oC), it increases with Sr content in the high temperature region (300 – 900 ^oC). The $GdBa_{1-x}Sr_xCo_2O_{5+\delta}$ samples exhibit a metal to insulator (M-I) transition around 200 ^oC and the transition becomes less pronounced with increasing Sr content. At a given temperature, the electrical conductivity increases with increasing Sr content due to increasing oxygen content. While the parent $GdBaCo_2O_{5+\delta}$ sample suffers from interfacial reaction with LSGM and GDC electrolytes at 1100 °C, Sr substitution for Ba greatly improves the chemical stability of $GdBa_{1-x}Sr_xCo_2O_{5+\delta}$. The x = 0.2 and 0.6 samples exhibit higher power density in SOFC than the x = 0 and 1.0 samples partly due to faster oxygen transport with lower lattice strain compared to that in the x = 0 and 1.0 with an orthorhombic structure.

CHAPTER 6

Layered $NdBaCo_{2-x}Ni_xO_{5+\delta}$ Perovskite Oxides as Cathodes for Intermediate Temperature SOFC

6.1 INTRODUCTION

As discussed in the previous Chapters, the layered $LnBaCo_2O_{5+\delta}$ perovskites exhibit promising mixed ionic-electronic conducting (MIEC) properties and catalytic activities for the oxygen reduction reaction in SOFC. The TEC value decreases with decreasing size of the Ln^{3+} ions from Ln = La to Y due to the decreasing ionicity of the Ln-O bond. Although the $GdBaCo_2O_{5+\delta}$ has an advantage of lower TEC compared to other $LnBaCo_2O_{5+\delta}$, it suffers from side reactions with the electrolyte at high temperatures and with lower cathode performance. In Chapter 5, the effect of Sr substitution for Ba in the $GdBa_{1-x}Sr_xCo_2O_{5+\delta}$ system was systematically investigated. The results showed that Sr substitution improves the chemical stability and catalytic activity of $GdBa_{1-x}Sr_xCo_2O_{5+\delta}$. Unfortunately, TEC increases with Sr substitution and reaches the maximum value at $x = 0.6$.

The layered $NdBaCo_2O_{5+\delta}$ perovskites exhibited good cathode performance in SOFC and oxygen permeability comparable to those of the disordered perovskite $La_{0.5}Ba_{0.5}CoO_{3-\delta}$, but it still suffers from a high TEC value of 19.1×10^{-6} $^{o}C^{-1}$ in the temperature range of 80 – 900 ^{o}C (Chapters 2 and 3). The high TECs of the cobalt-based perovskite have been attributed to the low-spin to high-spin transition of the Co^{3+} ions[41] and the accompanying increase in ionic radius. Attempts such as partial substitution of other elements like Mn, Fe, and Ni for Co have been pursued to lower the TEC in the perovskite oxide system. Accordingly, in this Chapter, the substitution of Ni for Co in $NdBaCo_{2-x}Ni_xO_{5+\delta}$ is investigated with an aim to lower the TEC while maintaining its good cathode performance. The effect of Ni substitution on the crystal chemistry, thermal and electrochemical properties, and catalytic activity in SOFC of the layered $NdBaCo_{2-x}Ni_xO_{5+\delta}$ perovskite oxides is presented.

6.2 EXPERIMENTAL

6.2.1 Materials Synthesis

The layered $NdBaCo_{2-x}Ni_xO_{5+\delta}$ ($0 \leq x \leq 0.6$) perovskite oxides were synthesized by conventional solid-state reaction methods. Required amounts of Nd_2O_3, $BaCO_3$, Co_3O_4, and NiO were thoroughly mixed using ball-milling in ethanol for 24 h and calcined at 1000 °C for 12 h in air. The calcined powders were then ground, pressed into pellets, and sintered at 1250 °C for 12 h ($0 \leq x \leq 0.6$) in air, followed by cooling to room temperature at a rate of 4 °C/min. The resulting powders were also annealed at 900 °C for 6 h in air, followed by slow cooling to room temperature at a rate of 1 °C/min to maximize the oxygen content values. The LSGM and GDC electrolyte disks, the NiO-10GDC cermet anode, and LDC powder were synthesized as described in Chapter 2.

6.2.2 Characterization

The synthesized $NdBaCo_{2-x}Ni_xO_{5+\delta}$ samples were characterized by XRD, Rietveld refinement, iodometric titration, TGA, TMA, electrical conductivity, SEM, and single cell performance measurements as described in Chapter 2. The reactivity of the $NdBaCo_{2-x}Ni_xO_{5+\delta}$ ($0 \leq x \leq 0.6$) samples against GDC or LSGM electrolytes was evaluated by heating a mixture of the $NdBaCo_{2-x}Ni_xO_{5+\delta}$ and electrolyte powders at 1000 °C for 3 h in air.

6.2.3 Fabrication of Single Cells

Fuel cell performances of the $NdBaCo_{2-x}Ni_xO_{5+\delta}$ ($0 \leq x \leq 0.6$) cathodes were evaluated with both LSGM and GDC electrolyte-supported single cell SOFCs. The single cells consisted of cathode | GDC | LSGM(470 μm thickness) | LDC|Ni+10GDC for LSGM-supported cell and cathode | GDC(520 μm thickness) | Ni+10GDC for the GDC-supported cell. The single cell fabrication method is described in Chapter 2. The $NdBaCo_{2-x}Ni_xO_{5+\delta}$ ($0 \leq x \leq 0.6$) cathodes were prepared by the screen printing method and heated at 1000 °C for 3 h. The polarization resistance (R_p) of the $NdBaCo_{2-x}Ni_xO_{5+\delta}$ ($0 \leq x \leq 0.6$) cathodes in the LSGM-supported SOFCs was measured at different temperatures by ac impedance spectroscopy at open circuit voltages (OCV).

6.3 RESULTS AND DISCUSSION

6.3.1 Crystal Structure and Chemical Analysis

XRD data show that single-phase layered $NdBaCo_{2-x}Ni_xO_{5+\delta}$ perovskite could be obtained for $0 \leq x \leq 0.6$ after sintering at 1250 ^oC for 12 h, followed by cooling to room temperature at a rate of 4 ^oC/min (Figure 6.1). For higher Ni contents with $x > 0.6$, XRD patterns show the formation of impurity phases such as NiO and Nd_2NiO_4, indicating a Ni solubility limit of ~ 0.6 in the $NdBaCo_{2-x}Ni_xO_{5+\delta}$ system. This value is slightly higher compared to a Ni solubility of ~ 0.4 in the $GdBaCo_{2-x}Ni_xO_{5+\delta}$ system.[121] The XRD patterns of these as-synthesized $NdBaCo_{2-x}Ni_xO_{5+\delta}$ for $0 \leq x \leq 0.6$ could be indexed on the basis of an orthorhombic structure with the space group *Pmmm*.

Since the oxygen content may not be maximized on cooling the samples at a faster rate of 4 ^oC/min, the $NdBaCo_{2-x}Ni_xO_{5+\delta}$ ($0 \leq x \leq 0.6$) samples were also annealed at 900 ^oC for 6 h, followed by slow cooling to room temperature at a rate of 1 ^oC/min in air. Figure 6.2 shows the XRD patterns of these slow-cooled $NdBaCo_{2-x}Ni_xO_{5+\delta}$ ($0 \leq x \leq 0.6$) samples. For $0 \leq x \leq 0.4$, the XRD patterns in Figure 6.2 could be refined by the Rietveld analysis based on the tetragonal space group *P*4/*mmm*. There is good agreement between the observed and calculated profiles in Figure 6.2, and the quality of refinements and atomic positions are listed in Table 6.2. However, the XRD data of the x = 0.6 sample could not be satisfactorily refined with the tetragonal *P*4/*mmm* space group mainly due to the peak broadening at $2\theta \approx 46.5\ ^{o}$ and $77.5\ ^{o}$. This peak broadening can be understood to be due to the orthorhombic distortion with decreasing oxygen content. For example, the iodometric titration data in Table 6.1 indicate a decrease in oxygen content value from 5.85 at x = 0 to 5.75 at x = 0.6 in $NdBaCo_{2-x}Ni_xO_{5+\delta}$. Accordingly, the XRD data of the x = 0.6 sample in Figure 6.2 could be indexed with the orthorhombic space group *Pmmm*.

An earlier study on the $NdBaCo_2O_{5+\delta}$ sample with $(5 + \delta) = 5.69$ also suggested it to be orthorhombic (space group: *Pmmm*).[106] In our study, the $NdBaCo_{2-x}Ni_xO_{5+\delta}$ samples with $0 \leq x \leq 0.4$ have higher oxygen contents after slow cooling at a rate of 1 °C/min from 900 °C (Table 6.1) compared to the literature value of 5.69 for $NdBaCo_2O_{5+\delta}$, so they could be refined based on a tetragonal structure (space group: *P*4/*mmm*). The higher oxygen content values destroy the ordering of the oxygen vacancies, resulting in a tetragonal structure. However, the low X-ray scattering factor of the oxygen atoms compared to those of the heavier Ba and Nd atoms hinder us from observing the subtle orthorhombic distortion even if there is a weak ordering of oxygen vacancies. Future neutron diffraction studies will be helpful to observe the ordering of oxygen vacancies in the $NdBaCo_{2-x}Ni_xO_{5+\delta}$ ($0 \leq x \leq 0.6$) samples.

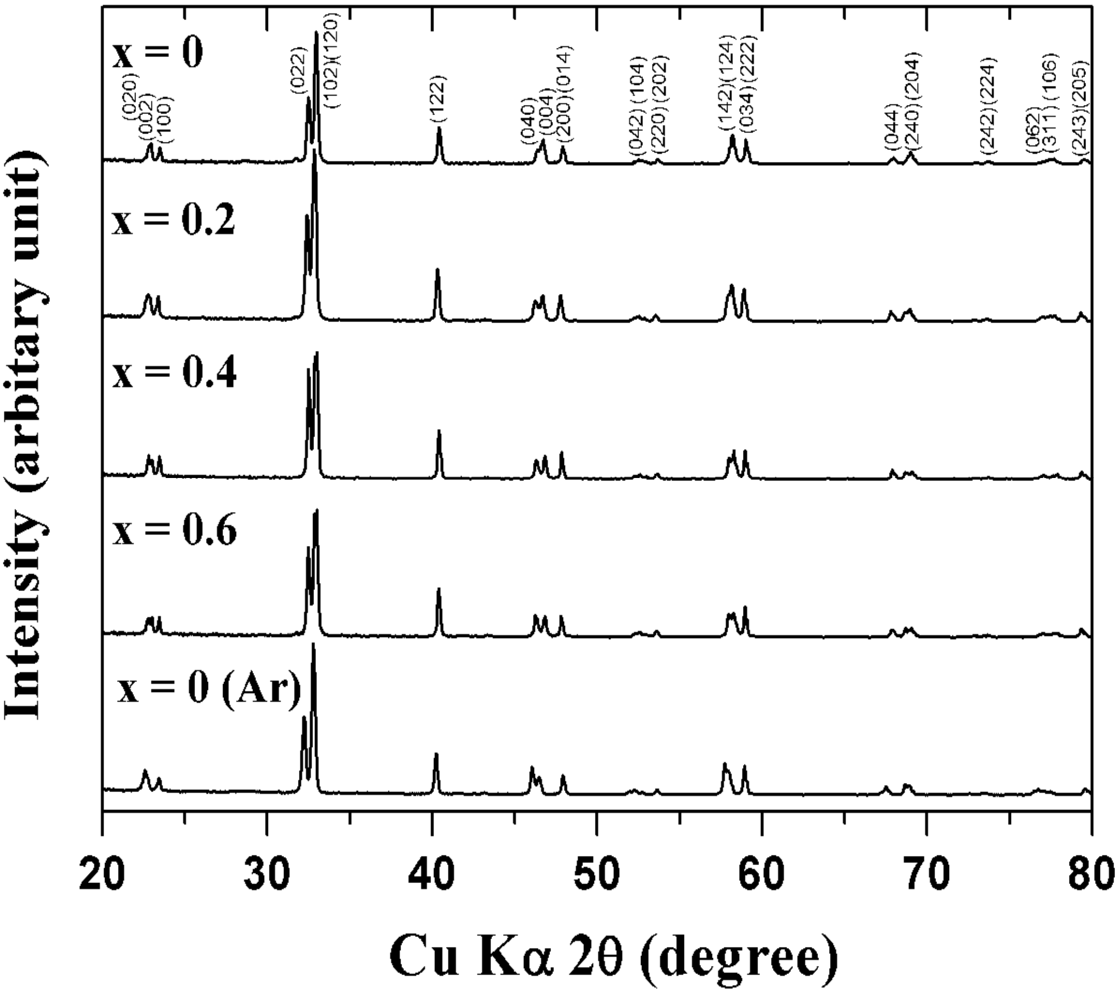

Figure 6.1 XRD patterns of the $NdBaCo_{2-x}Ni_xO_{5+\delta}$ samples sintered at 1250 °C for 12 h, followed by cooling to room temperature at a rate of 4 °C/min. The x = 0 (Ar) sample at the bottom refers to the x = 0 sample heated again at 900 °C for 3 h in Ar atmosphere after annealing in air at 900 °C for 6 h.

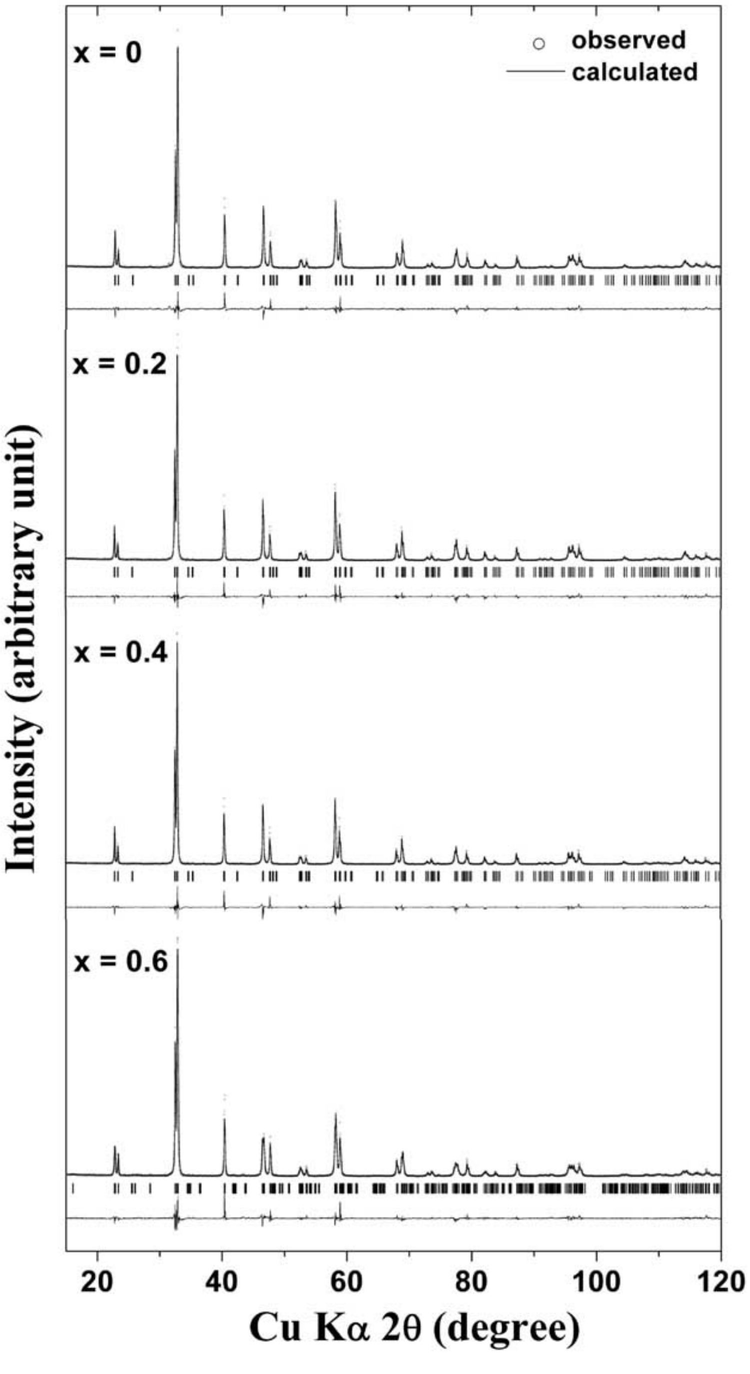

Figure 6.2 Observed and calculated XRD profiles and the difference between them for the $NdBaCo_{2-x}Ni_xO_{5+\delta}$ samples annealed at 900 °C for 6 h, followed by slow cooling at a rate of 1 °C/min in air. The vertical bars show the expected peak positions.

Table 6.1 Structural parameters, chemical analysis data, and TEC of the $NdBaCo_{2-x}Ni_xO_{5+\delta}$ oxides annealed at 900 °C for 6 h, followed by slow cooling at at a rate of 1 °C/min in air.

x	Space group	*a* (Å)	*b* (Å)	*c* (Å)	V(Å^3)	Oxidation state of (Co, Ni)	Oxygen content (5+δ)	TEC × 10^6 (°C^{-1}) 80 – 900 °C
0.0	*P*4/*mmm*	3.894	–	7.615	115.468	3.35	5.85	19.1
0.2	*P*4/*mmm*	3.894	–	7.619	115.529	3.33	5.83	18.1
0.4	*P*4/*mmm*	3.895	–	7.621	115.618	3.28	5.78	16.9
0.6	*Pmmm*	3.811	7.813	7.777	231.563	3.25	5.75	16.7
0.0(Ar)	*Pmmm*	3.793	7.874	7.808	233.194	2.93	5.43	–

Table 6 .2 Room temperature atomic positions of the NdBaCo$_{2-x}$Ni$_x$O$_{5+\delta}$ oxides annealed at 900 °C for 6 h, followed by slow cooling at a rate of 1 °C/min in air. For the tetragonal structure with the space group of *P*4/*mmm*, the atomic positions are Nd (0,0,1/2), Ba (0,0,0), (Co, Ni) (1/2,1/2,*z*), O1 (1/2,1/2,0), O2 (1/2,0,*z*), and O3 (1/2,1/2,1/2). For the orthorhombic structure with the space group of *Pmmm*, the atomic positions are Nd (1/2,*y*,1/2), Ba (1/2,*y*,0), (Co1,Ni1) (0,1/2,*z*), (Co2,Ni2) (0,0,*z*), O1 (0,0,0), O2 (0,1/2,0), O3 (0,1/2,1/2), O4 (0,0,1/2), O5 (1/2,0,z), O6 (1/2,1/2,*z*), and O7 (0,*y*,*z*).

Tetragonal *P*4/*mmm*	x = 0.0	x = 0.2	x = 0.4	Orthorhombic *Pmmm*	x = 0.6
(Co, Ni)(*z*)	0.250 (2)	0.250 (1)	0.250 (1)	Nd(*y*)	0.260 (1)
O2(*z*)	0.280 (2)	0.283 (1)	0.283 (2)	Ba(*y*)	0.252 (1)
χ^2	2.03	1.72	2.19	(Co1, Ni1)(*z*)	0.252 (2)
R_{Bragg}	3.44	4.32	3.96	(Co2, Ni2)(*z*)	0.263 (1)
				O5(*z*)	0.272 (5)
				O6(*z*)	0.270 (5)
				O7(*z*)	0.251 (3)
				O8(*z*)	0.256 (5)
				χ^2	1.88
				R_{Bragg}	4.21

The air-annealed x = 0 sample having the tetragonal structure in Figure 6.2 was heated again at 900 °C for 3 h in Ar atmosphere. Iodometric titration show this Ar-annealed sample to have an oxygen content of 5.43 compared to 5.85 for the air-annealed sample (Table 6.1). Accordingly, the XRD data of the Ar-annealed x = 0 sample could be fitted on the basis of the orthorhombic (x = 0 (Ar) sample in Figure 6.1). This result demonstrates the influence of oxygen content on the crystal chemistry of the $NdBaCo_2O_{5+\delta}$ sample.

Figure 6.3 shows the variations of the lattice parameters and unit cell volume with oxygen content ($5 + \delta$) in $NdBaCo_{2-x}Ni_xO_{5+\delta}$. It shows a linear increase in unit cell volume with decreasing oxygen content due to the reduction of (Co, Ni) ions. The degree of tetragonal distortion defined by the c/a ratio increases from 1.956 for the x = 0.0 sample to 1.957 for the x = 0.4 sample with increasing Ni content and decreasing oxygen content. Similarly, the orthorhombicity, $(b/2 - a)/(b/2 + a)$,[121] increases from 0.012 for the air-annealed x = 0.6 sample to 0.019 for the Ar-annealed x = 0.0 with decreasing oxygen content.

6.3.2 Thermal and Electrical Properties

Figure 6.4 shows the variations of oxygen content and the oxidation state of (Co, Ni) ions in $NdBaCo_{2-x}Ni_xO_{5+\delta}$ with temperature in air. These curves were derived using the initial oxygen contents determined by the iodometric titration and the TGA data. All the $NdBaCo_{2-x}Ni_xO_{5+\delta}$ ($0 \leq x \leq 0.6$) samples start to lose oxygen at

$T > 200$ °C with a corresponding decrease in the oxidation state of (Co, Ni) ions. They lose ~ 0.4 oxygen atoms per formula unit on heating to 900 °C.

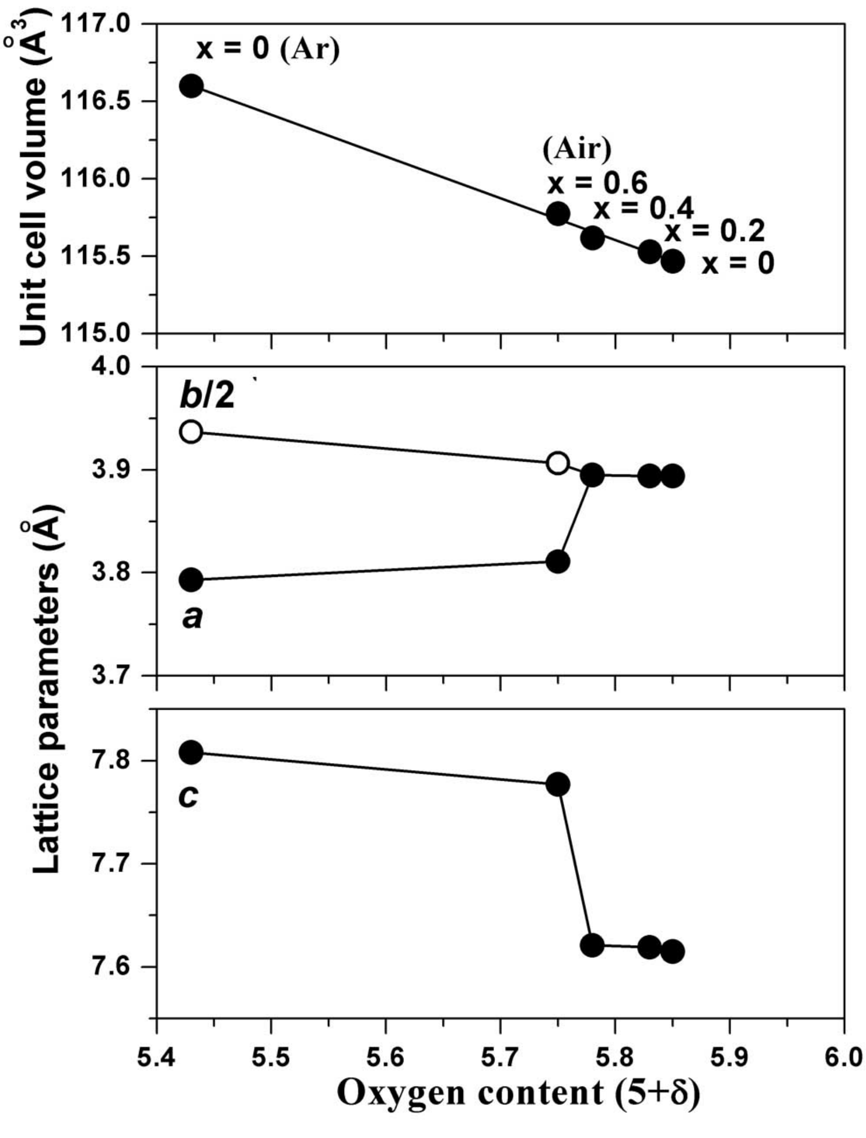

Figure 6.3 Variations of the lattice parameters and unit cell volume with oxygen content ($5 + \delta$) in $NdBaCo_{2-x}Ni_xO_{5+\delta}$. For the orthorhombic (*Pmmm*) phase, the unit cell volume is divided by two ($Z = 2$) for a comparison with that of the tetragonal (*P*4/*mmm*) phase ($Z = 1$).

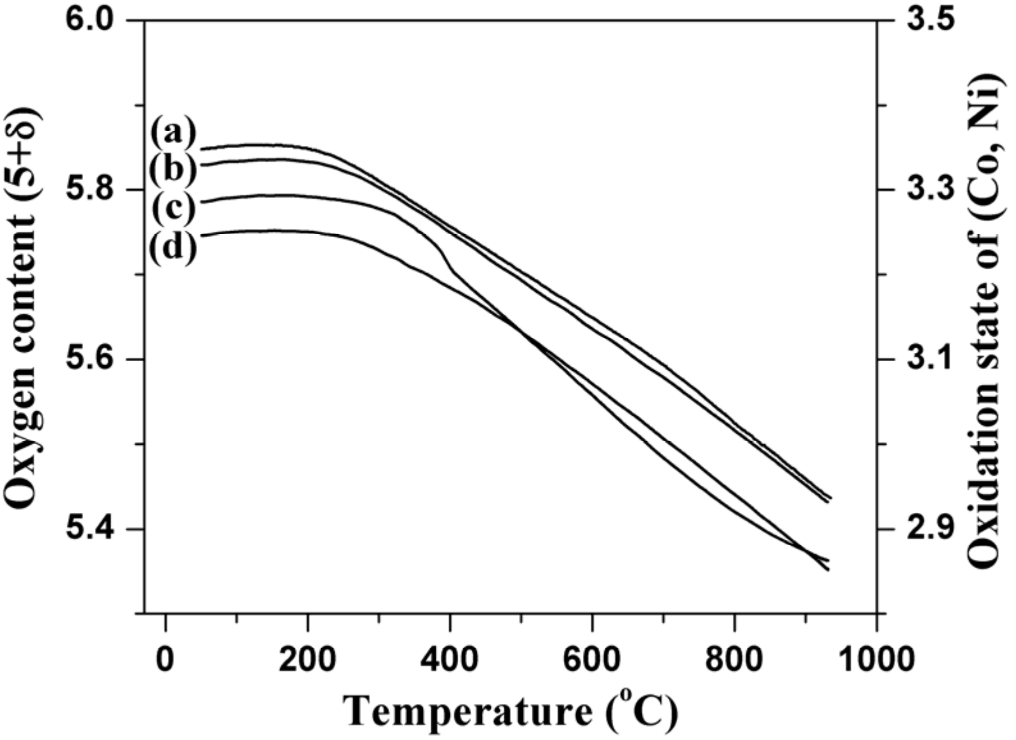

Figure 6.4 Variations of the oxygen contents and the oxidation state of the (Co, Ni) ions in $NdBaCo_{2-x}Ni_xO_{5+\delta}$ with temperature in air: (a) x = 0, (b) x = 0.2, (c) x = 0.4, and (d) x = 0.6.

The thermal expansion behaviors of the $NdBaCo_{2-x}Ni_xO_{5+\delta}$ ($0 \leq x \leq 0.6$) specimens were measured in air (Figure 6.5), and the average TEC values between 80 and 900 ^{o}C are given in Table 6.1. The slope of the thermal expansion curves increases with temperature due to oxygen loss and the consequent reduction of the (Co, Ni) ions (Figure 6.4). The parent $NdBaCo_2O_{5+\delta}$ sample with x = 0 has the highest TEC value of 19.1×10^{-6} $^{o}C^{-1}$, which is undesirable on combining in a SOFC with the electrolytes that typically have TECs of ~ 11 × 10^{-6} $^{o}C^{-1}$. The spin-state transition of the cobalt ions from low spin Co^{III} ($t_{2g}^{6}e_{g}^{0}$) to intermediate spin Co^{iii} ($t_{2g}^{5}e_{g}^{1}$) or high spin Co^{3+} ($t_{2g}^{4}e_{g}^{2}$) with increasing temperature has been reported to be the reason for the abnormally high TEC of such cobalt-based perovskite oxides.[41,119] However, the TEC value decreases with increasing Ni content x and reaches 16.7 × 10^{-6} $^{o}C^{-1}$ for the x = 0.6 sample, which is ~ 13 % lower than the TEC of the x = 0 sample. The decrease in TEC with Ni substitution is due to the decrease in the Co content and the absence of spin state transitions in nickel.

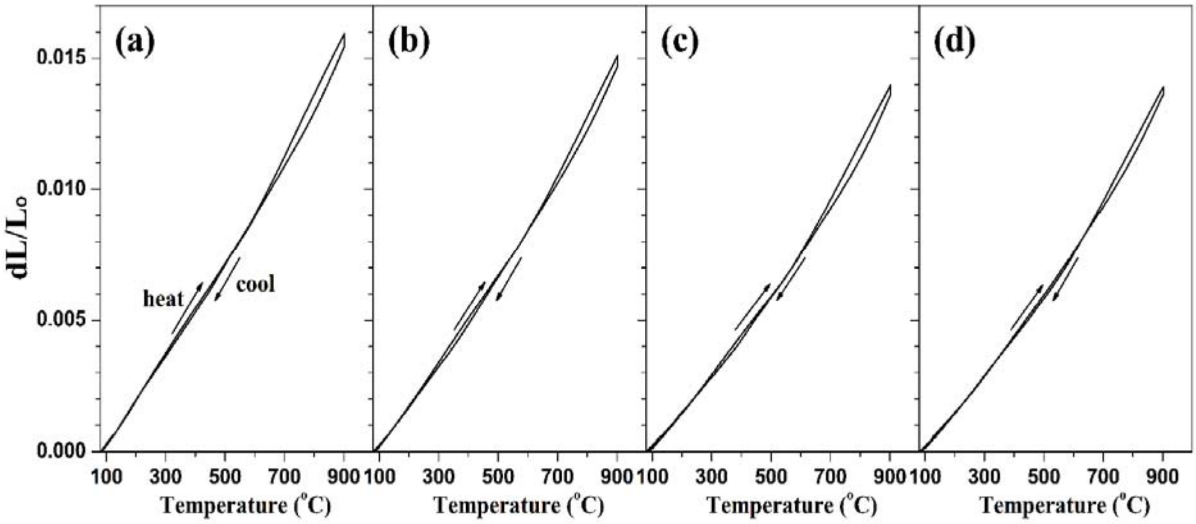

Figure 6.5 Thermal expansion (dL/L_o) curves of $NdBaCo_{2-x}Ni_xO_{5+\delta}$ in the temperature range of 80 – 900°C in air: (a) x = 0, (b) x = 0.2, (c) x = 0.4, and (d) x = 0.6.

Figure 6.6 shows the variations of the electrical conductivity with temperature of the $NdBaCo_{2-x}Ni_xO_{5+\delta}$ ($0 \leq x \leq 0.6$) samples. All the $NdBaCo_{2-x}Ni_xO_{5+\delta}$ samples show a decrease in electrical conductivity with increasing temperature due to the loss of oxygen from the lattice at higher temperatures (Figure 6.4). The formation of oxygen vacancies not only decreases the carrier concentration but also perturbs the (Co,Ni)–O–(Co,Ni) periodic potential, resulting in carrier localization.[91-93] At a given temperature, the electrical conductivity decreases with increasing Ni content in the $NdBaCo_{2-x}Ni_xO_{5+\delta}$ partly due to the increasing amount of oxygen vacancies. However, all the $NdBaCo_{2-x}Ni_xO_{5+\delta}$ samples show conductivity > 300 S/cm up to 900 °C, which is adequate for them to be employed as cathodes in SOFC.[12]

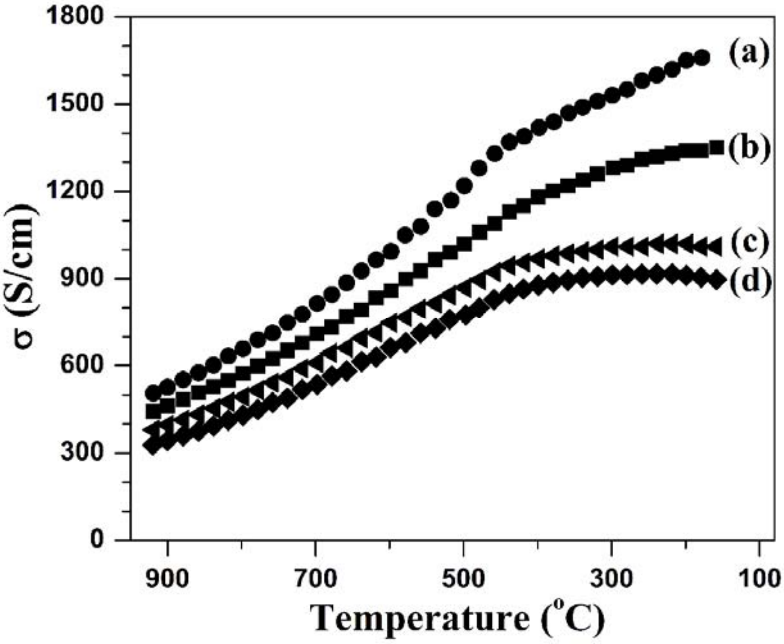

Figure 6.6 Variations of the electrical conductivity of $NdBaCo_{2-x}Ni_xO_{5+\delta}$ with temperature in air: (a) x = 0, (b) x = 0.2, (c) x = 0.4, and (d) x = 0.6.

6.3.3 Chemical Stability and Microstructure

Chemical stability of the $NdBaCo_{2-x}Ni_xO_{5+\delta}$ sample in contact with the GDC and LSGM electrolytes was assessed by heating the mixtures at 1000 ^oC for 3 h. Figure 6.7 (a) shows the XRD patterns of the $NdBaCo_{2-x}Ni_xO_{5+\delta}$ and GDC mixture after heating at 1000 ^oC for 3 h. While the x = 0.2 sample shows small unknown peaks at $2\theta \approx 41$ and 50.8^o due to slight side reaction with GDC, the x = 0, 0.4, and 0.6 samples show no reaction with GDC. Figure 6.7(b) shows the XRD patterns of the $NdBaCo_{2-x}Ni_xO_{5+\delta}$ and LSGM mixture after heating at 1000 ^oC for 3 h. Reflections corresponding to impurity phases develop at $2\theta \approx 29$ - 31^o with increasing Ni content, indicating a reaction with LSGM. However, the $NdBaCo_{2-x}Ni_xO_{5+\delta}$ cathode could be used with the LSGM electrolyte by applying a GDC buffer layer between the cathode and the electrolyte.

6.3.4 Single Cell Performances

Figure 6.8 shows the variations of open-circuit voltages (OCV) of the GDC and LSGM-supported SOFCs with temperature. The OCVs of GDC-supported single cells are ~ 0.95 V at 600 ^oC and decrease rapidly with increasing temperature. These OCVs are significantly lower than the theoretical values obtained from Nernst

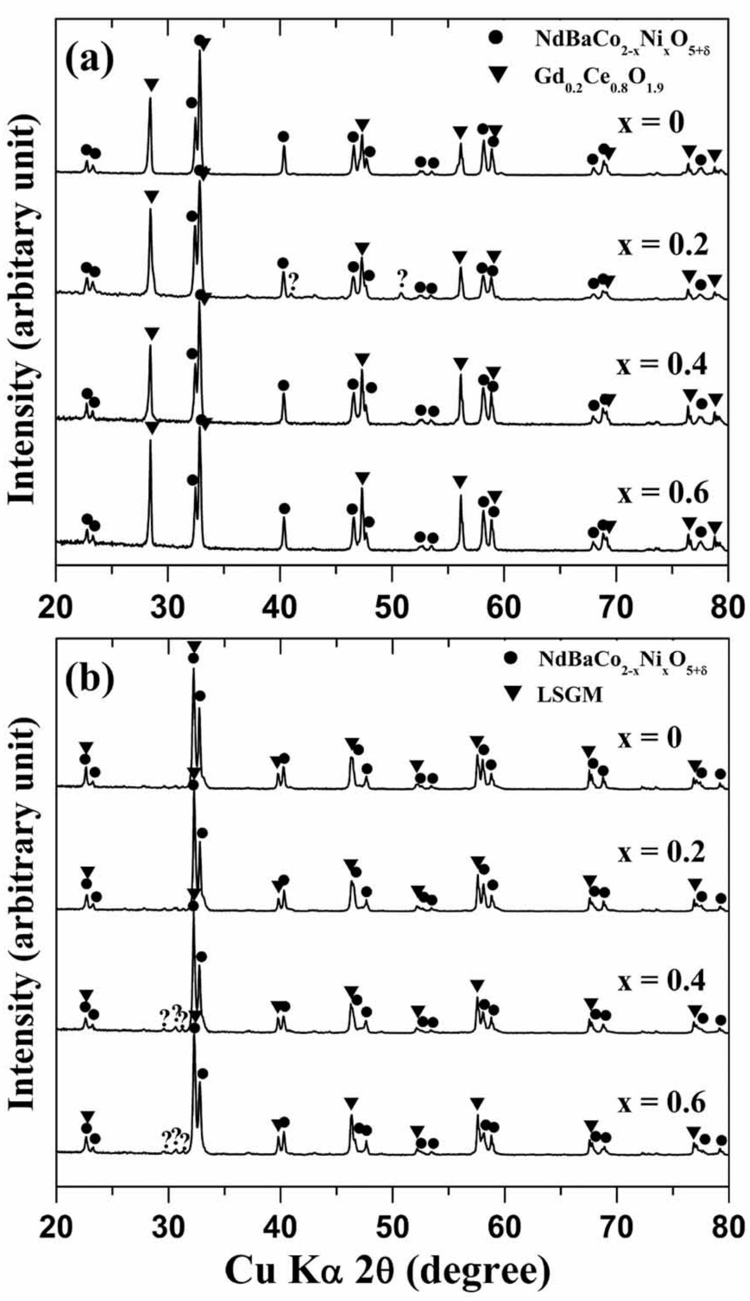

Figure 6.7 XRD patterns recorded after heating at 1000 °C for 3 h in air mixtures consisting of $NdBaCo_{2-x}Ni_xO_{5+\delta}$ and (a) GDC or (b) LSGM electrolytes. The reflections marked with ? belong to unknown phases formed by a reaction between $NdBaCo_{2-x}Ni_xO_{5+\delta}$ and GDC or LSGM.

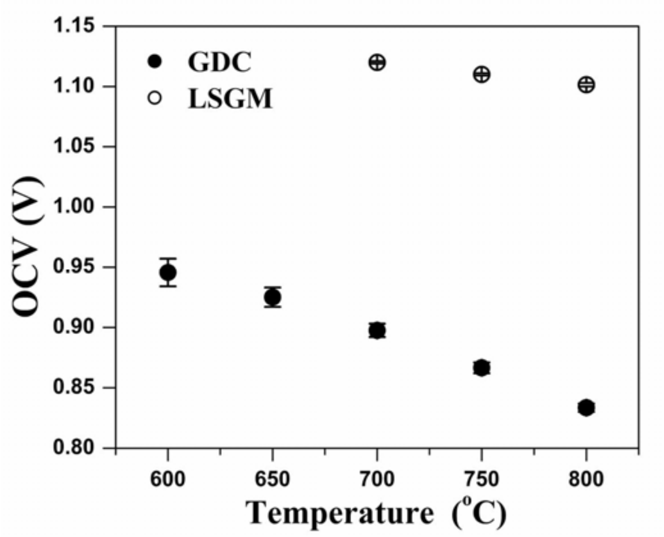

Figure 6.8 Comparison of the OCVs of the GDC- and LSGM-supported single cells at various temperatures. Humidified H_2 and air were supplied as fuel and oxidant, respectively.

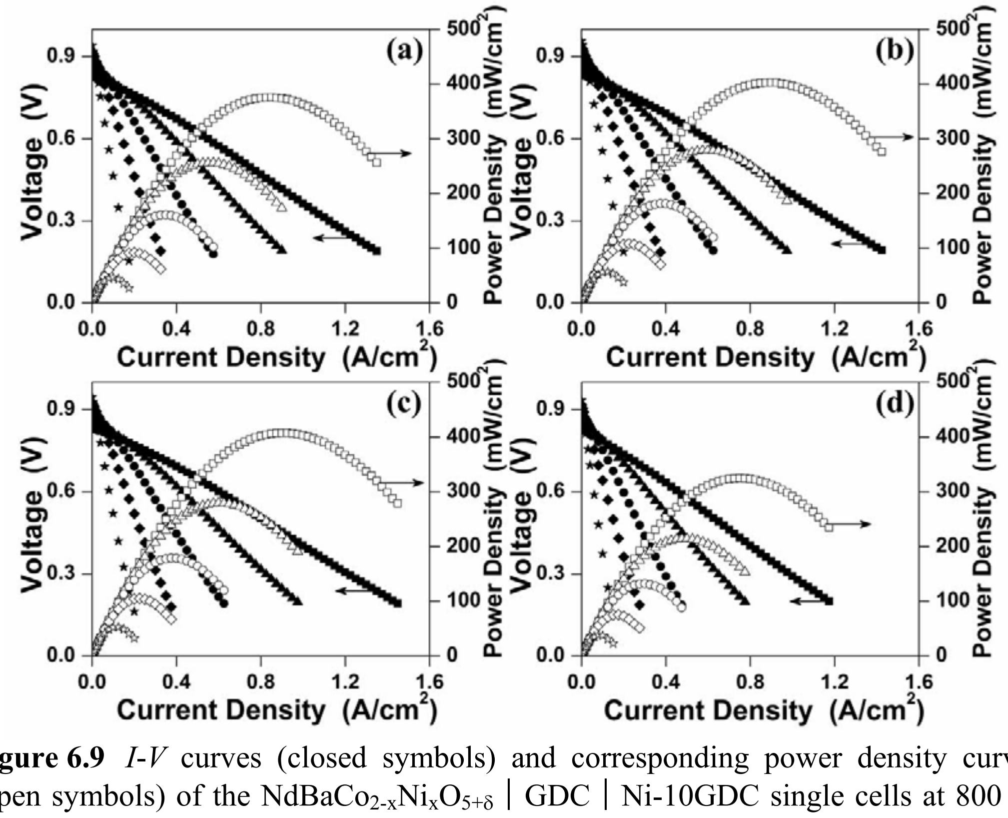

Figure 6.9 *I-V* curves (closed symbols) and corresponding power density curves (open symbols) of the $NdBaCo_{2-x}Ni_xO_{5+\delta}$ | GDC | Ni-10GDC single cells at 800 °C (square), 750 °C (triangle), 700 °C (circle), 650 °C (diamond), and 600 °C (star): (a) x = 0, (b) x = 0.2, (c) x = 0.4, and (d) x = 0.6.

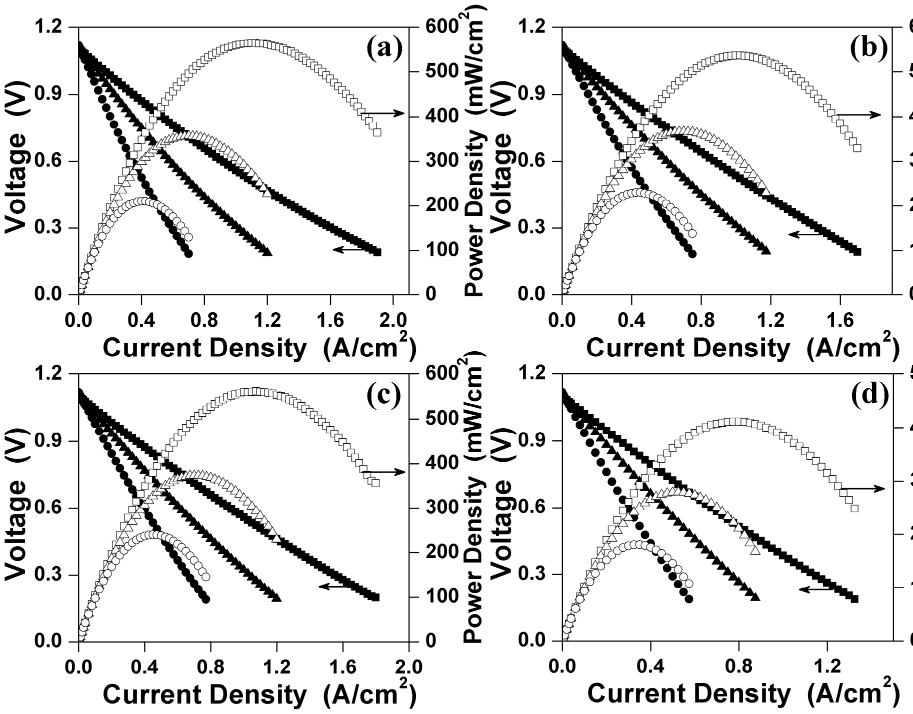

Figure 6.10 *I-V* curves (closed symbols) and corresponding power density curves (open symbols) of the NdBaCo$_{2-x}$Ni$_x$O$_{5+\delta}$ | GDC | LSGM | LDC | Ni-10GDC single cells at 800 ^{o}C (square), 750 ^{o}C (triangle), and 700 ^{o}C (circle): (a) x = 0, (b) x = 0.2, (c) x = 0.4, and (d) x = 0.6.

equation due to the reduction of the Ce^{4+} ions and the consequent increase in electronic conduction with increasing temperature.[122,123] On the contrary, the LSGM-supported SOFCs show high OCVs close to the theoretical value due to the good stability of the LSGM electrolyte in hydrogen atmosphere.

Figures 6.9 and 6.10 show the current-voltage (*I-V*) curves and the corresponding power density curves obtained with the GDC and LSGM-supported SOFCs at various temperatures. At a given current density and temperature, the GDC-supported SOFCs exhibit lower voltages than the LSGM-supported cells due to the lower OCVs (Figure 6.8) and slightly thicker electrolyte (520 μm) compared to the LSGM electrolyte (470 μm). From the fuel cell performance tests, the variations of the maximum power density with Ni content at 700, 750, and 800 °C are plotted in Figure 6.11. The x = 0.2 and 0.4 samples show performance similar to or slightly better than the x = 0 sample, while the x = 0.6 sample shows the lowest performance.

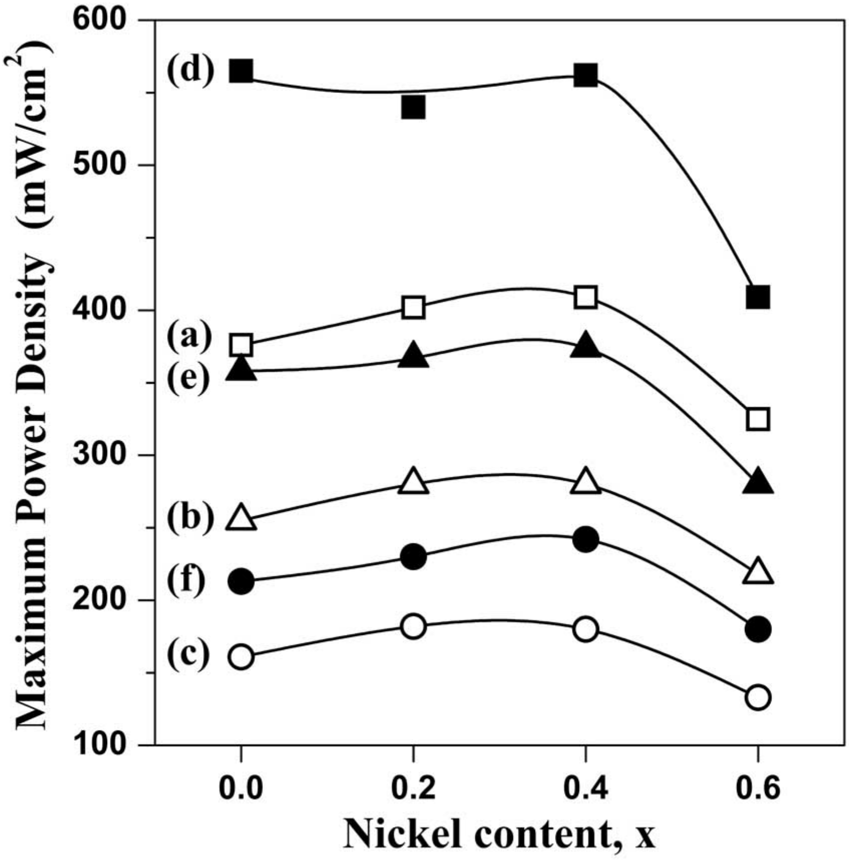

Figure 6.11 Variations with Ni content x of the maximum power density obtained with the GDC-supported single cells at (a) 800 °C, (b) 750 °C, (c) 700 °C and LSGM-supported single cells at (d) 800 °C, (e) 750 °C, and (f) 700 °C.

Figure 6.12 shows the variations of the total polarization conductance (R_p^{-1}) of the $NdBaCo_{2-x}Ni_xO_{5+\delta}$ ($0 \leq x \leq 0.6$) cathode with temperature. The cathode polarization conductance increases from x = 0 to x = 0.4 but shows the lowest value for the x = 0.6 sample, which is consistent with the SOFC performance data in Figure 6.11. From the Arrhenius plots of the cathode polarization conductance, the activation energies were calculated to be 1.59 eV (x = 0), 1.48 eV (x = 0.2), 1.37 eV (x = 0.4), and 1.28 eV (x = 0.6). It is noteworthy that the Ni substitution lowers the activation energy for the polarization conductance of the $NdBaCo_{2-x}Ni_xO_{5+\delta}$ cathodes.

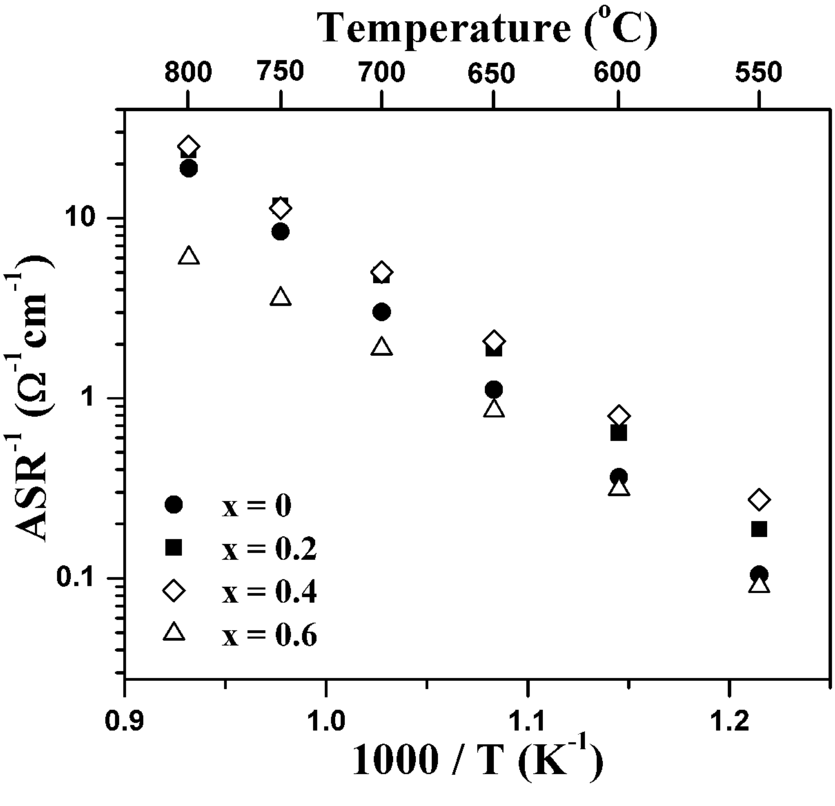

Figure 6.12 Variations of the total polarization conductance (R_p^{-1}) of the $NdBaCo_{2-x}Ni_xO_{5+\delta}$ ($0 \leq x \leq 0.6$) cathodes with temperature.

Cathode performances in SOFC measured with the GDC and LSGM electrolytes (Figures. 6.9-6.11) and the cathode polarization conductance data (Figure 6.12) reveal that a substitution of a small amount of Ni (x = 0.2 and 0.4) for Co offers performances comparable to or even slightly better than that of the x = 0 sample, but with an important advantage of lower TEC. Considering the TEC values (Table 6.1), chemical stability with the electrolytes (Figure 6.7), and fuel cell performance (Figures. 6.9–6.11), the x = 0.4 sample is the optimum composition in the $NdBaCo_{2-x}Ni_xO_{5+\delta}$ system as a cathode in SOFC. The enhanced performance of the x = 0.4 could be understood to be partly due to the increasing amount of oxygen vacancies with Ni substitution (Figure 6.4) that may improve the surface exchange of oxygen on the $NdBaCo_{2-x}Ni_xO_{5+\delta}$ cathodes.[11] However, further Ni substitution (x = 0.6) deteriorates the bulk oxygen transport due to the orthorhombic distortion and increasing amount of the low spin Ni^{III} which could trap oxygen vacancies.[119,124] Future in-depth transport studies could shed more light on the oxygen transport mechanisms in the layered $NdBaCo_{2-x}Ni_xO_{5+\delta}$ perovskite system.

6.4 CONCLUSIONS

With an aim to develop new cathode materials for intermediate temperature SOFC, the mixed conducting $NdBaCo_{2-x}Ni_xO_{5+\delta}$ ($0 \le x \le 0.6$) oxides with a layered perovskite structure have been investigated. The air-synthesized $NdBaCo_{2-x}Ni_xO_{5+\delta}$ has a tetragonal structure (space group of *P*4/*mmm*) for $0 \le x \le 0.4$, while showing an orthorhombic distortion (space group of *Pmmm*) for x = 0.6. The oxygen content, oxidation state of the (Co, Ni) ions, and TEC decrease with increasing Ni content. Although electrical conductivity decreases with increasing Ni content, all the $NdBaCo_{2-x}Ni_xO_{5+\delta}$ samples show conductivity > 300 S/cm up to 900 ^oC, which is adequate for employing them as cathodes in SOFC. Substitution of a small amount of Ni (x = 0.2 and 0.4) for Co leads to slightly improved performance in SOFC with an important advantage of lower TEC. Considering the TEC value, chemical stability with the electrolytes, and catalytic activity, the x = 0.4 sample represents an optimum composition in the $NdBaCo_{2-x}Ni_xO_{5+\delta}$ system for use as a cathode in intermediate temperature SOFC.

PART II

NON-PEROVSKITE OXIDE CATHODE MATERIALS FOR INTERMEDIATE TEMPERATURE SOFC

CHAPTER 7

Low Thermal Expansion $RBa(Co,M)_4O_7$ Cathodes Based on Tetrahedral-site Cobalt Ions for IT-SOFC

7.1 INTRODUCTION

The cobalt-containing cathodes with perovskite (*e.g.* LSC) or perovskite-related structure have become appealing due to their good MIEC properties at intermediate temperatures (500-800 °C). However, the high thermal expansion coefficient (TEC) of such cobalt-based oxides has impeded their practical applications. For example, $La_{0.6}Sr_{0.4}CoO_3$ has a TEC of 20.5×10^{-6} $^{o}C^{-1}$ which is too high compared to the TECs (10.0×10^{-6} to 12.5×10^{-6} $^{o}C^{-1}$) of standard oxide-ion electrolytes like yttria-stabilized zirconia (YSZ), gadolinia-doped ceria (GDC), and $La_{1-x}Sr_xGa_{1-y}Mg_yO_{3-\delta}$ (LSGM).[27,94] The large thermal expansion mismatch between the cathode and electrolyte can lead to delamination of or cracks in the cathode layer during the thermal cycling of SOFC.[3]

The abnormally high TECs of the cobalt-based perovskite and perovskite-related oxides have been attributed to the low-spin to high-spin transition of octahedral-site Co^{3+} ions[41] and the accompanying increase in ionic radius. Figure 7.1(a) shows, for example, the crystal structure of $(La,Sr)CoO_3$ pervoskite oxide, in which the corner-shared CoO_6 octahedra form a three-dimensional network. Attempts such as partial substitution of other elements like Mn, Fe, and Ni for Co have been pursued to lower the TEC, and the Fe-rich $La_{1-x}Sr_xFe_{1-y}Co_yO_{3-z}$ (LSFC) shows moderate TEC with acceptable cathode performance on employing it as a LSCF + electrolyte composite cathode.[29,44] The decreasing Co content in LSFC offers a trade-off between cathode performance and TEC. Thus, the high TEC of cobalt-rich perovskite or perovskite-related oxides remains an intrinsic problem to overcome.

Recently, $RBaCo_{4-x}M_xO_7$ **(**R = Y, Ca, In, Lu, Yb, Tm, Er, Ho, and Dy and M = Co, Zn, Fe, Al, and Ga) with a hexagonal structure has attracted interest as a potential oxygen storage material since it absorbs/desorbs a large amount of oxygen into/from the lattice at low temperatures of 200 – 400 °C in addition to exhibiting interesting magnetic properties.[125-129] Unlike the perovskite-based oxides, $RBa(Co,M)_4O_7$ consists of corner-shared $(Co,M)O_4$ tetrahedra with the Ba^{2+} and R ions adopting, respectively, 12- and 6-fold oxygen coordination (Figure 7.1 (b)).[126] Unfortunately, $YBaCo_{4-x}Fe_xO_7$ ($0 \leq x \leq 0.8$), belonging to the $RBaCo_{4-x}M_xO_7$ family**,** suffers from phase decomposition at elevated temperatures of 700 – 800 °C, which prevents its use in practical devices.[128] Although a recent report on $YBaCo_{4-x}Zn_xO_7$ ($1 \leq x \leq 3$) showed low oxygen adsorption at high temperatures by thermogravimetric analysis,[129] there was no direct investigation of the phase stability of the $RBaCo_{4-x}M_xO_7$ series and their potential for SOFC applications.

With an aim to overcome the phase instability problem and to apply them as cathodes in SOFC, we present here an investigation of various compositions in the

$RBaCo_{4-x}M_xO_7$ series (R = Y, Ca, In, or mixtures thereof and M = Zn, Fe, Al, or mixtures thereof) as illustrated in Figure 7.2.

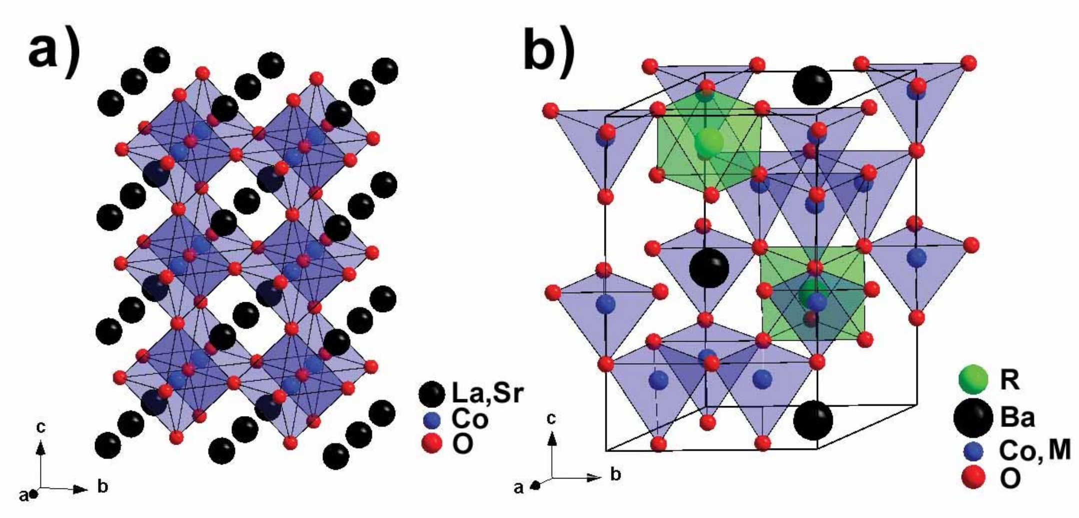

Figure 7.1 (a) Crystal structure of perovskite $La_{1-x}Sr_xCoO_3$ and (b) crystal structure of $RBa(Co,M)_4O_7$.

7.2 EXPERIMENTAL

7.2.1 Materials Synthesis

The $RBaCo_{4-x}M_xO_7$ series (R = Y, Ca, In, or mixtures thereof and M = Zn, Fe, Al, or mixtures thereof) samples were synthesized by conventional solid-state reaction methods. Required amounts of Y_2O_3, $CaCO_3$, In_2O_3, $BaCO_3$, Co_3O_4, ZnO, Al_2O_3, and Fe_2O_3 were thoroughly mixed by ball milling in ethanol for 24 h and calcined at 1000 ^{o}C for 12 h in air. The calcined powders were then ground, pressed into pellets, and sintered at 1100 – 1200 °C for 12 h in air. The $La_{0.6}Sr_{0.4}Co_{0.2}Fe_{0.8}O_3$ (LSCF) powders were synthesized by the glycine-nitrate combustion method, followed by sintering at 1200 °C for 12 h.[130] The LSCF powder was finally sintered at 1200 °C for 12 h. The LSGM and GDC electrolyte disks, the NiO-10GDC cermet anode, and LDC powder were synthesized as described in Chapter 2.

7.2.2 Phase Stability Tests

The phase stabilities of the $RBaCo_{4-x}M_xO_7$ powders were assessed by three different methods. Method 1 is a temperature-programmed phase stability measurement, which involves rapidly heating the sample to 1000 °C, followed by slowly cooling to room temperature at a rate of 2 °C min^{-1} with intermediate dwellings for 4 h at every 100 °C from 1000 °C to 200 °C (Figure 7.3 (a)). Method 2 is a long-term phase stability measurement, which involves heating the sample powder at 600, 700, 800, or 900 °C for > 50 h to provide enough time for the phase decomposition to occur, followed by quenching to room temperature. These experiments with methods 1 and 2 were carried out by placing the $RBaCo_{4-x}M_xO_7$ powders on top of pellets with the same compositions to prevent contact with the alumina crucible and any possible diffusion of Co into alumina. Method 3 is a high temperature XRD measurement, which involves the recording of the XRD pattern of the $RBaCo_{4-x}M_xO_7$ sample with increasing temperature after dwelling for 4 h at each temperature before recording.

7.2.3 Cha racterization

The synthesized $RBaCo_{4-x}M_xO_7$ samples were characterized by XRD, high temperature XRD, iodometric titration, TGA, dilatometer, electrical conductivity, SEM, oxygen permeation measurements, and single cell performance measurements as described in Chapter 2. The chemical stability of the $YBaCo_{4-x}Zn_xO_7$ samples against YSZ, GDC, or LSGM electrolytes was evaluated by heating a mixture of the $YBaCo_{4-x}Zn_xO_7$ and electrolyte powders at 1000 ^oC for 3 h or 1100 ^oC for 2 h in air. The polarization resistance (R_p) of the $YBaCo_{4-x}Zn_xO_7$ cathode in contact with GDC pellets (0.75 mm thickness) was measured using symmetrical cells in the temperature range of 500 – 800 ^oC by AC impedance spectroscopy (Solartron 1260 FRA).

7.2.4 Oxygen Permeation Measurements

Oxygen permeation measurements were carried out with coin-type $YBaCo_3ZnO_7$ pellets that had a thickness of 2.33 mm and > 90 % of theoretical density as described in Chapter 2.

7.2.5 Fabrication of Single Cells

Fuel cell performances of the $YBaCo_{4-x}Zn_xO_7$ ($1.0 \leq x \leq 2.0$) cathodes were evaluated with LSGM-electrolyte (0.5 mm thick) supported single cells. The single cell consists of cathode | GDC|LSGM(500 μm thickness) | LDC | Ni+10GDC. The single cell fabrication method is described in Chapter 2. For the cathode, the $YBaCo_{4-x}Zn_xO_7$ and $YBaCo_{4-x}Zn_xO_7$ + GDC layers were heated, respectively, at 900 and 950 °C for 3 h, while the LSCF layer were heated at 1050 °C for 2 h.

7.3 RESULTS AND DISCUSSION

7.3.1 High Temperature Phase Stability

Figure 7.2 shows the various compositions investigated in the $RBaCo_{4-x}M_xO_7$ series with R = Y, Ca, and In and M = Zn, Al, and Fe. The room-temperature oxygen contents ($7 \pm \delta$), oxidation state of (Co,Fe) ions, and lattice parameters of the as-synthesized $RBaCo_{4-x}M_xO_7$ powders are listed in Table 7.1. Their phase stabilities were assessed by three different methods: (1) temperature-programmed phase stability measurement (Figure 7.3 (a)), (2) long-term phase stability measurement by heating the samples at 600, 700, 800, and 900 °C for > 50 h, and (3) high temperature XRD measurements.

Figure 7.3 (b) reveals that the $YBaCo_4O_7$ sample decomposes severely into Y_2O_3, $BaCoO_{3-\delta}$, Co_3O_4, and some unknown phases during the temperature-programmed phase stability test (method 1). In contrast, the Zn-substituted $YBaCo_{4-x}Zn_xO_7$ ($0.5 \leq x \leq 2$) samples do not undergo any decomposition during such temperature programmed phase stability test. Figure 7.4 gives the results of the long-term phase stability measurements (method 2) of the $YBaCo_{4-x}Zn_xO_7$ ($0 \leq x \leq 2.0$)

Table 7.1 Structural and chemical analysis data of as-synthesized $RBaCo_{4-x}M_xO_{7\pm\delta}$ at room temperature.

Composition	*a* (Å)	*b* (Å)	*c* (Å)	V(Å^3)	Oxidation state of (Co, Fe)	Oxygen content (7 ± δ)
$YBaCo_4O_{7\pm\delta}$	6.303	-	10.247	352.541	2.30	7.10
$YBaCo_{3.5}Zn_{0.5}O_{7\pm\delta}$	6.305	-	10.262	353.291	2.34	7.10
$YBaCo_3ZnO_{7\pm\delta}$	6.310	-	10.273	354.231	2.38	7.07
$YBaCo_{2.5}Zn_{1.5}O_{7\pm\delta}$	6.312	-	10.285	354.870	2.44	7.05
$YBaCo_2Zn_2O_{7\pm\delta}$	6.318	-	10.288	355.648	2.53	7.03
$YBaCo_2ZnFeO_{7\pm\delta}$	6.320	-	10.281	355.631	2.52	7.28
$CaBaCo_3ZnO_{7\pm\delta}$	6.340	-	10.208	355.345	2.68	7.02
$CaBaCo_3FeO_{7\pm\delta}$	6.337	-	10.244	356.260	2.54	7.08
$CaBaCo_3AlO_{7\pm\delta}$	6.312	-	10.130	349.522	2.38	7.07
$InBaCo_2Zn_2O_{7\pm\delta}$	6.254	-	10.183	344.923	2.52	7.02
$Y_{0.5}Ca_{0.5}BaCo_3ZnO_{7\pm\delta}$	6.326	-	10.246	355.094	2.57	7.11
$Y_{0.5}In_{0.5}BaCo_3ZnO_{7\pm\delta}$	6.276	-	10.225	348.787	2.35	7.03
$Ca_{0.5}In_{0.5}BaCo_{2.5}Zn_{1.5}O_{7\pm\delta}$	6.293	-	10.209	350.130	2.57	6.96

Lattice parameters of all $RBaCo_{4-x}M_xO_{7\pm\delta}$ are based on a hexagonal structure with a space group of $P6_3mc$.

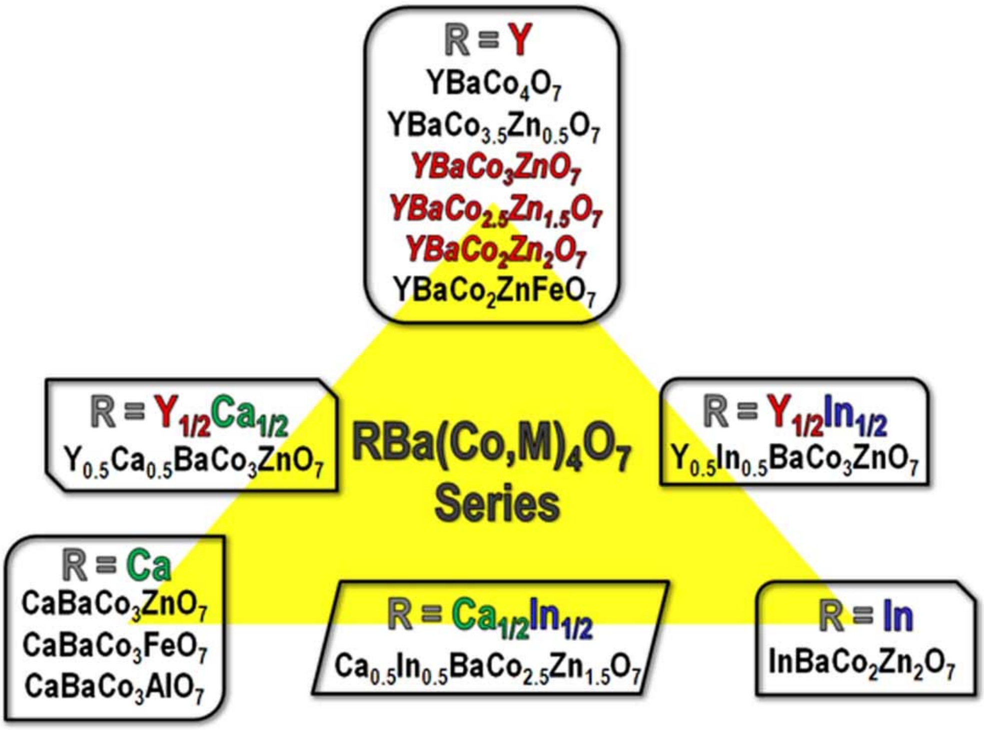

Figure 7.2 Phase diagram indicating the various compositions investigated in the $RBaCo_{4-x}M_xO_7$ series.

samples. As seen, the zinc-free $YBaCo_4O_7$ shows severe decomposition after heating at 800 °C for 12 h, and no reflections corresponding to the $YBaCo_4O_7$ phase could be detected after heating at 700 °C for 52 h (top two segments of Figure 7.4 (a)). The substitution of a small amount of Zn (x = 0.5) significantly improves the stability as indicated by the XRD pattern recorded after heating at 800 °C for 52 h, although the x = 0.5 sample also shows severe decomposition after heating at 700 °C for 52 h (bottom two segments of Figure 7.4 (a)). However, further increase in Zn content to

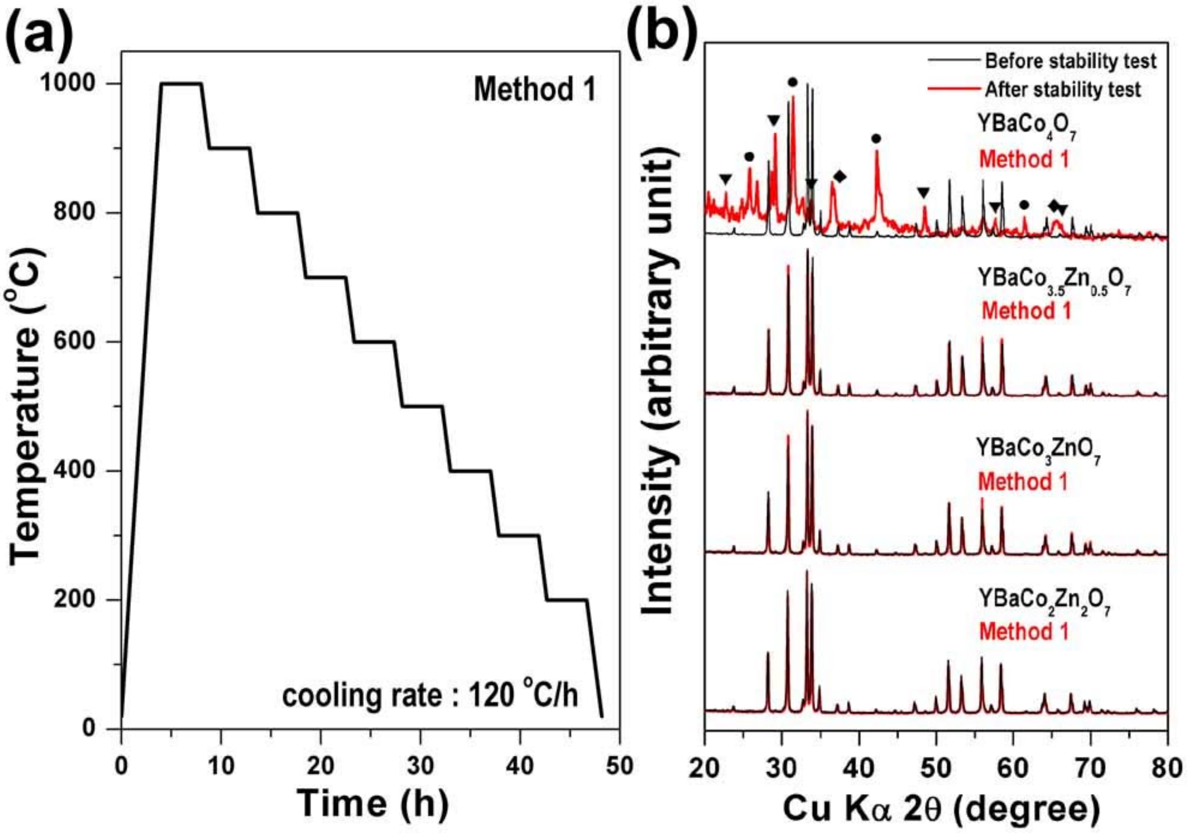

Figure 7.3 (a) Temperature *vs*. time schedule for the temperature-programmed phase stability test (method 1) of the $RBaCo_{4-x}M_xO_7$ powders. (b) XRD patterns illustrating the stabilities of various $YBaCo_{4-x}Zn_xO_7$ compositions: before (black line) and after (red line) high temperature phase stability test using the method 1. While the unmarked reflections belong to the pristine $RBaCo_{4-x}M_xO_7$ phase, those marked with ●, ◆, and ▼ belong, respectively, to $BaCoO_{3-\delta}$, Co_3O_4, and Y_2O_3.

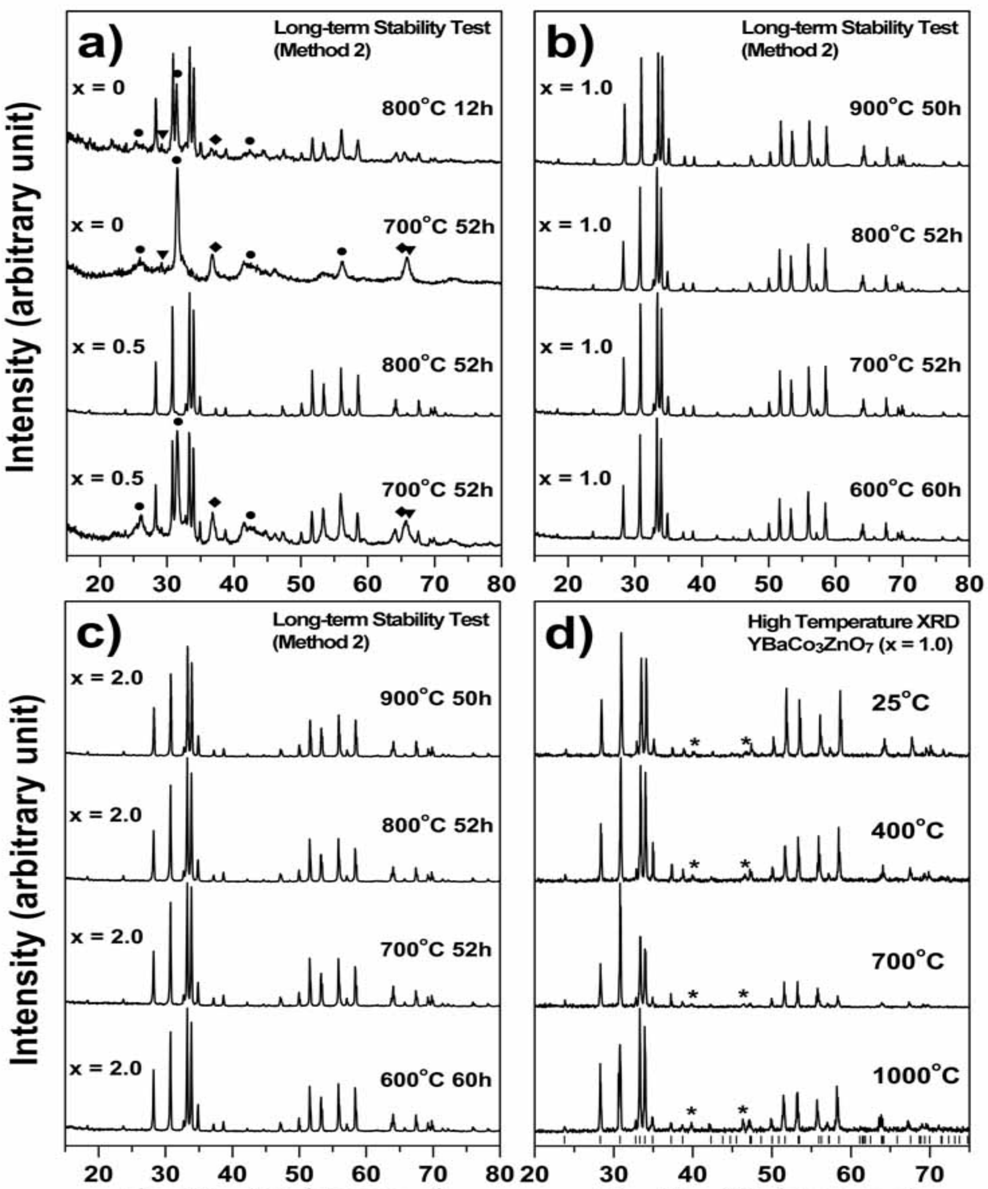

Figure 7.4 Long-term phase stability tests of $YBaCo_{4-x}Zn_xO_7$, assessed by heating the sample powders at 600, 700, 800, or 900 ^{o}C for > 50 h, followed by quenching to room temperature and recording the XRD patterns: (a) x = 0 and 0.5, (b) x = 1.0, and (c) x = 2.0 samples. While the unmarked reflections belong to the $YBaCo_{4-x}Zn_xO_7$ phase, those marked with ●, ◆, ▼, and * belong, respectively, to $BaCoO_{3-\delta}$, Co_3O_4, Y_2O_3, and Pt-Rh (from the sample stage).

$1.0 \leq x \leq 2.0$ completely eliminates the phase decomposition as demonstrated by the long-term stability tests at 600, 700, 800, and 900 ^{o}C (Figures 7.4 (b) and (c)). The x = 1.5 sample (not shown here) also does not show any phase decomposition after the long-term stability tests. The phase stability of the $YBaCo_3ZnO_7$ (x = 1.0 sample) was also carefully examined by high temperature XRD at temperatures up to 1000 ^{o}C (method 3). Figure 7.4 (d) shows the high temperature XRD patterns of the $YBaCo_3ZnO_7$ sample recorded at 400, 700, and 1000 ^{o}C after dwelling for 4 h at each temperature. All the results of methods 1-3 show that the substitution of Zn for Co with $1.0 \leq x \leq 2.0$ in $YBaCo_{4-x}Zn_xO_7$ completely eliminates the phase decomposition.

It has been reported that $YBaCo_{4-x}Fe_xO_7$ ($0 \leq x \leq 0.8$) decomposes severely at high temperatures.[128] With an aim to stabilize $YBaCo_{4-x}Fe_xO_7$, we also investigated the substitution of Zn for Co in $YBaCo_{4-x}Fe_xO_7$, but the resulting $YBaCo_2ZnFeO_7$ composition also show decomposition after heating at 800 ^{o}C for 52 h (Figure 7.5 (a)). In addition, substituition of Zn, Fe, or Al for Co in the $CaBaCo_3MO_7$ system failed to suppress the phase decomposition at high temperatures (Figure 7.5 (a)). However, the M = Zn sample in this system showed only a moderate decomposition compared to the severe decomposition of the M = Al and Fe samples. The $InBaCo_2Zn_2O_7$ sample also showed decomposition (Figure 7.5 (b)).

Our results show that the phase stability of the $RBaCo_{4-x}M_xO_7$ system is strongly influenced by both the R and M elements. For example, Zn substitution ($1 \leq x \leq 2$) is able to suppress the phase decomposition only in the R = Y system, but not

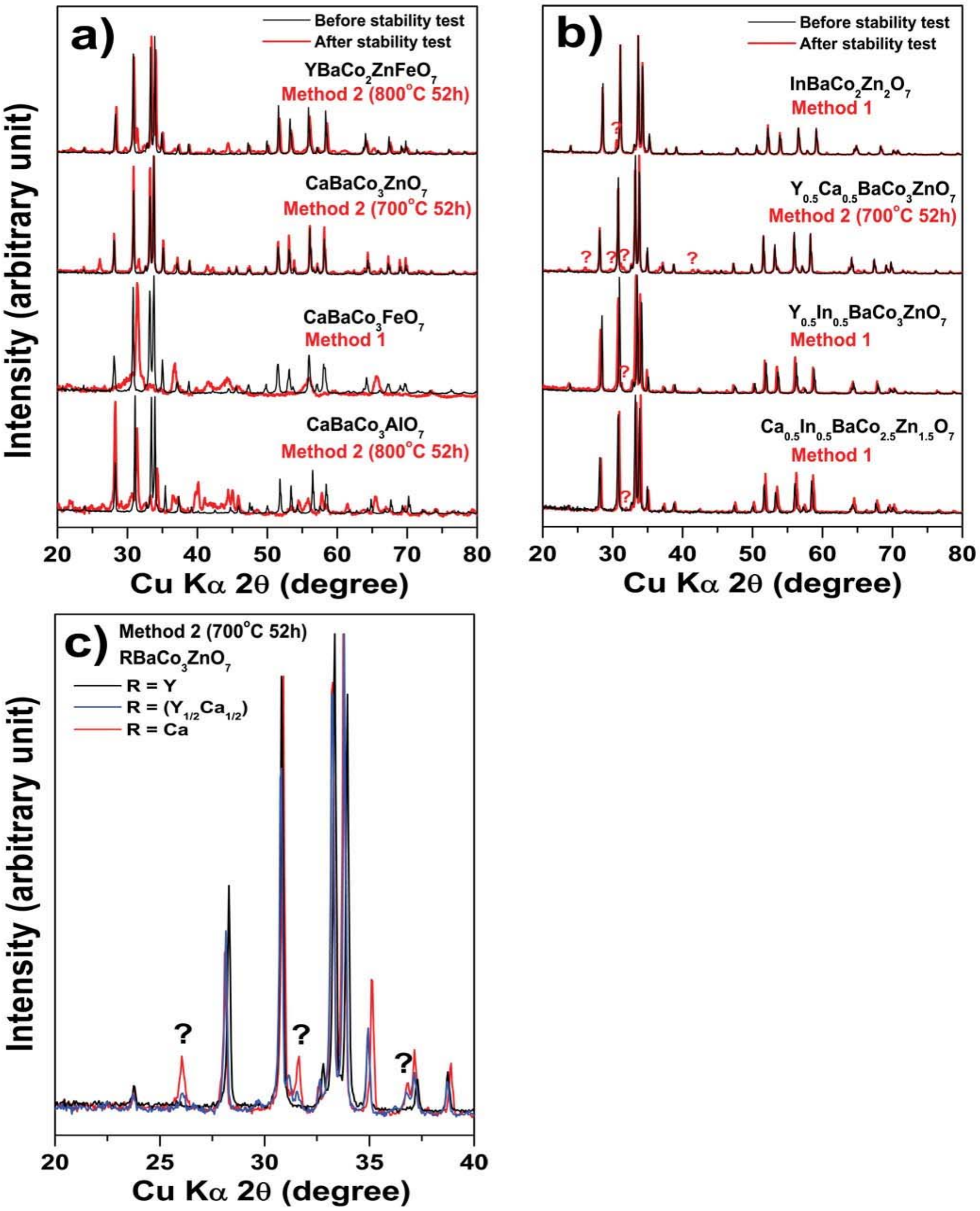

Figure 7 .5 XRD patterns illustrating the stabilities of various RBaCo$_{4-x}$M$_x$O$_7$ compositions: before (black line) and after (red line) high temperature phase stability test using the methods 1 and 2. See the text and experimental section for the details of methods 1 and 2. While the unmarked reflections belong to the pristine RBaCo$_{4-x}$M$_x$O$_7$ phase, those marked with ●, ◆, ▼, and ? belong, respectively, to BaCoO$_{3-\delta}$, Co$_3$O$_4$, Y$_2$O$_3$, and unknown phases.

in the R = Ca and In systems (Figures 7.5 (a) and (b)). To find the effect of R element on the phase stability of the RBa(Co,Zn)O_7 system, we designed new compositions with mixed R = $Y_{0.5}Ca_{0.5}$, $Y_{0.5}In_{0.5}$, and In $_{0.5}Ca_{0.5}$ (Figure 7.5 (b)). Although these samples still have decomposition problems, they show less amount of decomposition compared to the simple R = Ca or R = In samples. For example, Figure 7.5 (c) reveals that the R = ($Y_{1/2}Ca_{1/2}$) sample shows less amount of decomposition compared to the R = Ca sample in $RBaCo_3ZnO_7$ after the long-term stability test at 700 °C. Among the various $RBaCo_{4-x}M_xO_7$ compositions indicated in Figure 7.2, $YBaCo_{4-x}Zn_xO_7$ ($1 \leq x \leq 2$) is the only stable composition at high temperatures. The decomposition products ($BaCoO_{3-\delta}$ and Co_3O_4) of the $YBaCo_4O_7$ sample (Figure 7.4 (a)) suggest that the decomposition of $YBaCo_4O_7$ at elevated temperatures may be related to the tendency of cobalt to adopt octahedral coordination since cobalt is present in tetrahedral coordination in $YBaCo_4O_7$ and predominantly in octahedral coordination in both $BaCoO_{3-\delta}$ and Co_3O_4. With a strong tetrahedral-site preference, the partial substitution of Zn^{2+} for $Co^{2+/3+}$ appears to stabilize the $YBaCo_{4-x}Zn_xO_7$ ($x \geq 1$) phase with corner-shared CoO_4 tetrahedra.

7.3.2 Thermal Properties

Thermogravimetric analysis (TGA) of the $YBaCo_{4-x}Zn_xO_7$ (x = 1.0, 1.5, 2.0) was carried out in air for two consecutive heating/cooling cycles. After the first heating cycle, there was a dwelling at ~ 870 °C for 15 h before recording the first cooling curve. Figure 7.6 (a) shows the variations in the actual oxygen content with temperature for the x = 1.0 sample. These curves were derived using the initial room-temperature oxygen-content values determined by the iodometric titration and the TGA data. On heating, the sample first absorbs oxygen at 200-300 ^{o}C and then loses oxygen above 300 ^{o}C, characteristic of an oxygen storage material.[125] Above 400 ^{o}C, the TGA curve shows a plateau with only a slight decrease in weight. The sample then shows a small amount of weight gain during dwelling at ~ 870 ^{o}C for 15 h. The XRD patterns after the TGA cycle (Figure 7.7) as well as the long term stability test (Figure 7.4 (b)) suggest that this weight gain is not due to phase decomposition. The small weight gain at ~ 870 ^{o}C appears to be due to the filling up of the oxygen vacancies formed in $YBaCo_3ZnO_7$ during the rapid cooling (4 ^{o}C/min) process after sintering it at 1200 ^{o}C during the powder synthesis process. The variations of oxygen content (7 + δ) with temperature in the $0.5 \leq x \leq 2.0$ samples are compared in Figure 7.6 (b). These oxygen content values were obtained using the TGA data collected during cooling in Figure 7.6 (a) after dwelling the sample at ~ 870 ^{o}C for 15 h. As seen in Figure 7.6 (b), all the samples have oxygen contents > 7.0 even after dwelling at ~ 870 ^{o}C.

The thermal expansion behaviors of the various $RBaCo_{4-x}M_xO_7$ samples were measured in air. Figure 7.8 compares the thermal expansion curves and the corresponding TEC values of the $RBaCo_{4-x}M_xO_7$ samples recorded at 80 – 900 ^{o}C. Although the $CaBaCo_3ZnO_7$, $CaBaCo_3ZnO_7$, and $Y_{1/2}Ca_{1/2}BaCo_3ZnO_7$ samples show

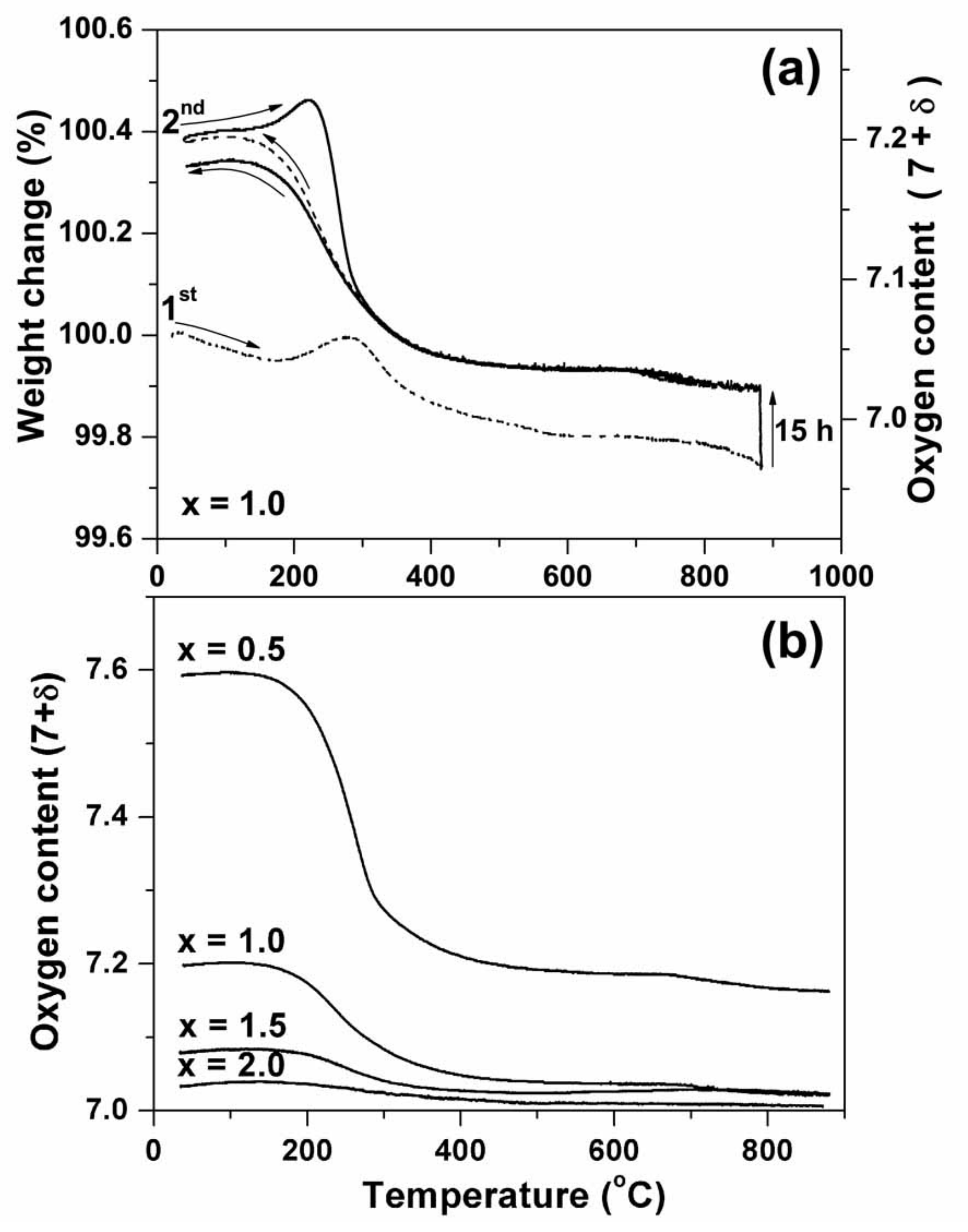

Figure 7.6 (a) Thermogravimetric analysis (TGA) of $YBaCo_3ZnO_7$ in air for two consecutive heating/cooling cycles: dotted line for the 1st cycle and solid line for the 2nd cycle. (b) The variation of oxygen contents (7 + δ) in $YBaCo_{4-x}Zn_xO_{7+\delta}$ ($0.5 \leq x \leq 2.0$) obtained after oxygen compensation at ~ 870 °C for 15 h in air.

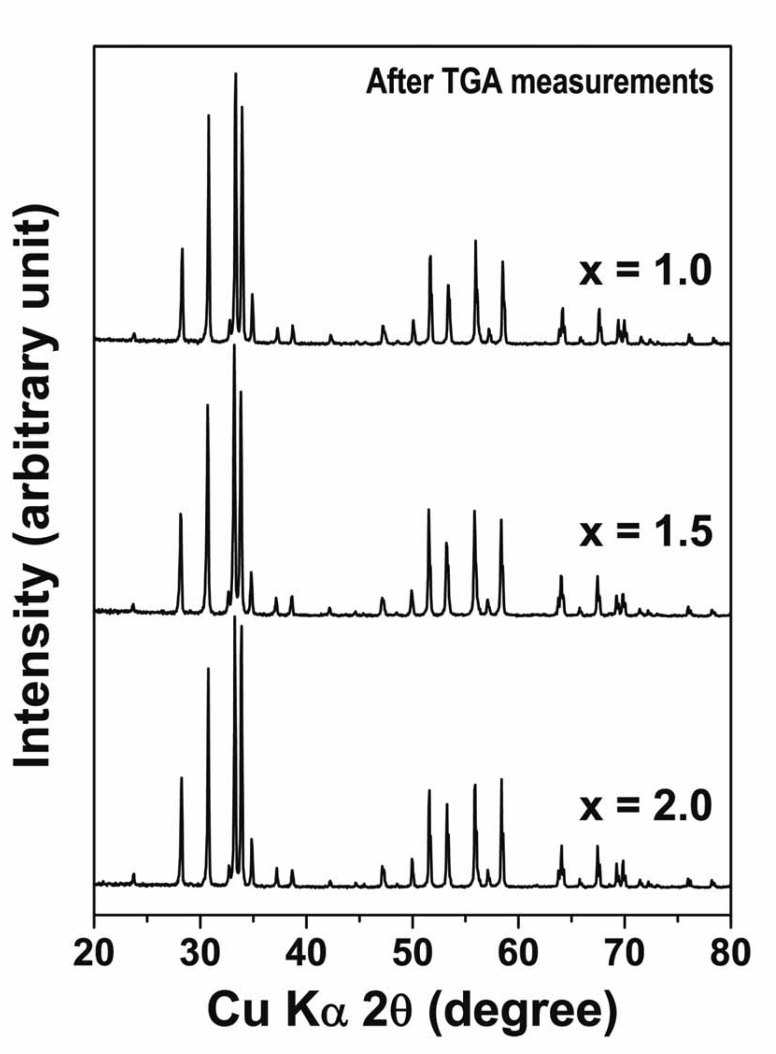

Figure 7.7 XRD patterns of the $YBaCo_{4-x}Zn_xO_7$ ($1.0 \leq x \leq 2.0$) after the TGA cycles in air.

phase decomposition after the long-term phase stability tests by method 2 as seen in Figure 7.5, their decomposition was rather slow considering the absence of any noticeble phase decomposition after the temperature-programmed phase stability measurement by the method 1 (not shown here). Figure 7.8 (a) shows that the thermal expansion curves recorded at 80 – 900 ^{o}C are reversible for these samples. However, the samples that encounter severe decompositions such as $YBaCo_4O_7$ and $YBaCo_2ZnFeO_7$ showed noticeable kinks in the slope with poor reversibility between the thermal expansion curves recorded during heating and cooling (not shown here). The TEC values of the $RBaCo_{4-x}M_xO_7$ specimens in the range of 80 – 900 ^{o}C vary in the ranges of $6 \times 10^{-6} – 13 \times 10^{-6}$ $^{o}C^{-1}$ in Figure 7.8 (b). From the unit cell expansion observed during the high temperature XRD measurements in Figure 7.4 (d), the TEC of $YBaCo_3ZnO_7$ has been determined to be 8.8×10^{-6} $^{o}C^{-1}$ in the range of 20 – 700 ^{o}C, which is slightly less than the value obtained from the dilatometer measurement. These low TEC values provide good thermal expansion compatibility with the standard SOFC electrolyte materials like YSZ, GDC, and LSGM ($10.0 \times 10^{-6} – 12.5 \times 10^{-6}$ $^{o}C^{-1}$). The low TEC can be attributed to the absence of spin state transitions of $Co^{2+/3+}$ ions and much diminished oxygen loss occurring with increasing temperature (Figure 7.6). The $Co^{2+/3+}$ ions with tetrahedral oxygen coordination in $YBaCo_3ZnO_7$ are in high-spin states[127] and do not encounter any spin state transitions with increasing temperature unlike the octahedral-site Co^{3+} ions in perovskite oxides that undergo a low-spin to high-spin transition and an increase in ionic radius with increasing temperature. In addition, unlike cobalt-containing pervoskites, the

$YBaCo_{4-x}Zn_xO_7$ (x = 1.0 and 2.0) samples exhibit nearly linear thermal expansion curves at $T > 400$ (Figure 7.8 (a)) due to the absence of any drastic oxygen loss as seen in the TGA data (Figure 7.6). The negligible oxygen loss also results in low TEC values.

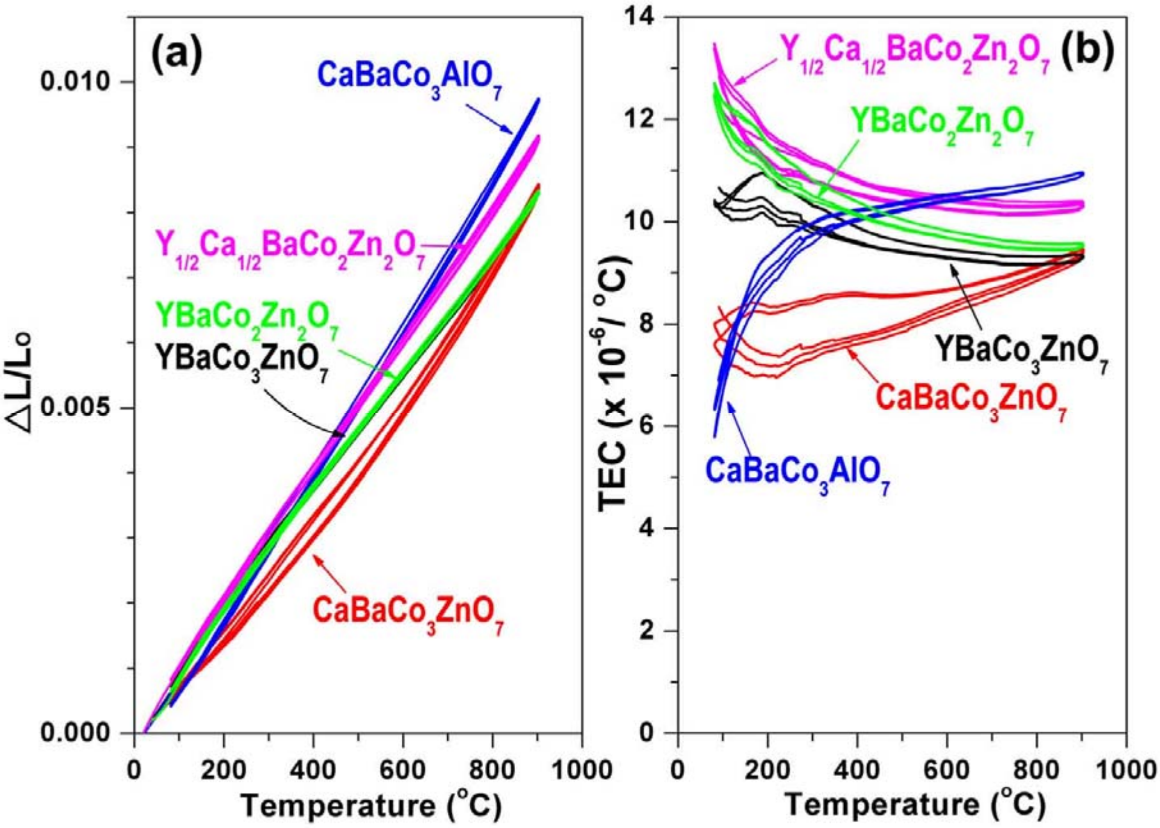

Figure 7 .8 (a) Thermal expansion (dL/L_o) curves and (b) corresponding thermal expansion coefficient (TEC) curves of various $RBaCo_{4-x}M_xO_7$ in the temperature range of 80 – 900 °C in air.

7.3.3 Oxygen Permeation Properties

The oxygen permeation flux (jO_2) data in Figure 7.9 (a) reveal that a dense $YBaCo_3ZnO_7$ pellet exhibits an oxygen flux of ~ 10^{-10} mol cm^{-2} s^{-1} at 700 – 900 °C, which is 3 – 4 orders of magnitude lower than that found with the cobalt-based perovskite oxides such as $SrCo_{0.8}Fe_{0.2}O_{3-\delta}$[12] and $La_{0.6}Sr_{0.4}CoO_{3-\delta}$[131] with similar thicknesses. However, whether the oxygen permeability in $YBaCo_3ZnO_7$ is determined by bulk oxygen diffusion or surface exchange rate remain to be established with future experiments. The $YBaCo_4O_{7+\delta}$ samples are known to accomodate large amount of excess oxygen ($\delta \approx 1.0$ in air) at 200 °C $\leq T \leq$ 400 °C, indicating the presence of a significant amount of oxygen in the interstitial sites within the lattice.[125] Although the amount of the excess oxygen (δ) sharply decreases at T > 400 °C, our TGA data in Figure 7.6 reveal that the $YBaCo_{4-x}Zn_xO_{7+\delta}$ samples still have excess oxygen ($\delta > 0$) at high temperatures. Therefore, one can conclude that the oxygen migration occurs via an interstitial mechanism within the $YBaCo_3ZnO_7$ lattice at 700 – 900 °C. However, further study is necessary to fully understand the oxygen transport mechanism in the $YBaCo_{4-x}Zn_xO_{7+\delta}$ samples.

It is interesting that the dense $YBaCo_3ZnO_7$ specimen maintains its original shape without any noticeable surface crack after the oxygen permeation measurements (Figure 7.9 (b)). In contrast, cobalt-based perovskite or perovskite-related materials tend to show surface cracks or even specimen breakage on cooling due to mechanical stresses caused by the large thermal expansion mismatch with the other components like the glass-ring and alumina tube that have TECs of, respectively, ~ 3.2×10^{-6} and ~ 7.6×10^{-6} $^{o}C^{-1}$.[132] For example the $La_{0.5}Ba_{0.5}CoO_{3-\delta}$ perovskite oxide that has a TEC of 24.3×10^{-6} $^{o}C^{-1}$ in the temperature range of 80 – 900 ^{o}C shows severe crack after the oxygen permeation test (Figure 7.9 (c)). Thus, the low TEC of $YBaCo_3ZnO_7$ can provide the important advantage of good mechanical integrity as an oxygen permeation membrane. In addition, Figure 7.9(d) shows the XRD pattern of the $YBaCo_3ZnO_7$ sample after performing the oxygen permeation experiments in the temperature range of 700 – 900 ^{o}C for an extended period of > 360 h. This result again proves the long-term phase stability of the $YBaCo_3ZnO_7$ sample at high temperatures.

$RBaCo_4O_{7+\delta}$ (R = Y, Dy, Ho, Er, Tm, Yb, and Lu) oxides have been studied intensively due to their high oxygen-storage capacity at $T < 450$ ^{o}C.[125,129,133,134] More importantly, recent reports have shown change in the crystal structure after large amount of oxygen uptake ($1.0 \leq \delta \leq 1.5$) within the lattice.[133,135] However, even the oxygen-rich $RBaCo_4O_{7+\delta}$ samples with $1.0 \leq \delta \leq 1.5$ lose oxygen on heating and their oxygen content values become close to 7 ($\delta = 0$) at $T > 500$ ^{o}C. Additionally, with the stoichiometric amount of oxygen ($\delta \approx 0$) on heating to 1000 ^{o}C, the $YBaCo_3ZnO_7$ sample exhibits the hexagonal structure with the space group of $P6_3mc$. Therefore, the location of oxide ions and their transport mechanism within the $RBaCo_{4-x}M_xO_7$ lattice during the SOFC operation at high temperatures ($T > 500$ ^{o}C) will be different from that of the lower temperature oxygen storage behavior ($T < 450$ °C), and it needs to be studied further.

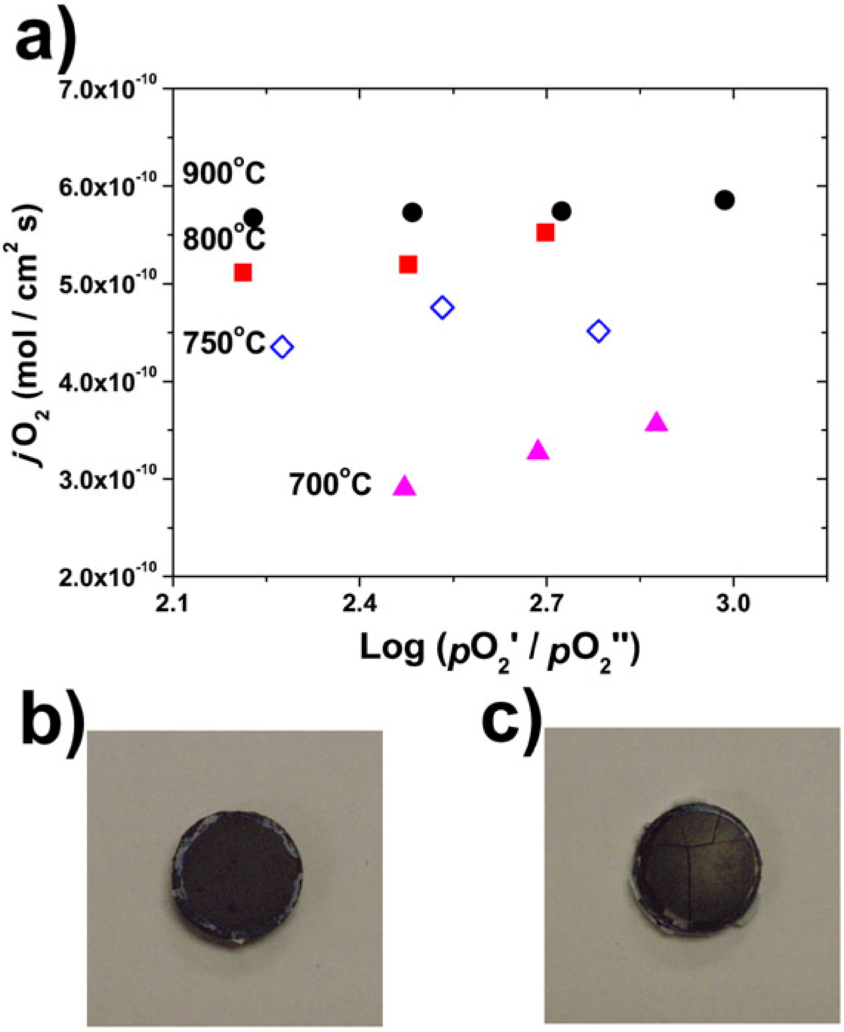

Figure 7.9 (a) Variations of the oxygen permeation flux of $YBaCo_3ZnO_7$ with Log (pO_2'/pO_2'') at different temperatures. Photographs of the (b) $YBaCo_3ZnO_7$ and (c) $La_{0.5}Ba_{0.5}CoO_{3-z}$ pellets after the oxygen permeation experiments. Trace amount of glass sealant (white color) remains in the edge of each pellet.

7.3.4 El ectrochemical Properties

Figure 7.10 shows the temperature dependence of the electrical conductivity of the $YBaCo_{4-x}Zn_xO_7$ ($1.0 \leq x \leq 2.0$) samples on heating (closed symbols) and cooling. The conductivity increases with temperature for all the samples, indicating a thermally-activated polaron behavior. At a given temperature, the electrical conductivity decreases with increasing Zn content. The activation energy calculated from the Arrhenius plots also increases from 0.172 eV ($x = 0$) to 0.193 eV ($x = 1.5$) to 0.226 eV ($x = 2.0$) with Zn content. The decrease in conductivity is due to the perturbation of the electron hopping pathway by the Zn^{2+} ions having a completely filled 3d orbital.

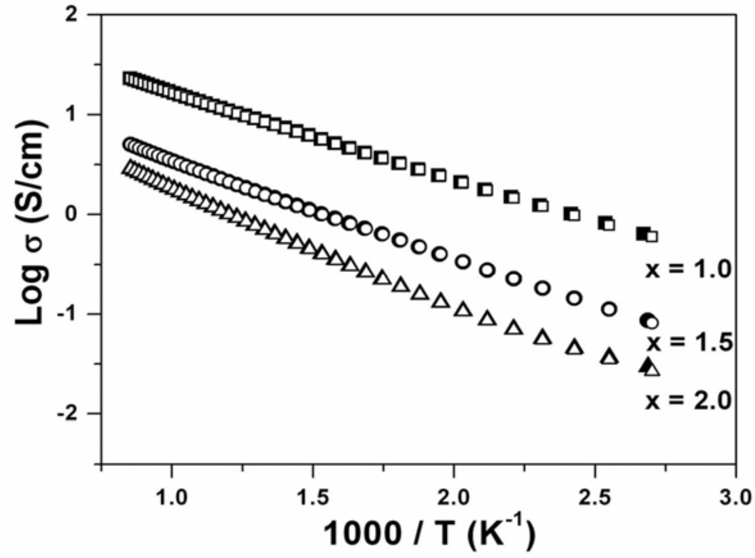

Figure 7.10 Temperature dependence of the electrical conductivity of the $YBaCo_{4-x}Zn_xO_7$ ($1.0 \leq x \leq 2.0$) samples on heating (closed symbols) and cooling (open symbols).

The chemical stability of the $YBaCo_{4-x}Zn_xO_7$ (x ≥ 1) powder in contact with the electrolyte is critical for use as a cathode in SOFC. Accordingly, the $YBaCo_{4-x}Zn_xO_7$ (x ≥ 1) powder was heated at 1000 °C for 3 h or 1100 °C for 2 h with YSZ, LSGM, and GDC electrolyte powders and examined by XRD. The data in Figure 7.11 reveal that $YBaCo_{4-x}Zn_xO_7$ with x ≥ 1 is stable in contact with the GDC electrolyte after heating at 1100 °C for 2 h, while it reacts with YSZ and LSGM on heating at 1000 °C for 3 h (not shown here). However, the $YBaCo_{4-x}Zn_xO_7$ (x ≥ 1) cathode could be used with the YSZ and LSGM electrolytes by applying a GDC buffer layer between the cathode and the electrolyte.

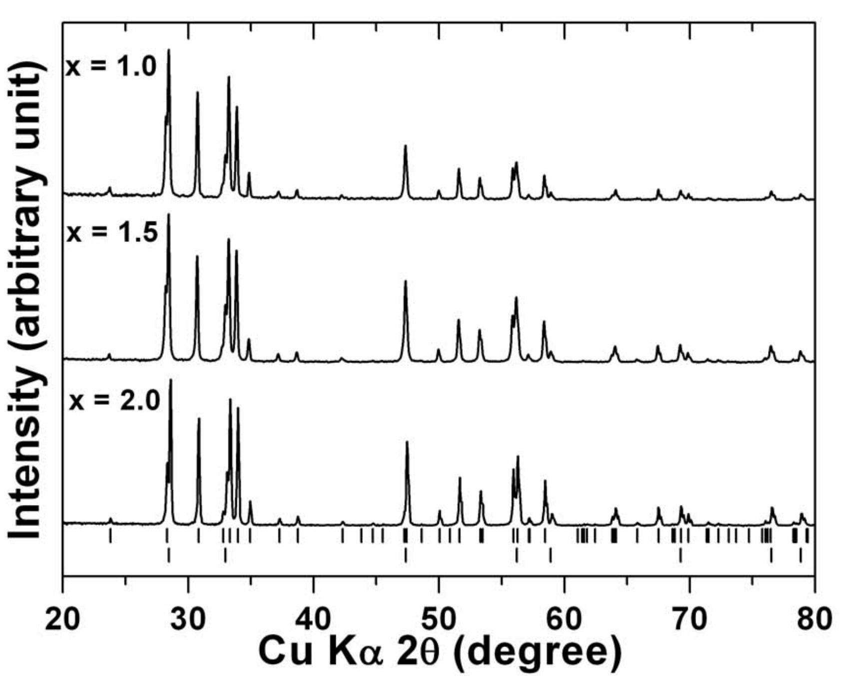

Figure 7.11 XRD patterns of the $YBaCo_{4-x}Zn_xO_7$ ($1.0 \le x \le 2.0$) + GDC mixture after heating at 1100 °C for 2 h. The vertical lines at the bottom indicate the calculated peak positions of the x = 2.0 (upper) and GDC (lower) samples.

The cathode polarization resistance (R_p) of $YBaCo_3ZnO_7$ was measured using symmetrical cells with two different cell configurations: $YBaCo_3ZnO_7$ | GDC | $YBaCo_3ZnO_7$ configuration with a simple $YBaCo_3ZnO_7$ cathode and $YBaCo_3ZnO_7$ | $YBaCo_3ZnO_7$+GDC | GDC | $YBaCo_3ZnO_7$+ GDC | $YBaCo_3ZnO_7$ configuration with a $YBaCo_3ZnO_7$ + GDC (1:1 wt. ratio) composite layer between the $YBaCo_3ZnO_7$ cathode and GDC electrolyte. Figure 7.12 compares the R_p values of these two symmetrical cells with that of the $La_{0.6}Sr_{0.4}Co_{0.2}Fe_{0.8}O_3$ (LSCF) cathode and the literature data for $La_{0.5}Sr_{0.5}CoO_3$ (LSC).[136] The R_p value of the $La_{0.6}Sr_{0.4}Co_{0.2}Fe_{0.8}O_3$ (LSCF) cathode prepared by a combustion method was measued with the same cell configuration, and its R_p value in Figure 7.12 is within the range of values reported in the literature by various groups.[44,96,136] It is noteworthy that both the simple $YBaCo_3ZnO_7$ (E_a = 0.82 eV) and $YBaCo_3ZnO_7$ + GDC composite cathodes (E_a = 0.94 eV) show lower activation energy (E_a) than simple LSCF (E_a = 1.01 eV for $T \geq 600$ °C and E_a = 1.77 eV for $T \leq 600$ °C) or LSC (E_a = 1.11 eV) cathodes in the temperature range of 500 – 800 °C. The cell with the simple $YBaCo_3ZnO_7$ cathode shows R_p values of 0.40 Ω cm^2 at 600 °C and 0.15 Ω cm^2 at 700 °C, which are lower than the R_p value for LSCF at $T \leq 700$ °C. After applying the composite layer, the R_p value decreases to 0.22 Ω cm^2 at 600 °C and 0.06 Ω cm^2 at 700 °C, which are approximately two times lower than that observed with the simple $YBaCo_3ZnO_7$ cathode. Our oxygen permeation measurements show that the oxygen transport in dense $YBaCo_3ZnO_7$ membrane is slow compared to that found with other cobalt-based perovskite oxides (Figure 7.9 (a)). Therefore, the

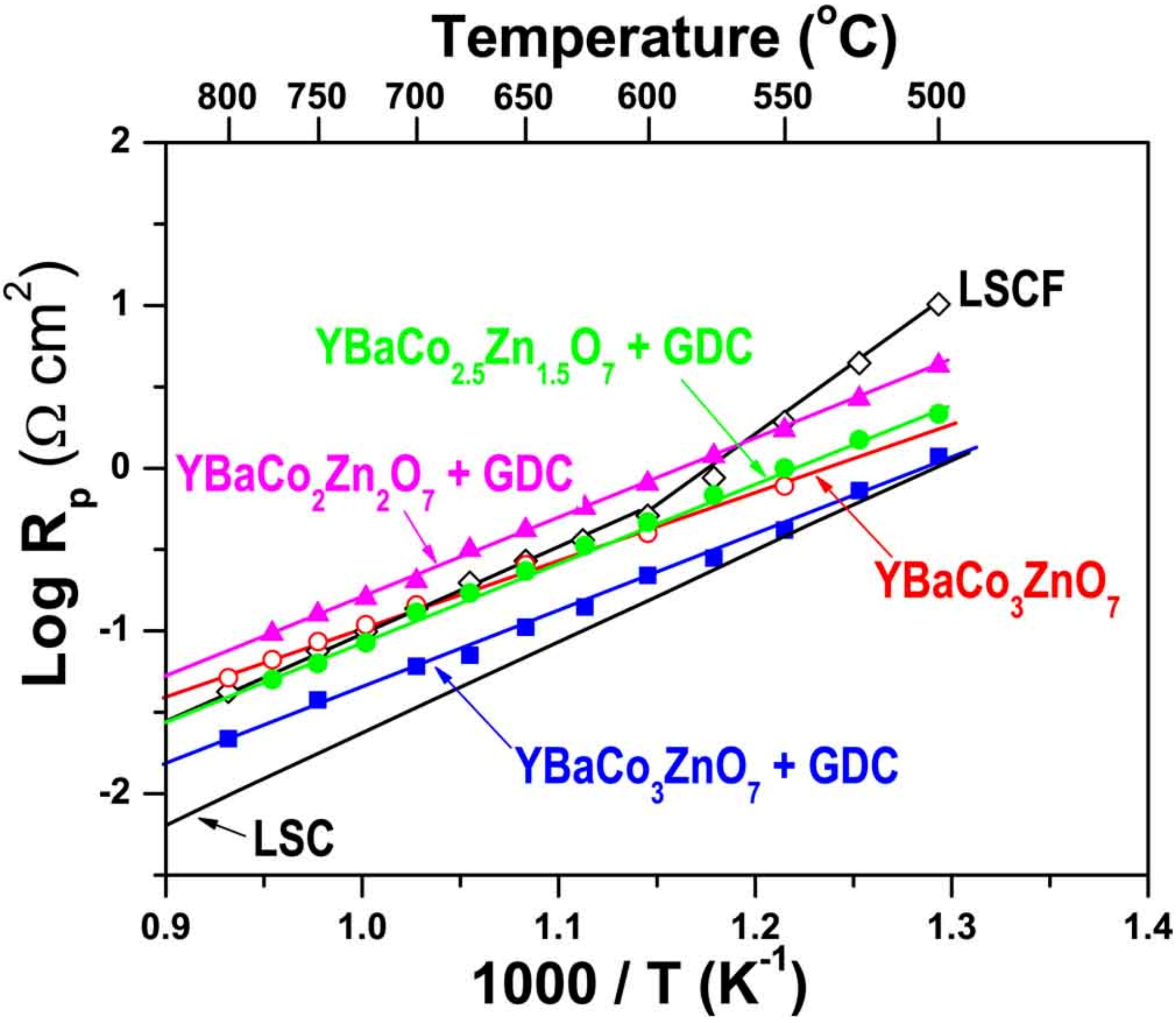

Figure 7 .12 Variations of the cathode polarization resistances (R_p) of the simple $YBaCo_3ZnO_7$, $YBaCo_{4-x}Zn_xO_7$ ($1.0 \leq x \leq 2.0$) + GDC composite, $La_{0.6}Sr_{0.4}Co_{0.2}Fe_{0.8}O_3$ (LSCF), and $La_{0.5}Sr_{0.5}CoO_3$ (LSC, literature data[136]) cathodes with temperature.

decrease in the polarization resistance of the $YBaCo_3ZnO_7$ + GDC composite cathode is due to the expanded reaction area on mixing the oxide ion conductor with $YBaCo_3ZnO_7$. More importantly, the R_p of the $YBaCo_3ZnO_7$ + GDC composite cathode becomes close to that of the LSC cathode at around 500 ^oC, exemplifying its potential for oxygen-reduction reaction at low temperatures. However, the R_p values of the $YBaCo_{4-x}Zn_xO_7$ + GDC composite cathodes increase with further increase in Zn content (x = 1.5 and 2.0) at a given temperature. For example, R_p increases from 0.219 (x = 1.0) to 0.464 (x = 1.5) to 0.802 (x = 2.0) at 600 ^oC. The activation energies of the cathodes were calculated to be 0.94 – 0.97 eV for $1.0 \leq x \leq 2.0$ in the temperature range of 500 – 800 ^oC from the Arrhenius plots in Figure 7.12.

The performances of the simple $YBaCo_3ZnO_7$, $YBaCo_3ZnO_7$ + GDC composite, and LSCF cathodes for the oxygen reduction reaction in SOFC were evaluated with LSGM (0.5 mm thick) electrolyte-supported single cells. Although the thick electrolyte hinders us from obtaining the optimum fuel cell performance due to the high electrolyte ohmic drop, it has been useful to compare the relative fuel cell performances of the various electrode materials.[82,114,137] Figures 7.13 (a) – (c) show the current-voltage (*I-V*) curves, the corresponding power density curves, and the cathode over-potential curves obtained at 800 ^oC. The maximum power density (P_{max}) obtained with the simple $YBaCo_3ZnO_7$ cathode (P_{max} = 270 mW cm^{-2}) is slightly lower than that obtained with the simple LSCF cathode (P_{max} = 290 mW cm^{-2}) at 800 ^oC. However, the $YBaCo_3ZnO_7$ + GDC composite cathode shows superior

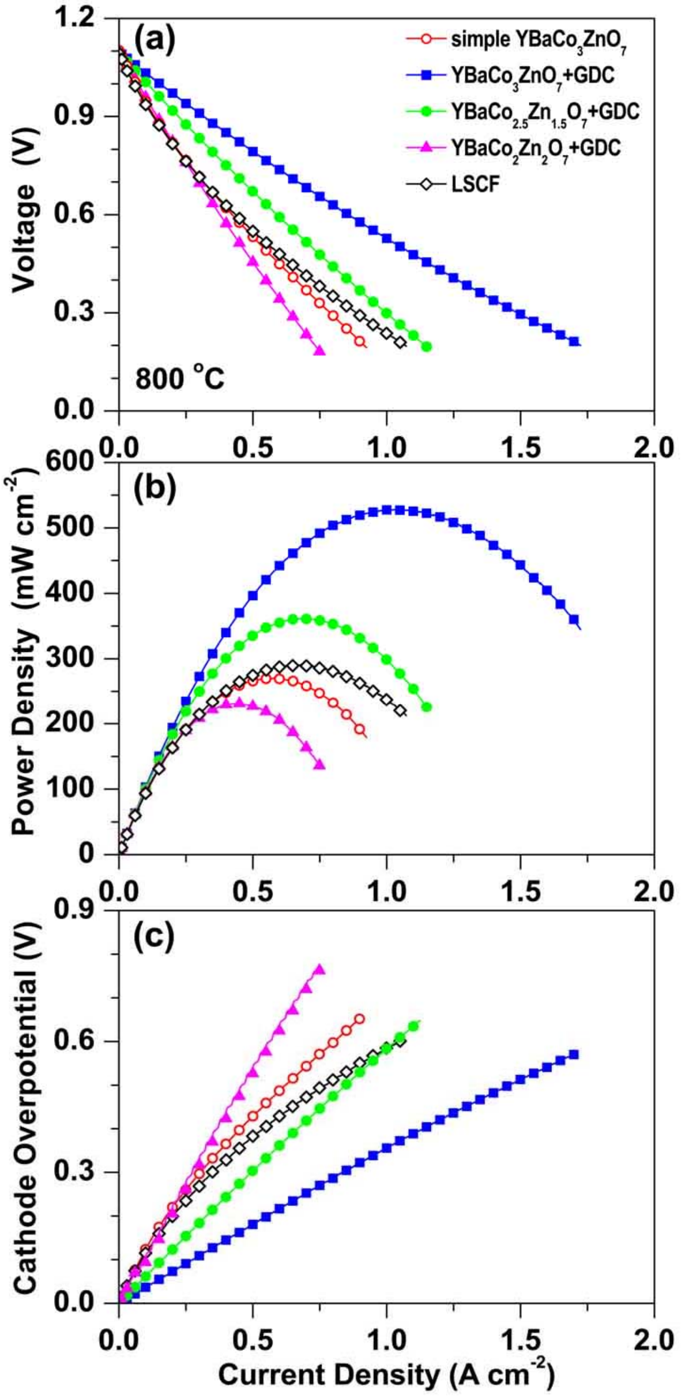

Figure 7. 13 Single cell SOFC performance data of the simple YBaCo$_3$ZnO$_7$, YBaCo$_{4-x}$Zn$_x$O$_7$ ($1.0 \leq x \leq 2.0$) + GDC composite, and La$_{0.6}$Sr$_{0.4}$Co$_{0.2}$Fe$_{0.8}$O$_3$ (LSCF) cathodes at 800 °C: (a) The current-voltage (*I*-*V*) curves, (b) corresponding power density curves, and (c) cathode over-potential curves.

performance compared to the simple $YBaCo_3ZnO_7$ or LSCF cathodes with P_{max} values of 528 mW cm^{-2}, which is consistent with its low R_p and cathode over-potential values. These P_{max} values are comparable to those obtained with the layered $Ln(Ba,Sr)(Co,Ni)_2O_{5+\delta}$ perovskite cathodes using similar single cell configurations in Chapters 3-6. The single cell performance of the $YBaCo_{4-x}Zn_xO_7$ + GDC composite cathode decreases with further increase in Zn content (x = 1.5 and 2.0) due to the decreasing electrical conductivity (Figure 7.10) and increasing R_p (Figure 7.12) and over-potential (Figure 7.13 (c)). These results suggest that the $YBaCo_3ZnO_7$ + GDC composite will be an attractive cathode for SOFC.

Figure 7.14 shows the microstructure of the cathode-electrolyte portion after the single cell SOFC performance tests. While the bottom portion of the micrographs indicate the dense, sintered LSGM electrolyte, the upper portion shows the GDC buffer layer with a thickness of $\leq$ 10 μm and the porous cathode + GDC composite or cathode layer. The simple $YBaCo_3ZnO_7$ or LSCF cathodes have thicknesses of ~ 40 μm while the $YBaCo_{4-x}Zn_xO_7$ ($1.0 \leq x \leq 2.0$) + GDC composite cathodes have thickness of ~ 50 μm.

On employing $YBaCo_3ZnO_7$ + GDC composite as a cathode in SOFC, $YBaCo_3ZnO_7$ exhibits performance comparable to that of well-studied Co-based perovskite cathodes, but with the critical advantage of an ideal matching of the TEC value with those of standard electrolytes and consequent long-term mechanical integrity without the development of cracks. The performance of the $YBaCo_{4-x}Zn_xO_7$

+ GDC composite cathodes decreases with further increase in Zn content (x = 1.5 and 2.0) due to decreasing electrical conductivity, increasing polarization resistance, and increasing over-potential while the microstructures remain similar, demonstrating that $YBaCo_3ZnO_7$ is the optimum composition. Further enhancement in the cathode performance could be achieved by optimizing the ratio between $YBaCo_3ZnO_7$ and GDC in the composite layer, increasing the surface area of $YBaCo_3ZnO_7$ by solution-based chemical synthesis methods, and employing anode-supported cells with thinner electrolytes. Cells with thin electrolytes are anticipated to offer good performance at lower temperatures (~ 500 ^{o}C) due to the low E_a values.

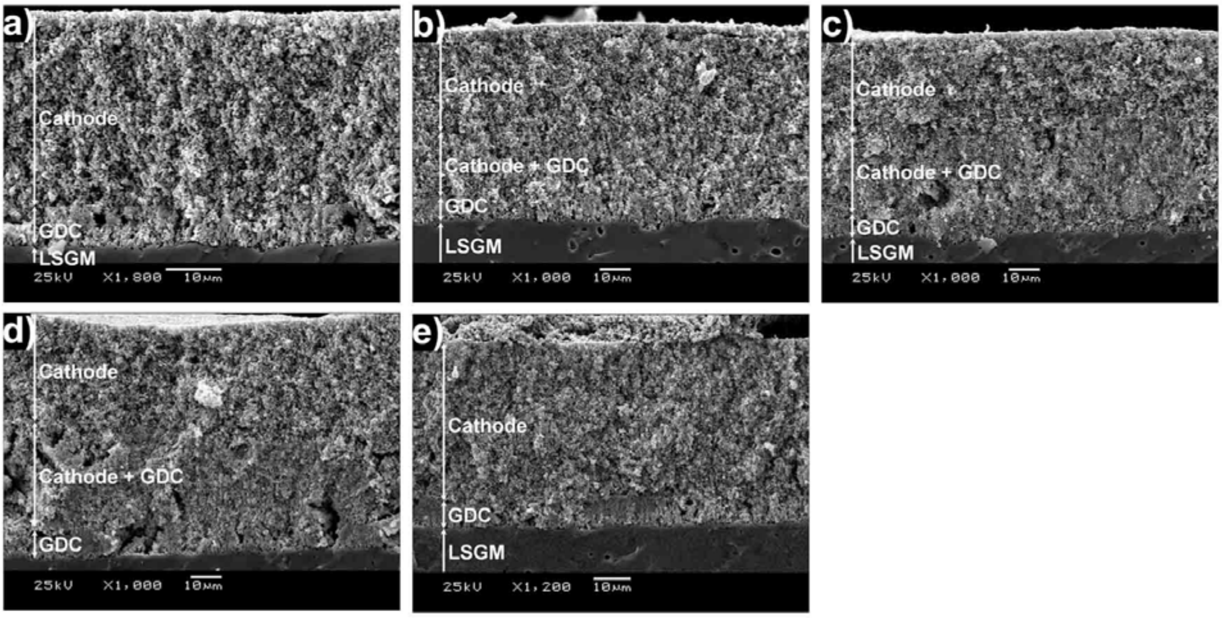

Figure 7.14 Scanning electron microscope images showing the cross section of the cathode-electrolyte portion: (a) simple $YBaCo_3ZnO_7$, (b) $YBaCo_3ZnO_7$ + GDC composite, (c) $YBaCo_{2.5}Zn_{1.5}O_7$ + GDC composite, (d) $YBaCo_2Zn_2O_7$ + GDC composite, and (e) simple $La_{0.6}Sr_{0.4}Co_{0.2}Fe_{0.8}O_3$ cathodes after the SOFC performance tests.

7.4 CONCLUSIONS

A new class of cathode materials $RBa(Co,M)_4O_7$ (R = Y, Ca, In and M = Zn, Fe, Al) based on tetrahedral-site $Co^{2+/3+}$ ions exhibiting a unique combination of high catalytic activity and low TEC have been investigated as cathode materials for SOFC. High temperature phase stability tests in various temperature regions show that $YBaCo_{4-x}Zn_xO_7$ ($1 \leq x \leq 2$) is the only stable composition among the various $RBaCo_{4-x}M_xO_7$ compositions investigated. The $RBaCo_{4-x}M_xO_7$ samples exhibit low TEC values of $6 \times 10^{-6} – 13 \times 10^{-6}$ $^{o}C^{-1}$ in the range of 80 – 900 ^{o}C, providing good thermal expansion compatibility with the standard SOFC electrolyte materials like YSZ, GDC, and LSGM. Although the oxygen permeation flux of the $YBaCo_3ZnO_7$ specimen is 3 – 4 orders of magnitude lower than that found with the cobalt-based perovskite oxides, such low oxygen conduction is overcome by employing $YBaCo_3ZnO_7$ + GDC composites as cathodes in SOFC. With a low cathode polarization resistance and over-potential, the $YBaCo_3ZnO_7$ + GDC composite cathodes exhibit fuel cell performance comparable to that of well-studied Co-based perovskite cathodes, but with the critical advantage of an ideal matching of the TEC value with those of standard electrolytes.

CHAPTER 8

Summary

With an aim to design and develop alternative cathode materials for intermediate temperature SOFCs, the $LnBaCo_2O_{5+\delta}$ (Ln = La, Nd, Sm, Gd, and Y) and $Ln(Ba,Sr)(Co,Ni)_2O_{5+\delta}$ layered perovskite oxides and a new series of non-pervoskite oxides $RBa(Co,M)_4O_7$ (R = Y, Ca, In, M = Zn, Fe, Al) having a hexagonal structure have been investigated.

A systematic investigation of a correlation of the electrochemical performances to the lanthanide host cations in $LnBaCo_2O_{5+\delta}$ (Ln = La, Nd, Sm, Gd, and Y) layered perovskite oxides has been carried out. The room-temperature oxygen content decreases from 6.0 to 5.41 from Ln = La to Y due to a decrease in the size of the Ln^{3+} ions and the consequent preference for lower coordination numbers. Although the increasing oxygen vacancy concentration and bending of the O–Co–O bonds lead to a decrease in electrical conductivity with decreasing size of the Ln^{3+} ions, the smaller lanthanide ions provide an important advantage of lowering the thermal expansion due to a decreasing ionicity of the Ln–O bonds. The $LnBaCo_2O_{5+\delta}$ (Ln = Pr, Nd, and Sm) oxides exhibit metal-insulator transitions at $T < 200$ °C and oxygen vacancy order-disorder transitions accompanied by a transition from orthorhombic to tetragonal structure at $T > 350$ °C. At a given temperature, the oxygen permeation flux jO_2 through the $LnBaCo_2O_{5+\delta}$ membranes decreases from La to Nd to Sm due to a lowering of the crystal symmetry and lattice strain. A linear dependence of jO_2 with the reciprocal of membrane thickness ($1/L$) and its extrapolation to the origin in the Ln = Nd sample reveal that the oxygen transport mechanism is bulk diffusion limited. The oxide ion conductivity values calculated using the Wagner's equation decrease with decreasing size of the Ln^{3+} ions from Ln = La to Nd to Sm. The power density of single-cell SOFCs fabricated with the $LnBaCo_2O_{5+\delta}$ cathodes decreases with the decreasing size of the Ln^{3+} ions due to the decreasing oxygen diffusion rate and electrical conductivity. The $LnBaCo_2O_{5+\delta}$ cathodes with an intermediate-size lanthanide ion like Sm^{3+} may provide a trade-off between TEC and catalytic activity.

With the $GdBa_{1-x}Sr_xCo_2O_{5+\delta}$ system, the Sr substitution for Ba affects the crystal chemistry, thermal expansion behavior, electrical conductivity, chemical compatibility, and electrochemical performance. The $GdBa_{1-x}Sr_xCo_2O_{5+\delta}$ system exhibits a structural change from orthorhombic (x = 0) to tetragonal (x = 0.2 – 0.6) to orthorhombic (x = 1.0) with changes in space groups and an increase in oxygen content ($5+\delta$) with increasing Sr content. While the TEC decreases with increasing Sr content in the low temperature region (80 – 300 ^{o}C), it increases with Sr content in the high temperature region (300 – 900 ^{o}C). The $GdBa_{1-x}Sr_xCo_2O_{5+\delta}$ samples exhibit a metal to insulator (M-I) transition around 200 ^{o}C and the transition becomes less pronounced with increasing Sr content. At a given temperature, the electrical conductivity increases with increasing Sr content due to increasing oxygen content.

While the Sr-free $GdBaCo_2O_{5+\delta}$ sample suffers from interfacial reaction with LSGM and GDC electrolytes at 1100 ^{o}C, Sr substitution for Ba improves the chemical stability of $GdBa_{1-x}Sr_xCo_2O_{5+\delta}$ with better cathode performance for $x = 0.2$ and 0.6.

With an aim to decrease the TEC further, the substitution of Ni for Co in $NdBaCo_{2-x}Ni_xO_{5+\delta}$ ($0 \leq x \leq 0.6$) has been pursued. The oxygen content, oxidation state of the (Co, Ni) ions, and TEC decrease with increasing Ni content. Although electrical conductivity decreases with increasing Ni content, all the $NdBaCo_{2-x}Ni_xO_{5+\delta}$ samples show conductivity > 300 S/cm up to 900 ^{o}C, which is adequate for employing them as cathodes in SOFC. Substitution of a small amount of Ni ($x = 0.2$ and 0.4) for Co leads to slightly improved performance in SOFC with an important advantage of lower TEC. Considering the TEC value, chemical stability with the electrolytes, and catalytic activity, the $x = 0.4$ sample represents an optimum composition in the $NdBaCo_{2-x}Ni_xO_{5+\delta}$ system for use as a cathode in intermediate temperature SOFC.

A new class of cathode materials $RBa(Co,M)_4O_7$ (R = Y, Ca, In and M = Zn, Fe, Al) based on tetrahedral-site $Co^{2+/3+}$ ions exhibiting a unique combination of high catalytic activity and low TEC have been investigated as cathode materials for SOFC. High temperature phase stability tests in various temperature regions show that $YBaCo_{4-x}Zn_xO_7$ ($1 \leq x \leq 2$) is the only stable composition among the various $RBaCo_{4-x}M_xO_7$ compositions investigated. The $RBaCo_{4-x}M_xO_7$ samples exhibit low TEC values of $6 \times 10^{-6} – 13 \times 10^{-6}$ $^{o}C^{-1}$ in the range of 80 – 900 ^{o}C, providing good thermal expansion compatibility with the standard SOFC electrolyte materials like YSZ, GDC, and LSGM. Although the oxygen permeation flux of the $YBaCo_3ZnO_7$ specimen is 3 – 4 orders of magnitude lower than that found with the cobalt-based perovskite oxides, such low oxygen conduction is overcome by employing $YBaCo_3ZnO_7$ + GDC composites as cathodes in SOFC. With a low cathode polarization resistance and over-potential, the $YBaCo_3ZnO_7$ + GDC composite cathodes exhibit fuel cell performance comparable to that of well-studied Co-based perovskite cathodes, but with the critical advantage of an ideal matching of the TEC value with those of standard electrolytes.

Overall, this work has provided a better understanding of the structure-property-performance relationships of the cathode materials for intermediate SOFC. The electrochemical performance is strongly related to the electrical properties and defect structure, which could be tuned by controlling the chemical compositions of the cathode materials. Although the Co containing perovskite oxides show high electronic and oxide ion conductivities leading to better catalytic activity, they exhibit high TEC due to the spin state transition associated with Co^{3+}. Thus, the high TEC of cobalt-rich perovskite or perovskite-related oxides remains an intrinsic problem to overcome. In this regard, the new class of $RBa(Co,M)_4O_7$ (R = Y, Ca, In and M = Zn, Fe, Al) oxides based on tetrahedral-site $Co^{2+/3+}$ ions are promising as cathode materials for intermediate temperature SOFC, considering the the absence of spin state transitions of $Co^{2+/3+}$ ions and much diminished oxygen loss occurring with increasing temperature. Therefore, future work could focus on a basic understanding of the oxygen bulk or surface exchange mechanisms and further optimization of the chemical compositions. Additionally, since the electrochemical performance of the $YBa(Co,Zn)_4O_7$ is greatly affected by the area of triple phase boundary (TPB), composite cathodes with different ratios of $YBa(Co,Zn)_4O_7$ and GDC could be investigated to optimize the microstructure, porosity, and the area of TPB.

LIST OF PUBLICATIONS RELATED TO THIS WORK

1. J.-H. Kim and A. Manthiram, “$LnBaCo_2O_{5+\delta}$ oxides as cathode for intermediate-temperature solid oxide fuel cells”, *Journal of the Electrochemical Society,* **155**, B385 (2008).
2. J.-H. Kim, F. Prado, and A. Manthiram, “Characterization of $GdBa_{1-x}Sr_xCo_2O_{5+\delta}$ ($0 \leq x \leq 1$) double perovskites as cathodes for solid oxide fuel cells”, *J. Electrochem.Soc.*, **155**, B1023 (2005).
3. J.-H. Kim, L. Mogni, F. Prado, A. Caneiro, and A. Manthiram, “High Temperature Crystal Chemistry and Oxygen Permeation Properties of the Mixed Ionic-Electronic Conductors $LnBaCo_2O_{5+\delta}$ (Ln = lanthanide)”, *Journal of the Electrochemical Society*, submitted in May 2009.
4. J.-H. Kim and A. Manthiram, “Layered $NdBaCo_{2-x}Ni_xO_{5+\delta}$ Perovskite Oxides as Cathodes for Intermediate Temperature Solid Oxide Fuel Cells”, *Electrochimica Acta*, submitted in June 2009.
5. J.-H. Kim and A. Manthiram, “Low Thermal Expansion $RBa(Co,M)_4O_7$ Cathode Materials Based on Tetrahedral-site Cobalt Ions for Solid Oxide Fuel Cells”, *Chemistry of Materials,* submitted in June 2009.
6. A. Manthiram and J.-H. Kim, “Low Thermal Expansion Cathode Materials Based on Tetrahedral-site Cobalt Ions for Solid Oxide Fuel Cells”, U.S. Patent, application filed in March 2009.

REFERENCES

1. W.R. Grove, *Philos. Mag.*, **14**, 127 (1839).
2. J. Larminie and A. Dicks, *Fuel Cell Systems Explained*, John Wiley & Sons, New York, USA (2000).
3. N. Q. Minh and T. Takahshi, *Science and Technology of Ceramic Fuel Cells*, Elsevier Science B. V., Amsterdam, Netherlands (1995).
4. F. Alcaide, P. -L. Cabot, and E. Brillas, *J. Power Sources*, **153**, 47 (2006).
5. K. Koon, *J. Power Sources*, **71**, 12 (1998).
6. S. C. Singhal, *Solid State Ionics*, **135**, 305 (2000).
7. M. Dokiya, *Solid State Ionics*, **152-153**, 386 (2002).
8. A. J. Bard and L. R. Faulkner, *Electrochemical Methods: Fundamentals and Applications. New York*, John Wiley & Sons, New York, (2000).
9. C. M. A. Brett and A. M. O. Brett, *Electrochemistry, Principles, Methods, and Applications*, p. 14, Oxford University Press Inc., New York, USA (1993).
10. O. Yamamoto, *Electrochim. Acta*, **45**, 2423 (2000).
11. S. C. Singhal and K. Kendall, *High Temperature Solid Oxide Fuel Cells: Fundamental, Design, and Applications*, Elsevier Ltd., Oxford, UK (2003).
12. P. J. Gellings and H. J. M. Bouwmeester, *CRC Handbook of Solid State Electrochemistry*, CRC Press, Boca Raton, USZ (1997).
13. E. Baur and H. Preis, ZElektrochem., **43**, 727 (1937).

14. S. Somiya, N. Yamamoto, and H. Yanagida, *Science and Technology of Zirconia III*, American Ceramic Society, Westerville, USA (1988).
15. S. P. S. Badwal, *Solid State Ionics*, **52**, 23 (1992).
16. N. Q. Minh, *J. Am. Ceram. Soc.*, **76**, 563 (1993).
17. H. L. Tuller and A. S. Nowick, *J. Electrochem. Soc.*, **122**, 255 (1975).
18. K. Eguchi, T. Setoguchi, T. Inoue, and H. Arai, *Solid State Ionics*, **52**, 165 (1992).
19. A. V. Virkar, *J. Electrochem. Soc.*, **138**, 1481 (1991).
20. T. Kawada, D. Ueno, M. Sase, K. Yashiro, T. Otake, A. Kaimai, and J. Mizusaki. In *SOFC IX*, eds. S.C. Singhal and J. Mizusaki,. *The Electrochemical Society*, Pennington, USA, PV2005-07 (2005).
21. A. Tsoga, A. Gupta, A. Naoumidis, and P. Nikolopoulos, *Acta Mater*., **48**, 4709 (2000).
22. T. Ishihara, H. Matsuda, and Y. Takita, *Solid State Ionics,* **79**, 147 (1995).
23. P.N. Huang and P. Petric, *J. Electrochem. Soc.*, **143**, 1644 (1996).
24. K. Huang, R. Tichy, and J. B. Goodenough, *J. Am. Ceram. Soc.*, **81**, 2565 (1998).
25. S. Srilomsak, D. P. Schlling and H. U. Anderson, in *Solid Oxide Fuel Cell I*, ed. S. C. Singhal, *The Electrochemical Society Proceedings*, Pennington, USA, PV 89-11 (1989).
26. M. Mori and Y. Hiei, in *Solid Oxide Fuel Cell VI*, eds. S. C. Singhal and M. Dokiya, *The Electrochemical Society Proceedings*, Pennington, USA, PV99-19 (1999).

27. V. V. Kharton, F. M. B. Marques, and A. Atkinson, Solid State Ionics, **174**, 135 (2004).
28. R. A. De Souza and J. A. Kilner, *Solid State Ionics*, **106**, 175 (1998).
29. D. J. L. Brett, A. Atkinson, N. P. Brandon, and S. J. Skinner, *Chem. Soc. Rev.*, **37**, 1568 (2008).
30. R. A. De Souza and J. A. Kilner, *Solid State Ionics*, **106**, 175 (1998).
31. M. J. L. Ostergard, C. Clausen, C. Bagger, and M. Mogensen, *Electrochim. Acta*, **40**, 1971(1995).
32. T. Tsai and S. A. Barnett, *Solid State Ionics*, **93**, 207 (1997).
33. S. K. Lau and S. C. Singhal, *Corrosion,* **85**, 1 (1985).
34. M. Suzuki, H. Sasaki, S. Otoshi, A. Kajimura, N. Sugiura and M. Ipponmatsu, *J. Electrochem. Soc.*, **141**, 1928 (1994).
35. T. Kawada, J. Suzuki, M. Sase, A. Kaimai, K. Yashiro, Y. Nigara, J. Mizusaki, K. Kawamura, and H. Yugami, *J. Electrochem. Soc.*, **149**, E252 (2002).
36. W. Zipprich, S. Waschilewski, F. Rocholl, and H. D. Wiemhofer, *Solid State Ionics*, **101-103**, 1015 (1997).
37. H. Yokokawa, N. Sakai, T. Kawada, and M. Dokiya, *J. Electrochem. Soc.*, **138**, 2719 (1991).
38. O. Yamamoto, Y. Takeda, R. Kanno, and M. Noda, *Solid State Ionics*, **22**, 241 (1987).
39. Y. Ohno, S. Nagata, and H. Sato, *Solid State Ionics*, **9-10**, 1001 (1983).

40. J. W. Adams, H. H. Nakamura, R. P. Ingel, and R. W. Rice, *J. Am. Ceram. Soc.*, **68**, C-228 (1985).

41. M. A. Señarís-Rodríguez and J. B. Goodenough, *J. Solid State Chem.,* **118**, 323 (1995).

42. B. *C.* H. Steele, *Solid State lonics,* **129**, 95 (2000).

43. E. C. H. Steele and J.-M. Bae, *Solid State Ionics,* **106**, 255 (1998) .

44. E. P. Murray, M. J. Sever, and S. A. Barnett, *Solid State Ionics*, **148**, 27 (2002).

45. S.N. Ruddlesden and P. Popper, *Acta Crystallogr.*, **11**, 54 (1958).

46. F. Prado, L. Mogni, G.J. Cuello, and A. Caneiro, *Solid State Ionics*, **178**, 77 (2007).

47. A. Manthiram, F. Prado, and T. Armstrong, *Solid State Ionics*, **152–153**, 647 (2002).

48. K.T. Lee and A. Manthiram, *Chem. Mater.*, **18**, 1621 (2006).

49. T. Armstrong, F. Prado, and A. Manthiram, *Solid State Ionics*, **140**, 89 (2001).

50. F. Prado, T. Armstrong, A. Caneiro, and A. Manthiram, *J. Electrochem. Soc.*, **148**, J7 (2001).

51. G. Amow and S.J. Skinner, *J. Solid State Electrochem.*, **10**, 538 (2006).

52. F. Prado, K. Gurunathan, and A. Manthiram, *J. Mater. Chem.*, **12**, 2390 (2002).

53. A. Manthiram and J. B. Goodenough, *Solid State Chem.*, **92**, 231 (1991).

54. Z. Zhang, M. Greenblatt, and J. B. Goodenough, *J. Solid State Chem.*, **108**, 402 (1994).

55. I. D. Fawcett, G. M. Veith, and M. Greenblatt, *J. Solid State Chem*., **155**, 96 (2000).

56. V. V. Kharton, E. V. Tsipis, E. N. Naumovich, A. Thursfield, M. V. Patrakeev, V. A. Kolotygin, J. C. Waerenborgh, and I. S. Metcalfe, *J. Solid State Chem*., **181**, 1425 (2008).

57. J. A. Kilner and C. K. M. Shaw, *Solid State Ionics*, **154–155**, 523 (2002).

58. K. Yamaura, Q. Huang, and R. J. Cava*, J. Solid State Chem*., **146**, 277 (1999).

59. K.T. Lee, D.M. Bierschenk, and A. Manthiram, *J. Electrochem. Soc*., **153**, A1255 (2006).

60. T. Ogawa, T. Ioroi, Y. Uchimoto, Z. Ogumi and Z.-I. Talrehara, in *Solid Oxide Fuel Cells III, The Electrochemical Society Proceedings*, Pennington, NJ, PV 93-4 (1993).

61. T. Horita, N. Saltai, T. ICawada, H. Yoltoltawa, and M. Dokiya, *J. Electrochem. Soc.,* **143**, 1161 (1996).

62. B.C.H. Steele, I. Kelly, H. Middleton, and R. Rudkin, *Solid State Ionics*, **28–30**, 1547 (1988)

63. Y. Matsuzaki and I. Yasuda, *Solid State Ionics*, **132**, 261 (2000)

64. S. Park, J.M. Vohs, and R.J. Gorte, *Nature*, **404**, 265 (2000).

65. S. Mcintosh, J.M. Vohs, and R.J. Gorte, *Electrochim. Acta,* **47**, 3815–3821 (2002).

66. S. Park, R. Cracium, J.M. Vohs, and R.J. Gorte, *J. Electrochem. Soc*., **146**, 3603 (1999).

67. C. Lu, W.L. Worrell, R.J. Gorte, and J.M. Vohs, *J. Electrochem. Soc.*, **150**, A354 (2003).

68. B.C.H. Steele, P.H. Middleton, and R.A. Rudkin, *Solid State Ionics*, **40-41**, 388 (1990).

69. C. Sun and U. Stimming, *J. Power Sources*, **171**, 247 (2007).

70. S.W. Tao and J.T.S. Irvine, *Nat. Mater.*, **2**, 320 (2003).

71. Y.H. Huang, R.I. Dass, Z.L. Xing, and J.B. Goodenough, *Science,* **312**, 254 (2006).

72. L. A. Chick, L. R. Pedersen, G. D. Maupin, J. L. Bates, L. E. Thomas, and G. J. Exarhos, *Mater. Lett.*, **10**, 6 (1990).

73. H. Taguchi, D. Mastuda, M. Nagao, K. Tanihata, and Y. Miyamoto, *J. Am. Ceram. Soc.*, **75**, 201 (1992).

74. J. Rodriguez-Carjaval, *Physica B*, **192**, 55 (1993).

75. G. Will, *Powder Diffraction: The Rietveld Method and the Two Stage Method to Determine and Refine Crystal Structures from Powder Diffraction Data*, Springer, Berlin, Germany (2006).

76. V. K. Pecharsky and P. Y. Zavalij, *Fundamentals of Powder Diffraction and Structural Characterization of Materials*, Springer, New York, USA (2005).

77. G. H. Jeffery, J. Bassett, J. Mendham, and R. C. Denney, *Vogel's Textbook of Quantitative Chemical Analysis*, 5th ed., John Wiley & Sons, New York, USA (1989)

78. A. Manthiram, J. S. Swinnea, Z. T. Sui, H. Steinfink, and J. B. Goodenough, *J.*

Am. Chem. Soc., **109**, 6667 (1987).

79. L. J. Van der Pauw, *Philips Res. Repts*., **13**, 1 (1958).
80. I. Reiss, *J. Appl. Phy*., **71**, 4079 (1992).
81. H. Kruidhof, H. J. M. Bouwmeester, R. H. E. van Doorn, and A. J. Burggraaf, *Solid State Ionics*, **63-65**, 816 (1993).
82. J. Wan, J. H. Zhu, and J. B. Goodenough, *Solid State Ionics*, **177**, 1211 (2006).
83. I. O. Troyanchuk, N. V. Kasper, and D. D. Khalyavin, *Phys. Rev. B*, **58**, 2418 (1998).
84. Y. Moritomo, M. Takeo, X. J. Liu, T. Akimoto, and A. Nakamura, *Phys. Rev. B*, **58**, R13 334 (1998).
85. A. Maignan, C. Martin, D. Pelloquin, N. Nguyen, and B. Raveau, *J. Solid State Chem.*, **142**, 247 (1999).
86. T. Vogt, P. M. Woodward, P. Karen, B. A. Hunter, P. Henning, and A. R. Moodenbaugh, *Phys. Rev. Lett.*, **84**, 2969 (2000).
87. C. Martin, A. Maignan, D. Pelloquin, N. Nguyen, and B. Raveau, *Appl. Phys. Lett.*, **71**, 1421 (1997).
88. A. Chang, S. J. Skinner, and J. A. Kilner, *Solid State Ionics*, **177**, 2009 (2006).
89. E. Suard, F. Fauth, and V. Caignaert, *Physica B*, **276**, 254 (2000).
90. M. Mori, Y. Hiei, N. M. Sammes, and G. A. Tompsett, *J. Electrochem. Soc.*, **147**, 1295 (2000).
91. K. T. Lee and A. Manthiram, *J. Electrochem. Soc.,* **152**, A197 (2005).
92. K. T. Lee and A. Manthiram, *J. Electrochem. Soc.,* **153**, A794 (2006).

93. H. Takahashi, F. Munakata, and M. Yamanaka, *Phys. Rev. B*, **57**, 15211 (1998).

94. H. Ullmann, N. Trofimenco, F. Tiez, D. Stöver, and A. Ahmad-Khanlou, *Solid State Ionics*, **138**, 79 (2000).

95. Y. Teraoka, T. Nobunaga, and N. Yamazoe, *Chem. Lett.*, 503 (1988).

96. J.-M. Bae and B. C. H. Steele, *Solid State Ionics*, **106**, 247 (1998).

97. K. T. Lee and A. Manthiram, *Solid State Ionics*, **176**, 1521 (2005).

98. Z. Shao and S. M. Haile, *Nature*, **431**, 170 (2004).

99. B. Wei, Z. Lü, X. Huang, J. Miao, X. Sha, X. Xin, and W. Su, *J. Eur. Ceram. Soc.*, **26**, 2827 (2006).

100. S. Streule, A. Podlesnyak, D. Sheptyakov, E. Pomjakushina, M. Stingaciu, K. Conder, M. Medarde, M. V. Patrakeev, I. A. Leonidov, V. L. Kozhevnikov, and J. Mesot, *Phys. Rev. B*, **73**, 094203 (2006).

101. A. Tarancón, D. Marrero-López, J. Peña-Martínez, J. C. Ruiz-Morales, and P. Núñez, *Solid State Ionics*, **179**, 611 (2008).

102. A. A. Taskin, A. N. Lavro, and Y. Ando, *Appl. Phys. Lett.*, **86**, 091910 (2005).

103. G. Kim, S. Wang, A. J. Jacobson, L. Reimus, P. Brodersen, and C. A. Mims, *J. Mater. Chem.*, **17**, 2500 (2007).

104. A. Tarankon, S. J. Skinner, R. J. Chater, F. H. Ramírez, and J. A. Kilner, *J. Mater. Chem.*, **17**, 3175 (2007).

105. C. Frontera, A. Caneiro, A. E. Carrillo, J. Oró-Solé, and J. L. García-Muñoz, *Chem. Mater.*, **17**, 5439 (2005).

106. J.C. Burley, J.F. Mitchell, S. Short, D. Miller, and Y. Tang, *J. Solid State Chem.*,

170, 339 (2003).

107. H. J. M. Bouwmeester, H. Kruidhof, and A. J. Burggraaf, *Solid State Ionics*, **72**, 185 (1994).
108. M. Mogensen, D. Lybye, N. Bonanos, P. V. Hendriksen, and F. W.Poulsen, *Solid State Ionics*, **174**, 279 (2004).
109. C. Wagner, *Progr. Solid State Chem.*, **10**, 3 (1975).
110. P. V. Vanitha, A. Arulraj, P. N. Santhosh, and C.N.R. Rao, *Chem. Mater.*, **12**, 1666 (2000).
111. X. G. Luo, H. Li, X. H. Chen, Y. M. Xiong, G. Wu, G. Y. Wang, C. H. Wang, W. J. Miao, and X. Li, *Chem. Mater.*, **18**, 1029 (2006).
112. J. Nakamura, M. Karppinen, P. Karen, J. Lindén, and H. Yamauchi, *Phys. Rev. B.*, **70**, 144104 (2004).
113. D. Akahoshi and Y. Ueda, *J. Solid State Chem.*, **156**, 355 (2001).
114. J.-H, Kim and A. Manthiram, *J. Electrochem. Soc.*, **155**, B385 (2008).
115. R.D. Shannon, *Acta Crystallogr., Sect. A: Cryst. Phys., Diffr.,Theor. Gen. Crystallogr.*, **32**, 751 (1976).
116. P. Karen, *J. Solid State Chem.*, **177**, 281 (2004).
117. J. A. Dean, *Lange's Handbook of Chemistry*, 5th ed., McGraw-Hill Inc., New York, USA (1999).
118. F.A. Kroger and H.J. Vink, in *Solid State Physics*, eds. F. Seitz and D. Turnbull, Vol. 3, Academic Press, New York, USA (1956).
119. K. Huang, H. Y. Lee, and J. B. Goodenough, *J. Electrochem. Soc.*, **145**, 3220

(1998).

120. G. Ch. Kostogloudis, N. Vasilakos, and Ch. Ftikos, *Solid State Ionics*, **106**, 207 (1998).

121. A. Bharathi, P. Yasodha, N. Gayathri, A. T. Satya, R. Nagendran, N. Thirumurugan, C. S. Sundar, and Y. Hariharan, *Phys. Rev. B*, **77**, 085113 (2008).

122. M. Godickemeier, K. Sasaki, and L. J. Gauckler, *J. Electrochem. Soc.*, **144**, 1635 (1997).

123. M. Godickemeier and L. J. Gauckler, *J. Electrochem. Soc.*, **145**, 414 (1998).

124. Ch. Ftikos, S. Carter, and B. C. H. Steele, *J. Eur. Ceram. Soc.*, **12**, 79 (1993).

125. M. Karppinen, H. Yamauchi, S. Otani, T. Fujita, T. Motohashi, Y.-H. Huang, M. Valkeapää, and H. Fjellvåg, *Chem. Mater.*, **18**, 490 (2006).

126. M. Valldor, *Solid State Sci.*, **6**, 251 (2004).

127. A. Maignan, V. Caignaert, D. Pelloquin, S. Hébert, and V. Pralong, *Phys. Rev. B*, **74**, 165110 (2006).

128. E. V. Tsipis, V. V. Kharton, and J. R. Frade, *Solid State Ionics*, **177**, 1823 (2006).

129. H. Hao, J. Cui, C. Chen, L. Pan, J. Hu, and X. Hu, X. *Solid State Ionics*, **177**, 631 (2006).

130. T. Mokkelbost, I. Kaus, T. Grande, and M. A. Einarsrud, *Chem. Mater.*, **16**, 5489 (2004).

131. K. Huang and J. B. Goodenough, *J. Electrochem. Soc.*, **148**, E203 (2001).

132. T. J. Ahrens, *Mineral physics and crystallography: a handbook of physical constants*, American Geophysical Union, Washington DC, USA (1995).

133. S. Kadota, M. Karppinen, T. Motohashi, and H. Yamauchi, *Chem. Mater.*, **20**, 6378 (2008).

134. Y. Jia, H. Jiang, M. Valkeapää, H. Yamauchi, M. Karppinen, and E. Kauppinen, *J. Am. Chem. Soc*., **131**, 4880 (2009).

135. O. Chmaissema, H. Zheng, A. Huq, P. W. Stephens, J. F. Mitchell, *J. Solid State Chem.*, **181**, 664 (2008).

136. C. Peters, A. Weber, and E. Ivers-Tiffée, *J. Electrochem. Soc.*, **155**, B730 (2008).

137. Kim, J.-H.; Prado, F.; Manthiram, A. *J. Electrochem. Soc.*, **155**, B1023 (2008).

VITA

Jung-Hyun Kim was born in 1976 in Seoul, Republic of Korea. He earned his B.S. and M.S. degrees in Chemical Engineering from Hanyang University in Seoul, Republic of Korea in February, 2002 and February, 2004, respectively. He worked at the Korea Institute of Energy Research as a research scientist from December, 2004 to July, 2005. He entered the University of Texas at Austin in August, 2005.

List of Publications:

1. J.-H. Kim and Y.-K. Sun, "Electrochemical performance of $Li[Li_xNi_{(1-3x)/2}Mn_{(1+x)/2}]O_2$ cathode materials synthesized by a sol-gel method," *Journal of Power Sources*, **119**, 166 (2003).
2. J.-H. Kim, C.S. Yoon, and Y.-K. Sun, "Structural Characterization of $Li[Li_{0.1}Ni_{0.35}Mn_{0.55}]O_2$ Cathode Material for Lithium Secondary Batteries," J*Journal of the Electrochemical Society*, **150**, A538 (2003).
3. J.-H. Kim, C.W. Park, and Y.-K. Sun, "Synthesis and electrochemical behavior of $Li[Li_{0.1}Ni_{0.35-x/2}Co_xMn_{0.55-x/2}]O_2$ cathode materials," *Solid State Ionics*, **164**, 43 (2003).
4. J.-H. Kim, S.-T. Myung, and Y.-K. Sun, "Molten salt synthesis of $LiNi_{0.5}Mn_{1.5}O_4$ spinel for 5 V class cathode material of Li-ion secondary battery," *Electrochimica Acta*, **49**, 219 (2004).
5. J.-H. Kim, S.-T. Myung, C. S. Yoon, and Y.-K. Sun, "The Effect of Ti Substitution for Mn on the Structure and Electrochemical Properties of $LiNi_{0.5}Mn_{1.5-x}Ti_xO_4$ Cathode Material," *Journal of the Electrochemical Society*, **151**, A1911 (2004).
6. J.-H. Kim, C.S. Yoon, S.-T. Myung, Jai Prakash, and Y.-K. Sun, "Phase Transitions in $Li_{1-\delta}Ni_{0.5}Mn_{1.5}O_4$ during cycling at 5 V," *Electrochemical and Solid-State Letters*, **7**, A216 (2004).

7. J.-H. Kim, S.-T. Myung, C.S. Yoon, S.G. Kang, and Y.-K. Sun, "Comparative study of $LiNi_{0.5}Mn_{1.5}O_{4-\delta}$ and $LiNi_{0.5}Mn_{1.5}O_4$ cathodes having two crystallographic structures: *Fd*-3*m* and $P4_332$," *Chemistry of Materials*, **16**, 906 (2004).

8. M.-G. Kim, H.-J. Shin, J.-H. Kim, S.-H. Park, and Y.-K. Sun, "XAS investigation of inhomogeneous metal-oxygen bond covalency in bulk and surface for charge compensation in li-ion battery cathode $Li[Mn_{1/3}Co_{1/3}Ni_{1/3}]O_2$ material," *Journal of the Electrochemical Society,* **152**, A1320 (2005).

9. Y.-J. Kang, J.-H. Kim, and Y.-K. Sun, "Structural and electrochemical study of Li-Al-Mn-O-F spinel material for lithium secondary batteries," *Journal of Power Sources,* **146**, 237 (2005).

10. Y.-J. Kang, J.-H. Kim, S.-W. Lee, and Y.-K. Sun, "The effect of $Al(OH)_3$ coating on the $Li[Li_{0.2}Ni_{0.2}Mn_{0.6}]O_2$ cathode material for lithium secondary battery," *Electrochimica Acta,* **50**, 4784 (2005).

11. G.-H Kim, J.-H. Kim, C. S. Yoon, S.-T. Myung, and Y.-K Sun, "Improvement of high voltage cycling behavior of surface-modified $Li[Ni_{1/3}Co_{1/3}Mn_{1/3}]O_2$ cathode by fluorine substitution for Li-ion battery," *Journal of the Electrochemical Society,* 152, A1707 (2005).

12. Y.-K. Sun, S.-T. Myung, M.-H. Kim, and J.-H. Kim, "Microscale core-shell structured $Li[(Ni_{0.8}Co_{0.1}Mn_{0.1})_{0.8}(Ni_{0.5}Mn_{0.5})_{0.2}]O_2$ as positive electrode material for lithium batteries," *Electrochemical and Solid-State Letters,* **9**, A171 (2006).

13. S.-W. Oh, S.-H. Park, J.-H. Kim, Y. C. Bae, and Y.-K. Sun, "Improvement of electrochemical properties of $LiNi_{0.5}Mn_{1.5}O_4$ spinel material by fluorine substitution," *Journal of Power Sources,* **157**, 464 (2006).

14. J.-H. Kim, R.-H. Song, J.-H. Kim, T.-H. Lee, Y.-K. Sun, and D.-R. Shin, "Co-synthesis of nano-sized LSM-YSZ composites with enhanced electrochemical property," *Journal of the Solid State Electrochemistry,* **11** (10) 1385-1390 (2007).

15. J.-H. Kim and A. Manthiram, "$LnBaCo_2O_{5+\delta}$ oxides as cathode for intermediate-temperature solid oxide fuel cells," *Journal of the Electrochemical Society,* **155**, B385 (2008).

16. J.-H. Kim, F. Prado, and A. Manthiram, "Characterization of $GdBa_{1-x}Sr_xCo_2O_{5+\delta}$ ($0 \leq x \leq 1$) double perovskites as cathodes for solid oxide fuel cells," *Journal of the Electrochemical Society,* **155** (10) B1023-B1028 (2008).

17. J.-H. Kim, L. Mogni, F. Prado, A. Caneiro, A. Manthiram, "High Temperature Crystal Chemistry and Oxygen Permeation Properties of the Mixed Ionic-Electronic Conductors $LnBaCo_2O_{5+\delta}$ (Ln = lanthanide)," *Journal of the Electrochemical Society*, submitted on May 2009.

18. J.-H. Kim and A. Manthiram, "Layered $NdBaCo_{2-x}Ni_xO_{5+\delta}$ Perovskite Oxides as Cathodes for Intermediate Temperature Solid Oxide Fuel Cells," *Electrochimica Acta*, submitted on June 2009.
19. J.-H. Kim and A. Manthiram, "Characterization of $Sr_{2.7}Ln_{0.3}Fe_{1.4}Co_{0.6}O_7$ (Ln = La, Nd, Sm, Gd) intergrowth oxides as cathodes for solid oxide fuel cells," *Solid State Ionics*, submitted on June 2009.
20. J.-H. Kim and A. Manthiram, "Low Thermal Expansion $RBa(Co,M)_4O_7$ Cathode Materials Based on Tetrahedral-site Cobalt Ions for Solid Oxide Fuel Cells," *Chemistry of Materials,* submitted on June 2009.
21. S. Cho, J. Yoon, J.-H. Kim, A. Serquis, X. Zhang, A. Manthiram, and H. Wang, "Vertically aligned nanocomposite thin films as a cathode-electrolyte interface layer for thin film solid oxide fuel cells," *Advanced Functional Materials*, accepted.

Permanent address: 102-101 Banpo Hanshintower Apt. Jamwon-dong, Seocho-gu,

Seoul, Republic of Korea 137-909

This dissertation was typed by the author.